UNIVERSITY OF CALIFORNIA, SAN DIEGO

Hybrid Models of Transport in Crowded Environments

A dissertation submitted in partial satisfaction of the
requirements for the degree
Doctor of Philosophy

in

Engineering Science with Specialization in Computational Science

by

Ilenia Battiato

Committee in charge:

Professor Daniel M. Tartakovsky, Chair
Professor Scott B. Baden
Professor Paul F. Linden
Professor Sutanu Sarkar
Professor Terrence J. Sejnowski

2010

The dissertation of Ilenia Battiato is approved, and it is acceptable in quality and form for publication on micro-film and electronically:

_____

_____

_____

_____
Chair

University of California, San Diego

2010

DEDICATION

To "my family".

EPIGRAPH

"Il Sapere deve affaticarsi in un lungo itinerario"

(Knowledge has to weary through a long itinerary)

—Hegel

TABLE OF CONTENTS

LIST OF FIGURES

ACKNOWLEDGEMENTS

Time has come for the acknowledgments and I am incredulous.

It is common practice to thank the adviser first for giving the opportunity of conducting such a wonderful and interesting research, etc.

I will not follow such practice, though. Instead, I will thank a friend and a model, who first changed my future and then taught me everything I know. Thank you for your patience and your trust. Thank you for tolerating my artistic distractions with a smile on your face. Thank you for believing in me. Thank you for meeting with me over the weekends when I was prey of despair. Thank you for forgiving my "juvenile" stubbornness. Thank you for listening to what I had to say. Thank you for telling that everything is "easy" (at some point it really started to help). Thank you for encouraging me. Thank you for contradicting me, whatever I said; it made our conversations much more interesting. Thank you for my achievements as they would not be possible without you. Thank you for the Moet & Chandon, it was really good. Thank you for letting me go. Thank you, Daniel for everything you have been, you still are and you will be for me.

Questa parte in italiano e' riservata alla mia famiglia. Anche loro, dopotutto, si meritano di essere un po' coccolati, come lo sono stata io per tutti i miei anni trascorsi su questa terra.

Zia Peppa, il primo pensiero va a te. Grazie per essere stata sempre presente. La tua forza e' adesso la mia forza.

Mamma e papa', grazie per avermi sostenuto incondizionatamente e aiutato a fare le scelte giuste nei momenti piu' difficili. Questo e' il mio futuro ed e' a voi che lo dedico.

Marco, grazie di essere mio fratello e mio amico. Magari un giorno potremmo diventare anche collaboratori!

Grazie Michele, per avermi insegnato quanto profondi possono essere la vita e l'amore.

The text of this dissertation includes the reprints of the following papers, either accepted or submitted for consideration at the time of publication. The dissertation

author was the primary investigator and author of these publications.

Chapter 2

Battiato, I., Bandaru, P. R., Tartakovsky, D. M., (2010) 'Elastic Response of Carbon Nanotube Forests to Aerodynamic Stresses'. *Physical Review Letters. In press.*

Chapter 3

Battiato, I., Tartakovsky, D. M., Tartakovsky, A. M., Scheibe T. D., (2009), 'On Breakdown of Macroscopic Models of Mixing-Controlled Heterogeneous Reactions in Porous Media'. *Adv. Water Resour., doi:10.1016/j.advwatres.2009.08.008.*

Chapter 4

Battiato, I., Tartakovsky, D. M., (2010), 'Applicability Regimes for Macroscopic Models of Reactive Transport in Porous Media'. *Journ. Cont. Hydrol., Special Issue, Invited, http://dx.doi.org/10.1016/j.jconhyd.2010.05.005.*

Chapter 5

Battiato, I., Tartakovsky, D. M., Tartakovsky, A. M., Scheibe, T.D., (2010),'Hybrid Simulations of Reactive Transport in Fractures'. *Adv. Water Resour., Special Issue, Submission code: AWR-10-234.*

Chapter 6

Battiato, I., Tartakovsky, D. M. (2010),'Nonintrusive hybrid algorithm of transport in crowded environments. *Under preparation.*

VITA

2010	Doctor of Philosophy in Engineering Physics with Specialization in Computational Science, University of California, San Diego.
2008	M.Sc. in Engineering Physics, University of California, San Diego.
2006-2010	Graduate Student Researcher, University of California, San Diego.
2005	Laurea (M.Sc. equivalent) in Environmental Engineering, Politecnico di Milano, *Summa cum laude.*

JOURNAL PUBLICATIONS

Battiato, I., Tartakovsky, D. M., (2010), 'Applicability Regimes for Macroscopic Models of Reactive Transport in Porous Media'. *Journ. Cont. Hydrol., Special Issue, Invited, http://dx.doi.org/10.1016/j.jconhyd.2010.05.005.*

Battiato, I., Bandaru, P. R., Tartakovsky, D. M., (2010) 'Elastic Response of Carbon Nanotube Forests to Aerodynamic Stresses'. *Physical Review Letters. In press.*

Battiato, I., Tartakovsky, D. M., Tartakovsky, A. M., Scheibe, T.D.,(2010) 'Hybrid Simulations of Reactive Transport in Fractures'. *Adv. Water Resour., Special Issue, Submission code: AWR-10-234.*

Battiato, I., Tartakovsky, D. M., Tartakovsky, A. M., Scheibe T. D., (2009), 'On Breakdown of Macroscopic Models of Mixing-Controlled Heterogeneous Reactions in Porous Media'. *Adv. Water Resour., doi:10.1016/j.advwatres.2009.08.008.*

Battiato, I., Tartakovsky, D. M. (2010),'Nonintrusive hybrid algorithm of transport in crowded environments. *Under preparation.*

BOOK CHAPTERS

Battiato, I., Tartakovsky, D. M., (2010) 'From Upscaling Techniques to Hybrid Models'.

Mathematical and Numerical Modeling in Porous Media: Applications in Geosciences,

CRC Press. Under preparation.

SELECT PRESENTATIONS

Battiato, I., Tartakovsky, D. M., 'Hybrid Simulations of Reactive Transport in Porous Media', (2010) *XVIII International Conference on Computational Methods in Water Resources, Barcellona, Spain, June 21-24.*

Battiato, I., Tartakovsky, D. M., 'Upscaling of Nonlinear Reactive Transport via Multiple-Scale Expansions', (2009) *AGU Fall Meeting, San Francisco CA, December 14-18.*

Battiato, I., 'Upscaling Techniques and Hybrid Models of Reactive Transport in Porous Media', (2009) *8th North American Workshop on Applications of the Physics of Porous Media, Ensenada, Baja California, Mexico, October 9-12.*

Battiato, I., Tartakovsky, D. M., Tartakovsky, A. M., 'Breakdown of Macroscopic Models of Reactive Transport In Porous Media', (2009) *Fluxes and Structures in Fluids: Physics of Geospheres, Moscow, June 24-27.*

Battiato, I., Tartakovsky, D. M., 'Macroscopic Models of Reactive Transport In Porous Media', (2009) *3rd Southern California Symposium On Flow Physics, San Diego CA, April 19.*

Battiato, I., Tartakovsky, A., Tartakovsky, D., 'Homogeneization Techniques for Reactive Transport in Porous Media', (2008) *GRA 17th Annual Groundwater Conference and Meeting, Costa Mesa, CA, September 25-26.*

POSTER PRESENTATIONS

Battiato, I., Bandaru, P. R., Tartakovsky, D. M., 'Elastic Response of Carbon Nanotube Forests to Aerodynamic Stresses', (2010) *Research Expo, University of California, San Diego, April 15.*

Battiato, I., Tartakovsky, A. M., Tartakovsky, D. M., Scheibe T. D., 'Mixing-Induced Precipitation Phenomena: Range of Applicability of Macroscopic Equations', (2009) *DOE-ERSP Annual PI Meeting, Lansdowne VA, April 20-23.*

Battiato, I., Tartakovsky, A. M., Tartakovsky, D. M., Scheibe T. D., 'Mixing-Induced Precipitation Phenomena: Range of Applicability of Macroscopic Equations', (2008) *AGU Fall Meeting, San Francisco CA, December 15-19.*

AWARDS

Outstanding Student Paper Award, AGU Fall meeting, San Francisco (2008).

ABSTRACT OF THE DISSERTATION

Hybrid Models of Transport in Crowded Environments

by

Ilenia Battiato

Doctor of Philosophy in Engineering Science with Specialization in
Computational Science

University of California, San Diego, 2010

Professor Daniel M. Tartakovsky, Chair

This dissertation deals with multi-scale, multi-physics descriptions of flow and transport in crowded environments forming porous media. Such phenomena can be described by employing either pore-scale or continuum-scale (Darcy-scale) models. Continuum-scale formulations are largely phenomenological, but often provide accurate and efficient representations of flow and transport. In the first part of the dissertation, we employ such a model to describe fluid flow through carbon nanotube (CNT) forests placed in a turbulent ambient environment of a microscopic wind tunnel. This analysis leads to closed-form analytical formulae that enable one to predict elastic response of CNT forests to aerodynamic loading and to estimate elastic properties of individual CNTs, both of which were found to be in a close agreement with experimental data. The second part of this work explores the applicability range of continuum-scale models of transport of chemically active solutes undergoing nonlinear homogeneous and heterogeneous reactions with the porous matrix. We use two upscaling techniques (the volume averaging method and multiple-scale expansions) to formulate sufficient conditions for the validity of continuum-scale models in terms of dimensionless numbers characterizing key pore-scale transport

mechanisms (e.g. Péclet and Damköhler numbers). When these conditions are not satisfied, standard continuum-scale models have to be replaced with upscaled equations that are nonlocal in space and time, effective parameters (e.g. dispersion tensors, effective reaction rates) do not generally exist, and pore- and continuum-scales cannot be decoupled. Such transport regimes necessitate the development of hybrid numerical methods that couple the pore- and continuum-scale models solved in different regions of the computational domain. Hybrid methods aim to combine the physical rigor of pore-scale modeling with the computational efficiency of its continuum-scale counterpart. In the third and final part of this dissertation, we use the volume averaging method to construct two hybrid algorithms, one intrusive and the other non-intrusive, that facilitate the coupling of pore- and continuum-scale models in a computationally efficient manner.

Chapter 1

Introduction

"That it is not a science of production
is clear even from the history of the earliest philosophers.
For it is owing to their wonder that men
both now begin and at first began to philosophize;
they wondered originally at the obvious difficulties,
then advanced little by little and stated difficulties about the greater matters,
e.g. about the phenomena of the moon and those of the sun and of the stars,
and about the genesis of the universe.
And a man who is puzzled and wonders thinks himself ignorant
(whence even the lover of myth is in a sense a lover of Wisdom,
for the myth is composed of wonders);
therefore since they philosophized in order to escape from ignorance,
evidently they were pursuing science in order to know,
and not for any utilitarian end. And this is confirmed by the facts;
for it was when almost all the necessities of life
and the things that make for comfort and recreation had been secured,
that such knowledge began to be sought.
Evidently then we do not seek it for the sake of any other advantage;
but as the man is free, we say, who exists for his own sake and not for another's,
so we pursue this as the only free science, for it alone exists for its own sake."

-Aristotle

"Metaphysics" (translated by W. D. Ross)

1.1 A question of scale...

Any mathematical model is an idealization of a real system at a specified scale. Assumptions and/or simplifications upon which such models are based enable their formulation, analytical and/or numerical treatment and, consequently, their use as predictive tools. The acceptance of a model derives from an optimal balance between simplicity and accuracy in capturing a system's behavior on the one hand and computational costs on the other. Different models might offer optimal performances, both in terms of fidelity and computation, in various regimes. A further complication in model selection arises when a scale at which predictions are sought is much larger than a scale at which governing equations and first principles are well defined. This situation is particularly common in analyses of flow and transport in crowded environments (porous media): the typical scales of interest for predictions are often many orders of magnitude larger than the scale at which heterogeneities might manifest themselves. Such complex systems are of particular interest because of their ubiquitous nature: they characterize a variety of environments ranging from geologic formations to biological cells, and from oil reservoirs to nanotechnology products.

Flow and transport in porous media can be modeled at the pore- (microscopic) or Darcy- (macroscopic) scales. The use of either representation is a statement of purpose for any individual who has decided to devote his/her zeal to the scientific cause: continuum-scale models lie in the realm of real world applications (let us not forget that H. Darcy was a civil engineer), while pore-scale models still mainly, if not exclusively, exist in the academic "crystal palace".

Equations that have a solid physical foundation based on the first principles (e.g., Stokes equations for fluid flow and Fick's law of diffusion for solute transport) usually satisfy the needs of the most demanding theoretician, even if the use of such microscopic models requires the knowledge of pore geometry (that is seldom available in real applications): this is a price that he/she is usually willing to pay. While rapid

advancements in computational power and imagine techniques bode well for the social and utilitarian redemption of theoreticians (who eventually will not have to make a choice between theoretical rigor and practical usefulness), computational domains that can be modeled with modern-day pore-scale simulations are still too small to be of any use for predictions at the field scale: the heterogeneity of most natural porous media (e.g. oil reservoirs, aquifers) and technology products (carbon nanotubes assemblies) and prohibitive computational costs render lattice-Boltzmann modeling [2], smoothed particle hydrodynamics [3], molecular dynamics [4] and other pore-scale simulations impractical as a predictive tool at scales that are many orders of magnitude larger than the pore scale.

Macroscopic models (e.g., Darcy's law for fluid flow and an advection-dispersion equation for transport), which treat a porous medium as an "averaged" continuum, overcome these limitations by relying on phenomenological descriptions and a number of simplifications (e.g., spatial smoothness of pore-scale quantities, spatial periodicity of pore structures, and low degree of physical and chemical heterogeneity). Engineers typically accept them with a dose of good spirit and hopeful expectation (usually well placed).

While the ubiquitous presence of heterogeneities in natural systems might lead to a localized breakdown of such continuum models, in many applied disciplines the transition from theoretical modeling to practical applications poses the danger of loosing track of modeling assumptions. Resulting failure can be dramatic in both social and economic terms, ranging from miscalculation of oil recovery rates or contaminant migration [5] to estimating incorrect elastic properties of carbon nanotubes patches [1].

We claim, with scientific positivism, that failures of standard continuum-scale models can be successfully addressed, and that such situations might represent an occasion for long-term reconciliation between the two schools of thought: whenever a *localized* breakdown of continuum-scale models occurs, hybrid models must be used to attain an increased rigor and accuracy in predictions, while keeping computational costs in check. Hybrid simulations [2, 6] resolve a small reactive region with a pore-scale model that is coupled to its continuum counterpart in the rest of a computational domain. (It is worthwhile pointing out that hybrid simulations are not applicable to transport phenomena

for which continuum models fail globally rather than locally either because "the connectivity of the pore space or a fluid phase plays a major role" or because of "long-range correlations in the system" [7, p. 1396].)

In the remainder of this chapter, we present a classification of the most common upscaling methods (section 1.2) that allow one to derive macroscopic equations from their pore-scale counterparts. In section 1.3, we report classical results of homogenization theory and their implications for applicability of macroscopic models. In the final section we discuss existing multiscale methods and their differences with hybrid algorithms.

1.2   Classification of upscaling methods

We consider crowded environments consisting of a solid matrix Ω_s and a fluid-filled pore space Ω_l. We define $\Omega := \Omega_s \cup \Omega_l$ and call it a *porous medium.* A major goal of upscaling is to establish connections between pore- and continuum-scale descriptions of transport processes in Ω.

Mathematical approaches to upscaling include the method of volume averaging [8] and its modifications [9], generalizations of the method of moments [10, 11, 12], homogenization via multiple-scale expansions [13], pore-network models [14], and thermodynamically constrained averaging [15].

Let u be a real-valued function on a pore-scale domain Ω_l that exhibits rapid spatial oscillations. It describes a certain physical quantity and satisfies a partial differential equation

$$\mathscr{L}[u] = f. \tag{1.1}$$

One can define the local average of u as

$$\langle u \rangle (\mathbf{x}) = \frac{1}{|\mathscr{V}|} \int_{\mathscr{V}(\mathbf{x})} u(\mathbf{y}) \mathrm{d}\mathbf{y}. \tag{1.2}$$

In the method of *volume averaging*, the support volume $\mathscr{V}$ "is a small, but not too small, neighborhood of point $\mathbf{x}$ of the size of a representative elementary volume, REV (several hundred or thousand of pores)" [16, p. 1]. The ambiguity in defining the size of an REV is typical. For example, in [17, p. 15] "the size of the REV is defined by saying that it is

- sufficiently large to contain a great number of pores so as to allow us to define a mean global property, while ensuring that the effects of the fluctuations from one pore to another are negligible. One may take, for example, 1 cm^3 or 1 dm^3;

- Sufficiently small so that the parameter variations from one domain to the next may be approximated by continuous functions, in order that we may use infinitesimal calculus."

A continuum-scale equation

$$\overline{\mathscr{L}}[\langle c \rangle] = g, \tag{1.3}$$

is constructed by volumetric averaging (1.2) of the original pore-scale equation (1.1). The procedure is facilitated by the spatial averaging theorem, which enables one to exchange spatial integration and differentiation [8],

$$\langle \nabla u \rangle = \nabla \langle u \rangle + \frac{1}{|\mathscr{V}|} \int_{A_{ls}} u \mathbf{n} \mathrm{d}A, \tag{1.4}$$

where A_{ls} is the liquid-solid interface contained in $\mathscr{V}$ and $\mathbf{n}$ is the outward normal unit vector of A_{ls}. A reference book on the method of volume averaging is [8].

Similar concepts are used in *thermodynamically constrained averaging theory* [15], wherein thermodynamics is introduced into a constrained entropy inequality to guide the formation of closed macroscale models that retain consistency with microscale physics and thermodynamics.

In the *homogeneization theory* by multiple-scale expansions (see, for example [16]), the volume $\mathscr{V}$ is the unit cell of a periodic porous medium Ω with period ϵ. A homogenized equation is obtained by determining the following limit,

$$\langle u \rangle = \langle \lim_{\epsilon \to 0} u_\epsilon \rangle, \tag{1.5}$$

where u_ϵ is the sequence (indexed by ϵ) of solutions of (1.1) with periodically oscillating coefficients. The limit is determined by utilizing a two-scale asymptotic expansion that "is an ansatz of the form,

$$u_\epsilon(\mathbf{x}) = u_0(\mathbf{x}, \mathbf{x}/\epsilon) + \epsilon u_1(\mathbf{x}, \mathbf{x}/\epsilon) + \epsilon^2 u_2(\mathbf{x}, \mathbf{x}/\epsilon) + \cdots \tag{1.6}$$

where each function $u_i(\mathbf{x}, \mathbf{y})$ in this series depends on two variables, $\mathbf{x}$ the macroscopic (or slow) variable and $\mathbf{y}$ the microscopic (or fast) variable, and is $\mathscr{V}$-periodic in $\mathbf{y}$ ($\mathscr{V}$ is the unit period). Inserting the ansatz (1.6) in the equation (1.1) satisfied by u_ϵ and identifying powers of ϵ leads to a cascade of equations for each term $u_i(\mathbf{x}, \mathbf{y})$. In general averaging with respect to $\mathbf{y}$ yields the homogenized equation for u_0. Another step is required to rigorously justify the homogenization result obtained heuristically with this two-scale asymptotic expansion" [16, p. 238].

Similar to the homogenization theory definition of average is that of the *methods of moments*, wherein the global ($\mathbf{x}$) and local ($\mathbf{y}$) variables "characterize the instantaneous position (configuration) of the Brownian particle in its phase space. Together the vectors ($\mathbf{x},\mathbf{y}$) define a multidimensional phase space $\mathbf{x} \oplus \mathbf{y}$ whithin which convective and diffusive solute-particle transport processes occur. The domain of permissible values of $\mathbf{x}$ will always be unbounded; in contrast, the domain of permissible or accessible values of $\mathbf{y}$ will generally be bounded" [18, p.66–67], i.e., $\mathbf{y} \in \mathscr{V}$. In this case, a macroscopic transport equation is obtained for the probability density function of a Brownian particle [18, eq. 3.3-5]

$$\overline{P}(\mathbf{x},t|\mathbf{y}') \overset{def}{=} \int_{\mathscr{V}} P(\mathbf{x},\mathbf{y},t|\mathbf{y}')\mathrm{d}\mathbf{y} \qquad (1.7)$$

where $P(\mathbf{x},\mathbf{y},t|\mathbf{y}') \equiv P(\mathbf{x}-\mathbf{x}',\mathbf{y},t-t'|\mathbf{y}')$ with $\mathbf{x}' = \mathbf{0}$ and $t' = 0$ denotes the "conditional probability density that the Brownian particle is situated at position ($\mathbf{x},\mathbf{y}$) at time t, given that it was initially introduced into the system at the position ($\mathbf{x}',\mathbf{y}'$) at some earlier time t' ($t > t'$)" [18, p.68]. "For sufficiently long times (i.e. 'long' relative to the time scale of evolution of the microscale transport process, but 'short' relative to the time scale of the macrotransport process) we expect that the particle(s) will loose memory of the initial position(s) $\mathbf{y}'$". Consequently, $\overline{P}(\mathbf{x},t|\mathbf{y}') \approx \overline{P}(\mathbf{x},t)$ and a fully macrotransport equation can be determined.

A number of other approaches to upscaling are reviewed in [18]. Even if based on different definitions of the averaging volume and on distinct mathematical tools, all upscaling methods require closure assumptions to decouple the average system behavior from the pore-scale information: the latter is exclusively incorporated into the upscaled equation through effective parameters that can be determined by laboratory experiments

or numerical solution of a closure problem at the unit cell level.

Next, we present classical results from homogenization theory applied to flow and transport problems.

1.3 From first principles to effective equations

1.3.1 Flow: from Stokes to Darcy/Brinkman equations

Single-phase flow of an incompressible Newtonian fluid in porous media in the pore-space Ω_l is described by the Stokes and continuity equations subject to the no-slip boundary condition on A_{ls},

$$\mu \nabla^2 \mathbf{v} - \nabla p = 0, \quad \nabla \cdot \mathbf{v} = 0, \quad \mathbf{x} \in \Omega_l, \qquad \mathbf{v} = \mathbf{0}, \quad \mathbf{x} \in A_{ls}, \tag{1.8}$$

where $\mathbf{v}(\mathbf{x})$ is the fluid velocity, p denotes the fluid dynamic pressure, and μ is the dynamic viscosity.

Upscaling of the Stokes equations (1.8) at the pore-scale to the continuum scale has been the subject of numerous investigations, including those relying on multiple-scale expansions [16, 19, 20, 21, 22, and references therein], volume averaging [23, and references therein], the method of moments, etc. These studies have demonstrated that Darcy's law, which was empirically established by Darcy in 1856 [24], and the continuity equation for $\langle \mathbf{v} \rangle$,

$$\langle \mathbf{v} \rangle = -\frac{\mathbf{K}}{\mu} \cdot \nabla \langle p \rangle, \qquad \nabla \cdot \langle \mathbf{v} \rangle = 0, \qquad \mathbf{x} \in \Omega, \tag{1.9}$$

provide an effective representation of the pore-scale Stokes flow (e.g., [16, Eq. 4.7]). Such upscaling procedures also enable one to formally define the permeability tensor $\mathbf{K}$ in (1.9) as the average of a "closure variable" $\mathbf{k}(\mathbf{y})$, i.e., $\mathbf{K} = \langle \mathbf{k}(\mathbf{y}) \rangle$. The latter is the unique solution of a local problem (e.g., [16, pp. 46-47, Theorem 1.1] and [19, Eq. 22]) defined on a representative (unit) cell of the porous medium. "It is well admitted that the existence of continuum behaviors that are macroscopically equivalent to finely heterogeneous media needs a good separation of scales. If l and L are the characteristic lengths at the local and the macroscopic scale, respectively, their ratio should obey" [25]

$$\epsilon = \frac{l}{L} \ll 1. \tag{1.10}$$

To describe flow through "hyperporous" media, Brinkman [26] introduced a modification of Darcy's law,

$$\nabla \langle p \rangle = -\frac{\mu}{\mathbf{K}} \langle \mathbf{v} \rangle + \mu_e \nabla^2 \langle \mathbf{v} \rangle, \tag{1.11}$$

where μ_e is an effective viscosity "which may differ from μ" [26]. The *raison d'etre* for such a modification was the necessity of obtaining an equation that was valid in the high permeability limit ($|\mathbf{K}| \to \infty$) and that allowed for a direct coupling with the Stokes equations at interfaces separating Stokes flow (infinite permeability regions) and filtration flow (low permeability regions). In Brinkman's words, "this equation has the advantage of approximating (1.9) for low values of $\mathbf{K}$ and (1.8) for high values of $\mathbf{K}$".

After its introduction and its widespread use, an increasing research effort was devoted to the identification of domains of validity of both Darcy's and Brinkman's law [27, 28, 29, and references therein]. Brinkman's intuition was mathematically proven later by Goyeau et al. [30] and Auriault et al. [25], who used respectively the method of volume averaging and multiple-scale expansions to demonstrate that Brinkman's equation represents a higher-order approximation of Darcy's law when the separation of scales is poor. Poor scale separation can be encountered in two typical situations. "The first one occurs when the porous medium is macroscopically heterogeneous, when the macroscopic characteristic length L associated to the macroscopic heterogeneities is not very large compared to the characteristic length l of the pores. For such media, length L can be estimated by $L \approx K/|\nabla K|$, where K is the permeability. When the macroscopic gradient of the permeability $|\nabla K|$ is large, the ratio l/L may not be very small and the separation of scale is poor. The second typical situation corresponds to large gradients of pressure which are applied to macroscopically homogeneous media. The macroscopic characteristic length $L \approx p/|\nabla p|$ associated to this gradient of pressure could be not very large compared to l" [25]. In a subsequent work, Auriault [28] defines the applicability range of Darcy's and Brinkman's equations in terms of the geometric parameters of three classes of porous media: classical porous media characterized by connected porous matrix (e.g. capillary tubes), swarms of fixed particles with connected pore space, and fribous media. It is finally concluded that the validity domain of Brikman's equation corresponds to porous media with very large porosity and very small solid concentration.

In Chapter 2 we show how continuum-scale models provide powerful predictive tools even on the nano-scale: we employ Brinkman's equation to describe flow through carbon nanotubes (CNTs) forests, and to predict elastic properties of CNTs patches with a high degree of fidelity. The current state-of-the-art in the field is to predict CNT deflections with computationally expensive molecular dynamics (MD) simulations [31, par. 2.4.5]. While MD simulations are capable of incorporating an accurate description of the structure and the dynamics at the atomistic level, they are computationally prohibitive when used to model CNTs of height greater than few tens of nanometers. Current laboratory techniques allow to grow CNTs to 100μm. The necessity for macroscopic models applicable to nanotechnology systems is stressed in a recent monograph on CNTs: "It turns out that currently there are no mesoscopic structural and dynamic methods especially suited for CNTs or composites based on CNTs" [31, par. 2.4.5, p. 45]. We show that such mesoscopic models do exist and can be successfully applied to nanotechnological devices.

1.3.2 Transport: from advection-diffusion to advection-dispersion equation

Let us now assume that the fluid contains a dissolved species $\mathcal{M}$, whose molar concentration $c(\mathbf{x}, t)$ $[molL^{-3}]$ at point $\mathbf{x} \in \Omega_l$ and time $t > 0$ changes due to advection, molecular diffusion, homogeneous reaction in the liquid phase and heterogeneous reaction at the solid-liquid interface A_{ls}. The first three phenomena are described by an advection-diffusion-reaction equation,

$$\frac{\partial c}{\partial t} + \mathbf{v} \cdot \nabla c = \nabla \cdot (\mathbf{D}\nabla c) + R(c), \qquad \mathbf{x} \in \Omega_l, \quad t > 0, \tag{1.12}$$

where the molecular diffusion coefficient $\mathbf{D}$ is, in general, a positive-definite second-rank tensor. If diffusion is isotropic, $\mathbf{D} = \mathscr{D}_m\mathbf{I}$ where $\mathscr{D}_m$ $[L^2T^{-1}]$ is the diffusion coefficient and $\mathbf{I}$ is the identity matrix. The source term $R(c)$ represents a generic homogeneous reaction. At the solid-liquid interface A_{ls} impermeable to flow, mass conservation requires that mass flux of the species $\mathcal{M}$ be balanced by net mass flux due to heterogeneous

reaction, $Q(c)$,

$$-\mathbf{n} \cdot \mathbf{D}\nabla c = Q(c), \qquad \mathbf{x} \in A_{ls}. \tag{1.13}$$

In addition to (1.13), flow and transport equations (1.8) and (1.12) are supplemented with boundary conditions on the external boundary of the flow domain Ω. The upscaling of (1.12) and (1.13) leads to effective equations for the average concentration $\langle c \rangle$, generally written in the following form

$$\frac{\partial \langle c \rangle}{\partial t} + \langle \mathbf{v} \rangle \cdot \nabla \langle c \rangle = \nabla \cdot (\mathbf{D}\nabla \langle c \rangle) + \overline{R}(\langle c \rangle) + \overline{Q}(\langle c \rangle), \qquad \mathbf{x} \in \Omega, \quad t > 0, \tag{1.14}$$

where $\overline{R}(\langle c \rangle)$ and $\overline{Q}(\langle c \rangle)$ are effective reactive sources.

A significant research effort and ingenuity has been devoted to the upscaling of various functional forms of $R(c)$ and $Q(c)$ relevant to engineering, chemical, biochemical, hydrological, and other applications [10, 11, 32, 12, 33, 34, 35, 36]. Yet, very little, and only recent, attention has been paid to the identification of the applicability conditions of the upscaled models proposed by such a prolific research path.

While useful in a variety of applications, continuum models fail to capture experimentally observed transport features, including a difference between fractal dimensions of the diffusion and dispersion fronts (isoconcentration contours) [37], long tails in breakthrough curves [38], and the onset of instability in variable density flows [39]. ADE-based models of transport of (bio-)chemically reactive solutes, which are the focus of our analysis, can significantly over-predict the extent of reactions in mixing-induced chemical transformations [40, 34, 3, 41, 42, and references therein]. These and other shortcomings stem from the inadequacy of either standard macroscopic models or their parametrizations or both. Upscaling from the pore-scale, on which governing equations are physically based and well defined, to the continuum scale, on which they are used for qualitative predictions, often enables one to establish the connection between the two modeling scales.

Upscaling approaches that rely on characteristic dimensionless numbers (e.g., the Damköhler and Péclet numbers) can provide quantitative measures for the validity of various upscaling approximations. Auriault and Adler [19] used multiple scale expansions to establish the applicability range of advection-dispersion equation for a

non-reactive solute in terms of Péclet number. Mikelić et al. [20] provided a rigorous upscaled version of the Taylor dispersion problem with linear heterogeneous reaction. For flow between two parallel reacting plates they established the applicability range of the upscaled equation in terms of Damköhler and Peclet numbers.

Nonlinearity of governing equations complicates the upscaling of most reactive transport phenomena. It requires a linearization and/or other approximations, whose accuracy and validity cannot be ascertained a priori. This is especially so for a large class of transport processes, such as mixing-induced precipitation, which exhibit highly localized reacting fronts and consequently defy macroscopic descriptions that are completely decoupled from their microscopic counterparts [32, 19, 9].

In Chapters 3 and 4, we generalize results from [19] and [20] to nonlinear reactive processes. In Chapter 3 we consider a multicomponent system undergoing nonlinear homogeneous and linear heterogeneous reaction described by a system of coupled reaction-diffusion equations (RDEs); we specify key physical and (bio-) chemical assumptions that underpin this model and identify Damköhler numbers for homogeneous and heterogeneous reactions as dimensionless parameters that control the phenomenon. We use the local volume averaging [8] to derive a system of upscaled RDEs that are commonly used to model mixing-induced precipitation on the continuum scale, e.g., [43, and the references therein]. The goal here is to identify sufficient conditions for the macroscopic RDEs to be a valid descriptor of mixing-induced precipitation. To focus on the relative effects of nonlinear geochemical reactions and diffusion, we neglect advection.

In Chapter 4 we consider the advective-diffusive transport of a solute that undergoes a nonlinear heterogeneous reaction: after reaching a threshold concentration value, it precipitates on the solid matrix to form a crystalline solid. The relative importance of three key pore-scale transport mechanisms (advection, molecular diffusion, and reactions) is quantified by the Péclet (Pe) and Damköhler (Da) numbers. We use multiple-scale expansions to upscale a pore-scale advection-diffusion equation with reactions entering through a boundary condition on the fluid-solid interface, and to establish sufficient conditions under which macroscopic advection-dispersion-reaction equations (ADREs) provide an accurate description of the pore-scale processes. These conditions are summarized by a phase diagram in the (Pe, Da) space, parameterized with a scale-

separation parameter that is defined as the ratio of characteristic lengths associated with the pore- and macro-scales.

Having criteria to identify subdomains where continuum-scale equations break down, we can proceed by formulating an hybrid model. Before doing that, we review the state-of-art on multiscale methods in the following section.

1.4   Multiscale models

The search for ways to combine the physical rigor of pore-scale modeling with the computational efficiency of its continuum-scale counterpart and to model phenomena where the small-scale processes significantly affect large-scale behavior (e.g., material deposition, fracture dynamics) has motivated the development of hybrid pore-scale/continuum-scale algorithms, e.g., [2, 6], and multi-scale approaches, e.g., [44, 45, 46, 47, 48, 49, 50, 51].

It is important to distinguish hybrid algorithms from multiscale numerical approaches that are based on empirical closures [47], upscaling methods [44] and/or assumed macroscopic behavior of microscopic variables [52]. Multiscale algorithms employ "effective" representations of pore-scale processes, which share many approximations and assumptions with continuum models. On the other hand, hybrid algorithms assume a local breakdown of continuum-scale representations and, consequently cannot rely on any of the assumptions on which the latter are based in order to formulate the coupling between the two scales.

Hybrid models provide significant computational speed-up when the sub-domain Ω_p wherein pore-scale simulations are required (i.e., wherein continuum models become invalid) is much smaller than the total computational domain Ω. The inequality [53, 54],

$$\frac{||\Omega_{pc}||}{||\Omega|| - ||\Omega_p||} \frac{C_{pc}}{C_p} \ll 1,$$

provides a more precise formulation of this statement. Here $||\Omega||$, $||\Omega_p||$, and $||\Omega_{pc}||$ are the volumes of Ω, Ω_p, and the "handshake" region Ω_{pc} wherein both continuum and pore-scale simulations are coupled, respectively; and C_p and C_{pc} are the computational costs per unit volume for pore-scale and coupling simulations, respectively. This condition

takes advantage of the fact that the computational cost of continuum-scale simulations is much smaller than that of pore-scale simulations. As pointed out in [53], a hybrid algorithm is beneficent "even if the algorithmic interface is computationally more expensive than either algorithm, as long as the interface region and the region using the more expensive method are each small fractions of the total volume." The latter condition is satisfied in highly localized flow and transport phenomena, such as flow and transport to/from point sources, and propagation of reactive fronts. Tools for identifying the regions wherein continuum models break down, Ω_p, are developed in Chapters 3 and 4 (see, also, [55, 56]).

Hybrids for reaction-diffusion systems, including [57, 58, 2], couple molecular dynamics (MD) and kinetic Monte Carlo simulations, MD and reaction-diffusion equation, and lattice Boltzmann and reaction-diffusion equation. Smoothed Particle Hydrodynamics (SPH) was used to incorporate moving boundary effects due to precipitation processes at the pore-scale [6]. An advantage of SPH over MD lies in requiring a significantly smaller number of particles (and consequently smaller computational costs) to properly model the hydrodynamics of a continuum fluid: this derives from the mesoscopic nature of SPH particles that are, in fact, a collection of MD particles. However if the Lagrangian particle nature of SPH allows physical and chemical effects to be incorporated into the modeling of flow processes with relatively little code-development efforts, additional complications might arise in the formulation of the coupling boundary conditions in presence of advection: each particle (both at the pore- and continuum-scale) moves in space with its own velocity (Stokes or Darcy) and coupling based on superposition of particle spheres of influence becomes unclear.

In the third part of this dissertation, we instead formulate a coupling in a fully Eulerian framework. We show that this formulation, combined with the volume averaging method, gives rise to a natural and efficient coupling between pore- and continuum-scale computations at the modeling interface. We present two hybrid algorithms with and without overlapping that couple pore-scale simulations in a small domain Ω_p with continuum simulations elsewhere in the computational domain, Ω/Ω_p. The coupling is accomplished via an iterative procedure to ensure the continuity of state variables and their fluxes across the interface between Ω_p and the rest of the computational domain. In

Chapter 5 the hybrid formulation with overlapping and its numerical implementation are applied to model Taylor dispersion in a planar fracture with chemically reactive walls. We use this well-studied problem to validate our hybrid algorithm via comparison with analytical solutions and two-dimensional pore-scale numerical simulations. In Chapter 6 a formalization for a hybrid model without overlapping is developed.

Chapter 2

Continuum Description of Systems at the Nanoscale

2.1 Introduction

Carbon nanotubes (CNTs) possess a remarkable combination of mechanical characteristics, such as exceptionally high elastic moduli [59], reversible bending and buckling characteristics [60], and superplasticity [61]. These properties insure that complex interactions between fluid flow and patterned nanostructures composed of CNTs play an important role in a variety of applications, including mechanical actuators [62], chemical filters [63], and flow sensors [64]. When placed on a body's exterior, CNT "forests" can act as superhydrophobic surfaces that significantly reduce drag [65] thanks to a linear dependence of the slip length on lateral length scales [66]. Observations of fluid flow past CNTs [1] suggest the potential use of CNT forests as sensors of tactile and shear forces.

Predictive and diagnostic capabilities of nano-sensors and other nano-forest covered surfaces are hampered by the relative lack of quantitative understanding of their response to hydro- or aerodynamic loading. Most experiments dealing with these phenoma assemble CNTs into macroscopic sheets or forests [67]. Yet their outcomes (data) are often interpreted with theoretical models that neglect crowding effects by employing the Stokes solution of flow past a single infinite cylinder in either analytical analysis [1, Eqs. 4 and 7] or molecular dynamics simulations [4, Eq. 4]. Attempts to account for crowding

effects by modifying the drag coefficient of each CNT are essentially phenomenological and treat CNTs as infinite cylinders, e.g. [4, 68, 1, and references therein].

The purpose of the present work is to predict the elastic response of CNT forests to ambient laminar and turbulent fluid flows and to employ these predictions to estimate CNTs' flexural rigidity from the data collected in the experimental apparatus of [1], which is shown in Fig. 2.1. The concept of flexural rigidity is routinely used to forecast the deflection and buckling behaviors of elastic bodies [69], including CNTs. Indeed, their observations of deformations of CNT forests with a scanning electron microscope revealed that in situ shearing can be conceptualized as the deflection of a cantilever (Fig. 2.2).
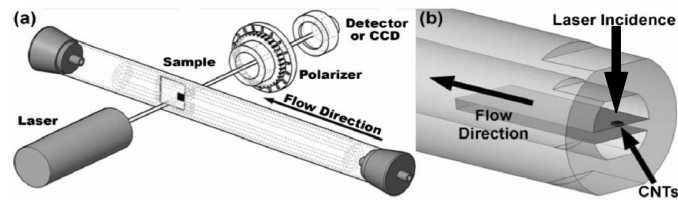
Figure 2.1: Experimental setup used by [1].
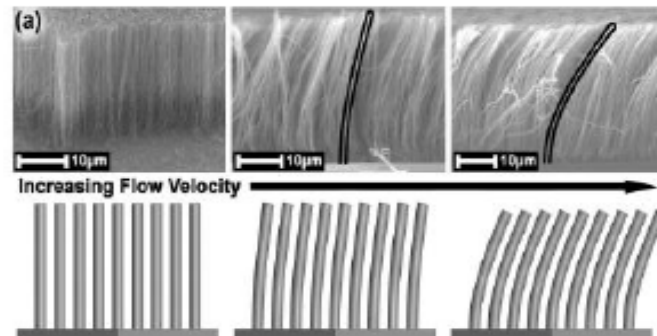
Figure 2.2: Scanning electron microscope (SEM) imaging of in situ shearing of CNT forests, and their representation with a cantilever, after [1].

We develop a closed-form analytical description of fully developed steady-state fluid flow over and through CNT forests, which are used to estimate the average drag coefficient, bending profile and, ultimately, flexural rigidity of individual CNTs. The incompressible Navier-Stokes equations are used to describe laminar or turbulent flow above the forest, with the porous medium Brinkman equation representing flow through

the forest. A viscosity ratio parameter in the Brinkman equation [70] accounts for slip effects at nanotube walls.

In section 2.2, we describe the experimental setup used by [1] and formulate a continuum model for flow past an infinite array of single-walled CNTs, and their individual bending profiles. This section also identifies a viscosity ratio, porosity (spacing between CNTs), the Reynolds number for porous flow in CNT forests, and the corresponding Darcy number as dimensionless parameters that control the phenomenon. Section 2.3 contains analytical solutions for velocity profiles and resulting shear stress and drag coefficients. Closed-form, analytical expressions for the CNT bending profiles are presented in section 2.4. In section 2.5, our theoretical predictions are compared with the experimental data of [1] and are employed to estimate a CNT's flexural rigidity. The main results and conclusions are summarized in section 2.6.

2.2 Experimental setup and model formulation

2.2.1 Experimental apparatus

A detailed description of the synthesis and patterning of the arrays of vertically aligned, multi-walled CNTs can be found in [1]. CNTs, with typical heights $H \in [40 - 60]\mu$m and diameters $2R_0 \in [30 - 50]$nm, were grown in square arrays of sizes 5-10μm on quartz substrates (see Fig. 2.3). The CNT samples were placed inside of the experimental apparatus shown in Fig. 2.1, at the center of a quartz tube with inner diameter of 6.2mm at the front edge of the substrate; appropriate measures [1] were taken to prevent the sample vibration or fluid flow entrance effects. The samples were then exposed to fluid (air) at various pressures, and fluid velocities were calibrated using the flow chamber cross-sectional area and volumetric flow rates as measured by a flow meter. A linearly polarized He-Ne laser ($\lambda = 633$nm) was used to illuminate the CNT forests and the transmitted light intensity was monitored as a function of fluid flow. As the axis of the polarizer was initially oriented parallel to the laser polarization direction, the deflections of the CNT ensembles (initially oriented parallel to the polarized laser beam) was translated into a change of the light intensity and sampled by a photodetector or a charge coupled device (CCD) camera. Multiple measurements and averaging of the

obtained deflections lowers the error in the recorded deflections; e.g., at the upper air velocity limit of ≈ 65m/s, the displacement error on the order of $\pm 0.5\mu$m was observed.

2.2.2 Model formulation

To model the experiment, we consider a fully developed incompressible fluid flow between two infinite parallel plates separated by the distance of $H + 2L$ (Fig. 2.4). The bottom part of the flow domain, $-H < \hat{y} < 0$, is occupied by square-patterned arrays of CNTs (Fig. 2.3). The flow is driven by an externally imposed (mean) constant pressure gradient $\mathrm{d}\hat{p}/\mathrm{d}\hat{x} < 0$.
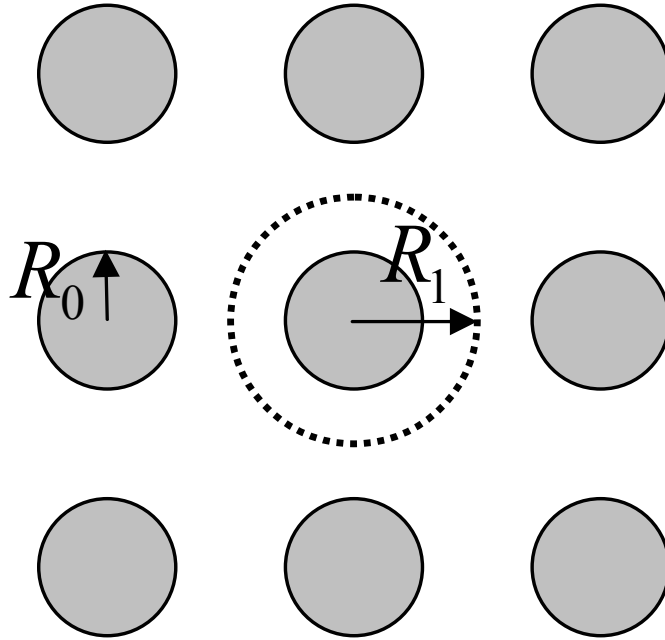
Figure 2.3: Carbon nanotubes of external radius R_0 are grown in square arrays. R_1 represents the midway distance between aligned nanotubes.

Fluid flow

We treat the nano-forest, i.e., the region occupied by carbon nanotubes, as a porous medium with porosity $\phi = 1 - (R_0/R_1)^2$ and permeability K. The flow in this region, $\hat{y} \in (-H, 0)$, can be described by the Brinkman equation for the horizontal
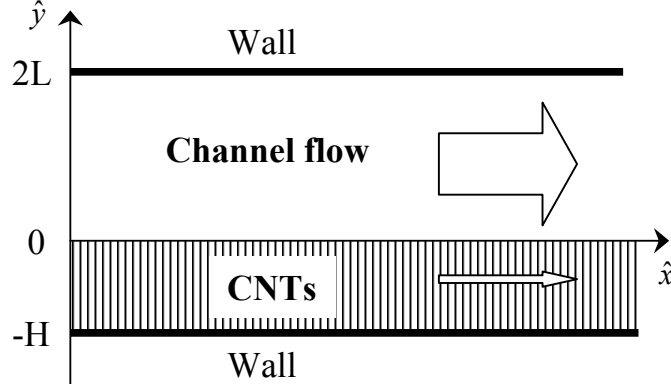
Figure 2.4: The schematic of the problem (not in scale). Fluid flows in a channel. At its bottom wall CNTs are uniformly grown. The computational domain is here represented and divided into two regions: the channel flow region for $\hat{y} \in (0, 2L)$ and the region occupied by CNTs for $\hat{y} \in [-H, 0]$.

component of the intrinsic average velocity $\hat{u}$ [28],

$$\mu_e \frac{\mathrm{d}^2 \hat{u}}{\mathrm{d}\hat{y}^2} - \frac{\mu}{K} \hat{u} - \frac{\mathrm{d}p}{\mathrm{d}x} = 0, \quad \hat{y} \in (-H, 0), \tag{2.1}$$

where μ is the fluid's dynamic viscosity, and μ_e is its "effective" viscosity that accounts for the slip at the CNTs walls [70]. Since the experimentally observed maximum bending of the CNTs is about 10% of their length, we assume that bending has a negligible effect on permeability. This allows us to decouple an analysis of the flow from that of the mechanics of the bending. This assumption will be validated in section 2.5 by comparing the model predictions with the experimental data. Expressing the permeability of square arrays of infinite cylinders [71, Eq. 19] in terms of porosity ϕ, we obtain

$$K = \frac{R_1^2}{8} \left[-\ln(1 - \phi) - \frac{(1 - \phi)^{-2} - 1}{(1 - \phi)^{-2} + 1} \right]. \tag{2.2}$$

In the rest of the flow domain, $\hat{y} = [0, 2L]$, we use either Navier-Stokes or Reynolds equations to describe fully developed flow respectively in either laminar ($\gamma = 0$) or turbulent ($\gamma = 1$) regimes [72, Eq. 7.8],

$$\mu \frac{\mathrm{d}^2 \hat{u}}{\mathrm{d}\hat{y}^2} - \gamma \rho \frac{\mathrm{d}\langle \hat{u}' \hat{v}' \rangle}{\mathrm{d}\hat{y}} - \frac{\mathrm{d}p}{\mathrm{d}x} = 0, \qquad \hat{y} \in (0, 2L), \tag{2.3}$$

where ρ is the fluid density and $\hat{u}(\hat{y})$ is the horizontal component of flow velocity $\hat{\mathbf{u}}(\hat{u}, \hat{v})$. In the laminar regime, $\hat{u}$ is the actual velocity and $\hat{v} \equiv 0$. In the turbulent regime,

$\hat{\mathbf{u}}$ denotes the mean velocity, $\mathrm{d}p/\mathrm{d}x$ is the mean pressure gradient, $\hat{u}'$ and $\hat{v}'$ are the velocity fluctuations about their respective means, and $\langle \hat{u}'\hat{v}' \rangle$ is the Reynolds stress. Fully-developed turbulent channel flow has velocity statistics that depend on $\hat{y}$ only.

In both flow regimes, the no-slip condition is imposed at $\hat{y} = -H$ and $\hat{y} = 2L$, and the continuity of velocity and shear stress is prescribed at the interface, $\hat{y} = 0$, between the free and filtration flows [73]:

$$\hat{u}(-H) = 0, \quad \hat{u}(2L) = 0, \quad \hat{u}(0^-) = \hat{u}(0^+) = \hat{U}, \quad \mu_e\left(\frac{\mathrm{d}\hat{u}}{\mathrm{d}\hat{y}}\right)_{\hat{y}=0^-} = \mu\left(\frac{\mathrm{d}\hat{u}}{\mathrm{d}\hat{y}}\right)_{\hat{y}=0^+} \quad (2.4)$$

where $\hat{U}$ is an unknown matching velocity at the interface between channel flow and porous medium.

Let us introduce a characteristic Darcy velocity $q = -(H^2/\mu)\mathrm{d}p/\mathrm{d}x$ and define dimensional quantities

$$u = \frac{\hat{u}}{q}, \quad y = \frac{\hat{y}}{H}, \quad \epsilon = \frac{R_1}{H}, \quad \delta = \frac{L}{H}, \quad \mathrm{M} = \frac{\mu_e}{\mu}, \quad Da = \frac{K}{H^2}, \quad Re_p = \frac{\rho Hq}{\mu}, \quad (2.5)$$

where Da is the Darcy number e.g., [74, Eq. 6] and Re_p is the Reynolds number for porous flow. Then the flow equations (2.1)–(2.4) can be rewritten in a dimensionless form

$$\mathrm{M}\frac{\mathrm{d}^2u}{\mathrm{d}y^2} - \frac{u}{Da} + 1 = 0, \qquad\qquad y \in (-1, 0) \qquad\qquad (2.6)$$

$$\frac{\mathrm{d}^2u}{\mathrm{d}y^2} - \gamma Re_p\frac{\mathrm{d}\langle u'v'\rangle}{\mathrm{d}y} + 1 = 0, \qquad\qquad y \in (0, 2\delta). \qquad\qquad (2.7)$$

subject to the boundary conditions

$$u(-1) = 0, \quad u(2\delta) = 0, \quad u(0^-) = u(0^+) = U, \quad \mathrm{M}\frac{\mathrm{d}u}{\mathrm{d}y}(0^-) = \frac{\mathrm{d}u}{\mathrm{d}y}(0^+), \qquad (2.8)$$

where $U = \hat{U}/q$ is an unknown dimensionless velocity at the interface between the free and porous flows.

The dimensionless version of (2.2) allows one to express the Darcy number Da in terms of porosity ϕ and the geometric factor ϵ,

$$Da = \frac{\epsilon^2}{8}\left[-\ln\left(1 - \phi\right) - \frac{(1-\phi)^{-2} - 1}{(1-\phi)^{-2} + 1}\right]. \qquad (2.9)$$

The limit of $Da \to 0$ corresponds to the diminishing flow through the nanotube forest due to decreasing permeability $K \to 0$ or, equivalently, porosity $\phi \to 0$, i.e., due to very dense

packing of carbon nanotubes. In this limit, the Brinkman correction term $\mathrm{M}\mathrm{d}^2 u/\mathrm{d}y^2$ in (2.6) becomes negligible and (2.6) reduces to Darcy's law. The limit of $Da \to \infty$ corresponds to free flow and (2.6) reduces to the Stokes equation. According to (2.9) and its graphical representation in Figure 2.5, $Da \ll 1$ for $\epsilon < 1$ regardless of the magnitude of ϕ. This implies that crowding effects cannot be neglected for arrays of obstacles, whose geometric ratio $\epsilon \leq 1$. Even in high porosity CNT patches ($\phi \approx 0.8 - 0.9$), common values of $\epsilon \approx 10^{-2} - 10^{-3}$ give rise to $Da \approx 10^{-5} - 10^{-7}$.
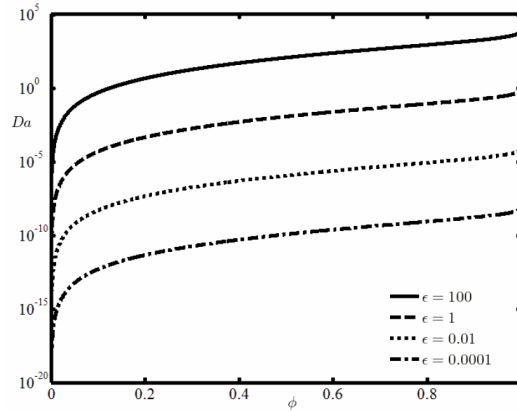
Figure 2.5: The Darcy number Da as a function of porosity ϕ and geometric factor ϵ.

Elastic bending of nanotubes

Let $\hat{l}(\hat{y})$ denote the horizontal deflection of an individual CNT at the elevation $\hat{y} \in [-H, 0]$. The deflection is caused by the force (drag) $\hat{\mathscr{D}}(\hat{y})$ exerted by the fluid on the CNT at the elevation $\hat{y}$. By treating the elastic CNT with the Young modulus $\hat{E}$ as a cantilever and denoting the moment of inertia of the CNT's cross section with $\hat{I}$, the deflection $\hat{l}(\hat{y})$ can be found [1] as a solution of

$$\frac{\mathrm{d}^2}{\mathrm{d}\hat{y}^2}\left(\hat{E}\hat{I}\frac{\mathrm{d}^2\hat{l}}{\mathrm{d}\hat{y}^2}\right) = \hat{\mathscr{D}}(\hat{y}), \tag{2.10}$$

subject to the boundary conditions

$$\hat{l}(-H) = 0, \qquad \frac{\mathrm{d}\hat{l}}{\mathrm{d}\hat{y}}(-H) = 0, \qquad \frac{\mathrm{d}^2\hat{l}}{\mathrm{d}\hat{y}^2}(0) = 0, \qquad \frac{\mathrm{d}^3\hat{l}}{\mathrm{d}\hat{y}^3}(0) = 0. \tag{2.11}$$

The first two conditions imply zero deflection and zero slope at the nanotube's fixed end $\hat{y} = -H$, respectively. The remaining two conditions correspond to zero bending moment and zero shear at the free end $\hat{y} = 0$, respectively. The product $\hat{E}\hat{I}$ is called the flexural rigidity of an individual CNT.

The drag force per horizontal unit area exerted by the fluid on any cross-section $\hat{y} = \text{const}$ is given by the xy-component of the stress tensor $\hat{\sigma}_{xy}(y)$,

$$\hat{\sigma}_{xy} = \alpha_\mu \frac{\mathrm{d}\hat{u}}{\mathrm{d}\hat{y}}, \tag{2.12}$$

where $\alpha_\mu = \mu_e$ for $\hat{y} \in [-H, 0)$, and $\alpha_\mu = \mu$ for $\hat{y} \in [0, 2L]$. The drag force distribution along an individual carbon nanotube, $\hat{\mathscr{D}}(\hat{y})$ in (2.10), is obtained as

$$\hat{\mathscr{D}} = \hat{\sigma}_{xy}/\hat{\mathscr{N}} = \mu_e R_1 \frac{\mathrm{d}\hat{u}}{\mathrm{d}\hat{y}}, \tag{2.13}$$

where $\hat{\mathscr{N}} = 1/R_1$ is the number of CNTs per unit length, and R_1 is the radius of the unit cell defined in Fig. 2.3.

Rewriting (2.10)–(2.13) in terms of the dimensionless quantities (4.5) and introducing new ones,

$$l = \frac{\hat{l}}{H}, \qquad \sigma_{xy} = \frac{\hat{\sigma}_{xy}H}{q\mu}, \qquad \mathscr{D} = \epsilon\mathrm{M}\frac{\mathrm{d}u}{\mathrm{d}y}, \qquad EI = \frac{\hat{E}\hat{I}}{H^3\mu q} \tag{2.14}$$

we obtain

$$\frac{\mathrm{d}^2}{\mathrm{d}y^2}\left(EI\frac{\mathrm{d}^2l}{\mathrm{d}y^2}\right) = \mathscr{D}, \qquad y \in (-1, 0), \tag{2.15}$$

subject to the boundary conditions

$$l(-1) = 0, \qquad \frac{\mathrm{d}l}{\mathrm{d}y}(-1) = 0, \qquad \frac{\mathrm{d}^2l}{\mathrm{d}y^2}(0) = 0, \qquad \frac{\mathrm{d}^3l}{\mathrm{d}y^3}(0) = 0. \tag{2.16}$$

2.3 Solution of the flow problem

2.3.1 Flow in the CNT forest

Velocity distribution inside the CNT forest is obtained by integrating the Brinkman equation (2.6) subject to the first and third boundary conditions (2.8)

$$u(y) = Da + C_1 e^{\lambda y} + C_2 e^{-\lambda y}, \qquad y \in [-1, 0], \tag{2.17a}$$

where $\lambda = 1/\sqrt{\mathrm{M}Da}$ and

$$C_1 = \frac{(U - Da)\mathrm{e}^{\lambda} + Da}{\mathrm{e}^{\lambda} - \mathrm{e}^{-\lambda}}, \qquad C_2 = -\frac{(U - Da)\mathrm{e}^{-\lambda} + Da}{\mathrm{e}^{\lambda} - \mathrm{e}^{-\lambda}}. \qquad (2.17\mathrm{b})$$

The unknown velocity U at the interface $y = 0$ between the porous and free flows is determined by matching the flow in the CNT forest (2.17) with the free flow. Velocity profiles for the latter are derived in the following section for laminar and turbulent regimes.

2.3.2 Flow above the CNT forest

Laminar regime

A solution of the flow equation (2.7) with $\gamma = 0$ subject to the second and third boundary conditions (2.8) is

$$u(y) = -\frac{y^2}{2} + \left(\delta - \frac{U}{2\delta}\right) y + U, \quad y \in [0, 2\delta]. \qquad (2.18)$$

The interfacial velocity U is obtained from the continuity of the shear stress at $y = 0$, the last boundary condition (2.8), as

$$U = Da\frac{1 - \mathrm{sech}\lambda}{\beta} + \frac{\delta}{\lambda\mathrm{M}}\frac{\tanh\lambda}{\beta}, \qquad \beta = 1 + \frac{\tanh\lambda}{2\delta\lambda\mathrm{M}}. \qquad (2.19)$$

The velocity distribution inside the CNT forest is now uniquely defined by combining (2.17) and (2.19).

Figure 2.6 represents the resulting velocity profiles for $\mathrm{M} = 1$, $\epsilon = 0.001$, $\delta = 100$, and several values of the Darcy number Da. Figure 2.6 shows the effect of crowding on velocity profile: small Darcy number Da corresponds to a plug-flow regime with uniform velocity (i.e. Darcy velocity) almost everywhere in the computational domain; for increasing values of Da the velocity profile tends to Poiseuille flow solution (i.e. parabolic profile).

Turbulent regime

A number of solutions of (2.7) with $\gamma = 1$ can be found in chapter 7 of [72]. Assuming the top of the CNT forest to be hydrodynamically smooth, the dimensionless
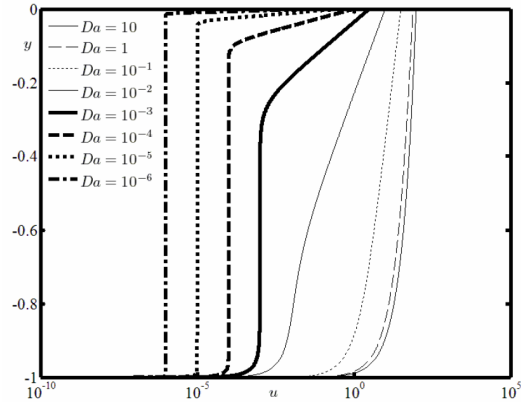
Figure 2.6: Laminar regime: dimensionless velocity profile $u(y)$ inside the CNT forest for M $= 1$, $\epsilon = 0.001$, $\delta = 100$, and several values of the Darcy number Da.

mean velocity u in the viscous sublayer of dimensionless width δ_ν obeys the *law of the wall* [72, pp. 270-271],

$$u(y) = \delta y + U, \qquad y \in [0, \delta_\nu]. \tag{2.20}$$

The continuity of the shear stress at $y = 0$, i.e., the last boundary condition (2.8), yields an expression for the dimensionless interfacial velocity,

$$U = Da(1 - \text{sech}\lambda) + \frac{\delta}{\lambda M} \tanh \lambda. \tag{2.21}$$

The comparison of (2.19) and (2.21) reveals that the interfacial velocities U in the laminar and turbulent regimes differ by the factor β. One can verify that $\beta \to 1$ as the Darcy number $Da \to 0$, i.e. when the permeability and porosity of CNT forests become small. For such conditions, equation (2.21) represents a good approximation of (2.19).

2.3.3 Shear stress, drag coefficient, and hydrodynamic load

The dimensionless drag force per unit length of a CNT (or the corresponding shear stress) is obtained by substituting (2.17) into (2.14)

$$\mathscr{D}(y) = \epsilon \lambda M \left(C_1 e^{\lambda y} - C_2 e^{-\lambda y} \right), \qquad y \in [1, 0], \tag{2.22}$$

The distribution of dimensionless shear stress σ_{xy} along a single CNT is shown in Fig. 2.7.
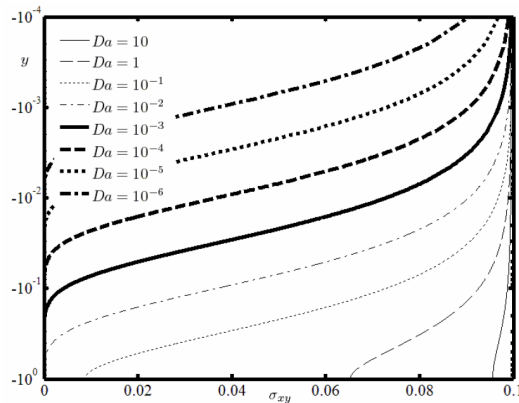
Figure 2.7: Dimensionless shear stress σ_{xy} along an individual CNT for M = 1, $\epsilon = 0.001$, $\delta = 100$, and several values of the Darcy number Da.

Integrating (2.22) over the length of the CNT, we obtain the total dimensionless drag force exerted by the fluid on the CNT, $\mathscr{F} = \epsilon M U$. The dimensional drag $\hat{\mathscr{F}}$, $[LM/T^2]$, which can also be obtained directly from (2.13), is given by $\hat{\mathscr{F}} = R_1 \mu_e Q$. Defining a drag coefficient C_D as the ratio between $\hat{\mathscr{F}}$ and $A\rho q^2/2$, where $A = 2R_0 H$ is the CNT surface area projected onto a plane normal to the velocity vector, we arrive at

$$C_D = \frac{1}{Re_p} \frac{MU}{\sqrt{1-\phi}}. \tag{2.23}$$

Expression (2.23) expresses the drag coefficient of an individual CNT in terms of the porosity of a CNT forest ϕ, the Reynolds number for the porous flow Re_p, and the dimensionless velocity at the interface separating the free and porous flows. To the best of our knowledge, this is the first rigorously derived formula for the drag coefficient for arrays of *finite* cylinders under *non uniform* flow conditions. Previous results hold for infinite cylinders or spheres in velocity field that is uniform on average.

2.4 Elastic CNT bending

Accounting for the boundary conditions (2.16), integration of (2.15) whose right-hand-side is given by (2.22) yields a dimensionless bending profile of individual CNTs,

$$l(y) = \frac{1}{2EI}\left[2I_4(y) - \frac{I_1(0)}{3}y^3 - I_2(0)y^2 + Ay + \frac{B}{3}\right], \tag{2.24}$$

where $A = I_1(0) - 2I_2(0) - 2I_3(-1)$, $B = 2I_1(0) - 3I_2(0) - 6I_3(-1) - 6I_4(-1)$,

$$I_n(y) = \epsilon \mathrm{M}\lambda^{1-n}\left[C_1 e^{\lambda y} + (-1)^{n+1}C_2 e^{-\lambda y}\right], \qquad n = 1,\ldots,4, \tag{2.25}$$

and C_1 and C_2 are defined by (2.17b). The corresponding dimensionless bending profiles are shown in Figure 2.8 for several values of the Darcy number Da.
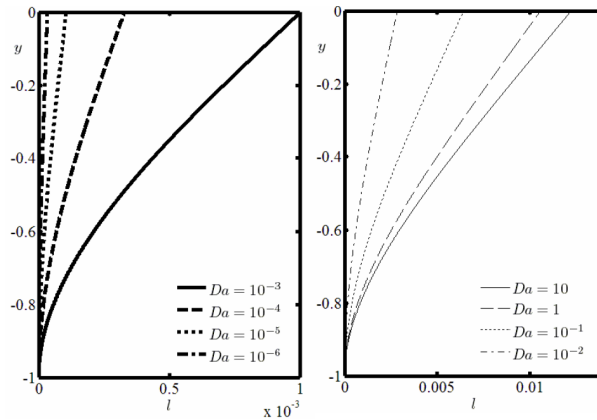
Figure 2.8: Dimensionless CNT bending profiles for M $= 1$, $\epsilon = 0.001$, $\delta = 100$, U defined by (2.19), and several Darcy numbers Da.

2.5 Comparison with experimental data

The experimental data reported by [1] consist of measurements of deflection of the CNT tips and bulk velocity across the wind tunnel. The latter is computed in section 2.5.1. The former, $\hat{X} = \hat{l}(0)$, is used to validate the model and to determine the flexural rigidity of CNTs in section 2.5.2. The experiments were conducted in turbulent

regimes, and were used to estimate the flexural rigidity $\hat{E}\hat{I}$ of five CNT samples, whose length $\hat{H}$ ranged from $40\mu m$ to $60\mu m$.

2.5.1 Average flow velocity across the wind tunnel

Purpose of this section is to relate the Darcy velocity q to measurements of an average velocity. Let us define a dimensionless bulk velocity across the wind tunnel as

$$u_{\mathrm{b}} = \frac{1}{1+2\delta} \int_{-1}^{2\delta} u(y)\mathrm{d}y, \tag{2.26}$$

and the corresponding dimensional bulk velocity as $\hat{u}_{\mathrm{b}} = u_{\mathrm{b}}q$. Substituting (2.17) into (2.26), we obtain

$$u_{\mathrm{b}} = \frac{1}{1+2\delta}\left[Da + \frac{U-2Da}{\lambda}\left(\coth\lambda - \mathrm{csch}\lambda\right)\right] + \frac{2\delta}{1+2\delta}u_{\mathrm{av}}, \quad u_{\mathrm{av}} = \frac{1}{2\delta}\int_0^{2\delta} u(y)\mathrm{d}y. \tag{2.27}$$

In the laminar flow regime, the dimensionless average velocity of the free flow, $u_{\mathrm{av}} = \hat{u}_{\mathrm{av}}/q$, can be readily evaluated since the velocity profile $u(y)$ on the interval $0 \leq y \leq 2\delta$ is given by (2.18). In the turbulent regime that characterizes the [1] experiment, $u(y)$ is determined by (2.20) only on the portion of this interval, i.e, on the interval $0 \leq y \leq \delta_\nu$.

We find u_{av} in the turbulent regime by assuming that the effects of the slip velocity U on u_{av} are negligibly small. This allows us to employ a relationship between the friction velocity $\hat{u}_\tau \equiv \sqrt{-(L/\rho)\mathrm{d}p/\mathrm{d}x}$ and the average bulk velocity $\hat{u}_{\mathrm{av}}$ of turbulent flow in a channel of width $2L$ [72, p.278],

$$\frac{1}{\kappa} + \frac{\hat{u}_{\mathrm{av}}}{\hat{u}_\tau} = \frac{1}{\kappa}\ln\left(\frac{L\rho\hat{u}_\tau}{\mu}\right) + 5.9, \tag{2.28}$$

where $\kappa = 0.41$ is the von Karman constant. A dimensionless form of (2.28),

$$\frac{1}{\kappa} + u_{\mathrm{av}}\sqrt{\frac{Re_p}{\delta}} = \frac{1}{\kappa}\ln\sqrt{\delta^3 Re_p} + 5.9, \tag{2.29}$$

expresses the the Darcy velocity q in terms of the average bulk velocity $\hat{u}_{\mathrm{av}}$ through the dependence $Re_p(q)$ in (4.5). Substituting (2.29) into (2.27) yields

$$\frac{1}{\kappa} + \sqrt{\frac{Re_p}{\delta}}\left(1 + \frac{1}{2\delta}\right)u_{\mathrm{b}} = \frac{1}{\kappa}\ln\sqrt{\delta^3 Re_p} + A\sqrt{\frac{Re_p}{\delta}} + 5.9, \tag{2.30a}$$

where

$$A = \frac{1}{2\delta\lambda^2 M}\left[1 + (\coth\lambda - \operatorname{csch}\lambda)\left(\delta\tanh\lambda - \frac{1}{\lambda} - \frac{1}{\lambda}\operatorname{sech}\lambda\right)\right].$$ (2.30b)

Equation (2.30) allows one to determine the Darcy velocity q from measurements of the average bulk velocity $\hat{u}_\mathrm{b}$.

2.5.2 Estimation of CNT's flexural rigidity & comparison with experimental data

Data sets collected by [1] consist of measurement pairs $(\hat{u}_\mathrm{b}, \hat{X})$. The relevant parameters used in these experiments are presented in Table 2.1. We use measurements of average bulk velocity $\hat{u}_\mathrm{b}$ to determine the scaling factor (Darcy velocity) q from (2.30), and measurements of the deflection of a CNT's tip $\hat{X}$ to estimate the flexural rigidity $\hat{E}\hat{I}$ of CNTs from (2.24) and (2.14),

$$\hat{E}\hat{I} = \frac{\mu q H^4}{2\hat{X}}\left[2I_4(0) + \frac{B}{3}\right].$$ (2.31)

Equation (2.31) provides a closed-form expression to estimate the flexural rigidity of carbon nanotubes from their elastic response to hydrodynamic loading. We used (2.31) to determine $\hat{E}\hat{I}_\mathrm{av}$ for each sample, with the average flexural rigidity among all samples equal to $2.68 \cdot 10^{-22}$ Nm^2.

Table 2.1: Parameter values used in the experiment of [1] and corresponding dimensionless quantities.

Parameters	Units	Dimensionless parameters
$R_1 = 0.08$	μm	$\phi = 0.9735$
$R_0 = 0.02$	μm	$Da = 3.94 - 8.86 \cdot 10^{-7}$
$H = 40 - 60$	μm	$\delta = 24.83 - 37.75$
$L = 1.5$	mm	M $= 1$
$K = 1.4 \cdot 10^{-3}$	μm^2	$\epsilon = 1.3 - 2 \cdot 10^{-3}$
$\rho_\mathrm{air} = 1.2$	kg/m^3	
$\rho_\mathrm{Ar} = 1.784$	kg/m^3	
$\nu_\mathrm{air} = 1.5 \cdot 10^{-5}$	m^2/s	
$\nu_\mathrm{Ar} = 1.18 \cdot 10^{-5}$	m^2/s	
$\mu_\mathrm{air} = 1.8 \cdot 10^{-5}$	kg/m/s	
$\mu_\mathrm{Ar} = 2.1 \cdot 10^{-5}$	kg/m/s	
$\hat{u}_\mathrm{b} = 5 - 55$	m/s	

Alternatively, for a known value of $\hat{E}\hat{I}$, (2.31) can be used to predict the CNT tip deflections due to hydrodynamic loading of CNTs caused by different fluids and/or various values of average bulk velocity $\hat{u}_b$. Such predictions serve to validate our model through comparison with the experiments of [1]. Fig. 2.9 and 2.10 present experimental data and model predictions based on (2.31) wherein the average value of the CNT flexural rigidity, $\hat{E}\hat{I}_{av} = 2.99 \cdot 10^{-22}$ Nm^2, is computed from experiments with argon (Fig. 2.9) and then used to predict CNT deflections for air flow (Fig. 2.10). The figure reveals good agreement between theory and experiment over a wide range of flow velocities. Similarly good agreement was observed for other CNT heights (Fig. 2.11-2.12). For large velocities ($\hat{u}_b \geq 45$ m/s), the assumptions of elastic bending and constant permeability of a CNT forest may be violated because CNTs can overlap and develop kinks.
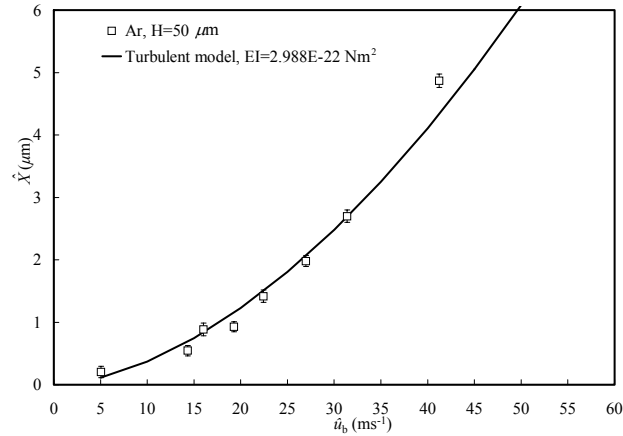
Figure 2.9: Experimental (squares) and predicted (solid lines) deflections of the CNT tip $\hat{X}$ in response to hydrodynamic loading by the turbulent flows of argon for a range of the bulk velocity values $\hat{u}_b$. The data from [1] are for CNTs of height $\hat{H} = 50\mu$m.

A typical wall thickness of CNTs with diameter $2R_0 = 40$nm is 0.34nm [75, 31, p. 33], which corresponds to the second moment of inertia $I \approx 8.3 \cdot 10^{-33}$ m^4. Hence our estimates of the flexural rigidity EI predict the Young modulus of individual CNTs to be $E \approx 0.034$TPa, which is of the same order of magnitude as $E \approx 0.09$TPa reported in [76, Fig. 3A] for single CNTs of comparable diameters. The factor of 3 discrepancy between the Young moduli of a single CNT and assembled CNTs is to be expected. Indeed, the
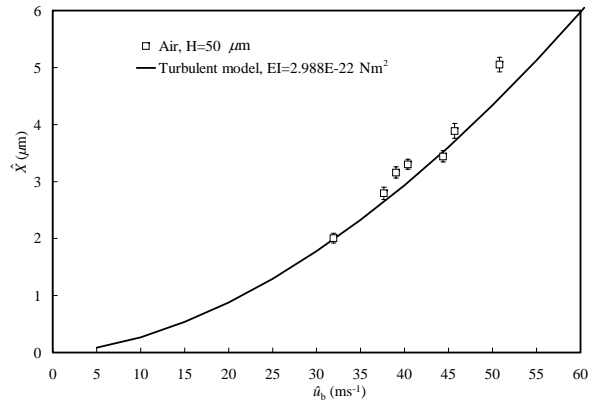
Figure 2.10: Experimental (squares) and predicted (solid lines) deflections of the CNT tip $\hat{X}$ in response to hydrodynamic loading by the turbulent flows of air for a range of the bulk velocity values $\hat{u}_b$. The data from [1] are for CNTs of height $\hat{H} = 50\mu$m.

latter often exhibit moduli that are more than an order of magnitude lower than the intrinsic moduli of individual nanotubes [77, 78]. This phenomenon has been attributed to growth techniques where impurities coat the surface of nanotubes and to the formation of bundles of parallel tubes, which reduce the effective surface area available for shear transfer [79, and references therein].

2.6 Summary and conclusions

The present research sheds new light on CNT-fluid flow interactions by going beyond phenomenological approaches, which fit data from physical experiments [1] and/or molecular dynamics simulations [4] to the Stokes solution for flow past a single infinite cylinder. Unlike these and other similar analyses, e.g. [68], our model accounts for the effects of both crowding in CNT forests and finite length of nanostructures. This is accomplished by treating CNT forests as a porous medium and deriving approximate analytical solutions for a coupled system of the Navier-Stokes and Brinkman equations, which describe flow over and through CNT forests, respectively.

We provide closed-form expressions for the drag force exerted on individual CNTs
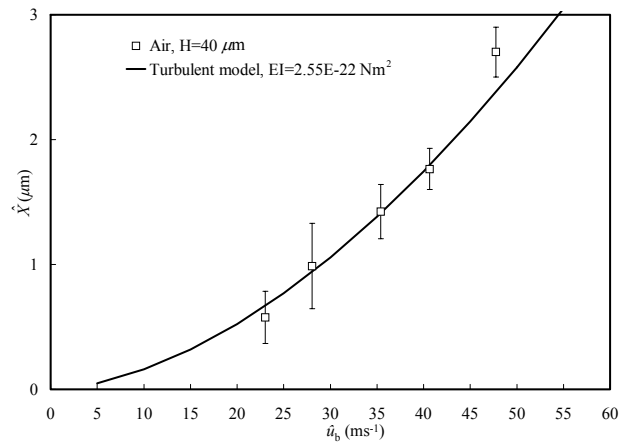
Figure 2.11: Experimental (squares) and predicted (solid lines) deflections of the CNT tip $\hat{X}$ in response to hydrodynamic loading by the turbulent flows of air for a range of the bulk velocity values $\hat{u}_b$. The data from [1] are for CNTs of height $\hat{H} = 40\mu$m.
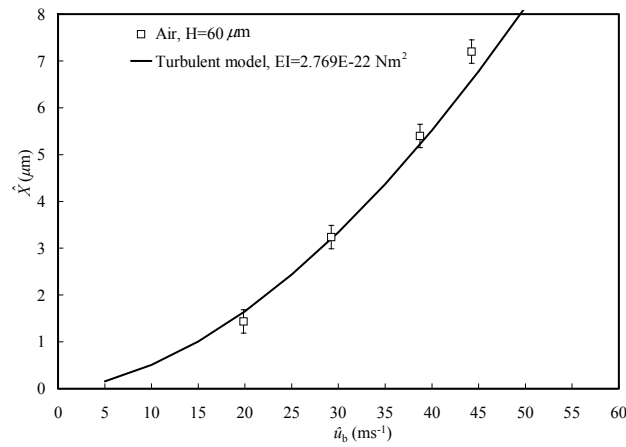
Figure 2.12: Experimental (squares) and predicted (solid lines) deflections of the CNT tip $\hat{X}$ in response to hydrodynamic loading by the turbulent flows of air for a range of the bulk velocity values $\hat{u}_b$. The data from [1] are for CNTs of height $\hat{H} = 60\mu$m.

and the corresponding drag coefficient C_D. To the best of our knowledge, this is the first rigorously derived expression for C_D, which takes into account the compound effects of both crowding in CNT forests and their finite height. Finally, we determine analytically the bending profile of individual CNTs caused by hydrodynamic loading. The maximum deflection at their tips can serve to estimate the flexural rigidity of CNTs. We demonstrated good agreement between our model predictions and experimental data.

Battiato, I., Bandaru, P. R., Tartakovsky, D. M., (2010) 'Elastic Response of Carbon Nanotube Forests to Aerodynamic Stresses'. Physical Review Letters. In press.

Chapter 3

Applicability Range of
Macroscopic Equations:
Diffusive-Reactive Systems

3.1   Introduction

In this Chapter we use the method of volume averaging [8] to identify compu-
tational sub-domains where the breakdown of standard continuum models occurs and,
hence, a pore-scale component of hybrid simulations is to be employed. The method of
volume averaging is employed to identify transport regimes for which the assumptions
required for the validity of upscaled (macroscopic) equations do not hold, and pore-scale
simulations are used to validate this theoretical analysis. To focus on the relative effects
of nonlinear geochemical reactions and diffusion, we neglect advection. In the following
Chapter, we will consider the effects of advection and employ upscaling approaches other
than the method of volume averaging.

In section 3.2, we formulate a pore-scale model of mixing-induced precipitation in
porous media, which consists of a system of coupled reaction-diffusion equations (RDEs);
specify key physical and (bio-)chemical assumptions that underpin this model; and iden-
tify Damköhler numbers for homogeneous and heterogeneous reaction as dimensionless
parameters that control the phenomenon. In section 3.3, we use the local volume aver-

aging [8] to derive a system of upscaled RDEs that are commonly used to model mixing-induced precipitation on the continuum scale, e.g., [43, and the references therein]. The goal here is to identify sufficient conditions for the macroscopic RDEs to be a valid descriptor of mixing-induced precipitation. Section 3.4 presents the results of pore-scale simulations of mixing-induced precipitation, which unambiguously show that these conditions are not met.

3.2 Problem formulation

Consider a porous medium Ω that is fully saturated with an incompressible liquid at rest. The medium consists of a solid matrix Ω_s and a liquid-occupied pore space Ω_l, so that $\Omega = \Omega_s \cup \Omega_l$. The liquid is a solution of two chemical (or biological) species M_1 and M_2 (with respective concentrations $\hat{c}_1$ and $\hat{c}_2$) that react to form an aqueous reaction product M_3. Whenever $\hat{c}_3$, the concentration of M_3, exceeds a threshold value, M_3 undergoes a heterogeneous reaction and precipitates on the solid matrix, forming a precipitate $M_{4(s)}$. In general, this process of mixing-induced precipitation is fully reversible, $M_1 + M_2 \rightleftarrows M_3 \rightleftarrows M_{4(s)}$, and its speed is controlled by the reaction rates k_{12} $[L^3 mol^{-1}T^{-1}]$, k_p $[LT^{-1}]$, k_3 $[T^{-1}]$ and k_d $[mol T^{-1}L^{-2}]$ corresponding to the following reactions,

$$M_1 + M_2 \xrightarrow{k_{12}} M_3 \xrightarrow{k_p} M_{4(s)} \quad \text{and} \quad M_1 + M_2 \xleftarrow{k_3} M_3 \xleftarrow{k_d} M_{4(s)}. \tag{3.1}$$
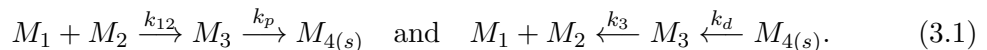
For bimolecular and unimolecular elementary reactions at constant temperature, the change in concentration is proportional to the product of the concentration of the reactants. Hence, the consumption and production rates, R_i^c with $i \in \{1, 2\}$ and R_3^p, of species M_i, $i \in \{1, 2\}$, and M_3, respectively, associated with the homogeneous reaction in (3.1) are typically concentration-driven and of the form $R_i^c = -R_3^p = -k_{12}\hat{c}_1\hat{c}_2 + k_3\hat{c}_3$. For the heterogeneous reaction, it is common to assume ([80, 81], and references therein) that i) precipitation rate r_p is proportional to concentration $\hat{c}_3$, i.e., $r_p = k_p\hat{c}_3$; ii) dissolution rate r_d is constant, $r_d = k_d$; and iii) super-saturation index does not become large enough to support precipitation in the liquid phase, i.e., precipitation of M_3 occurs solely as an overgrowth on solid grains.

With these assumptions, the aqueous concentrations $\hat{c}_i(\hat{\mathbf{r}}, \hat{t})$ $\left[molL^{-3}\right]$ at point $\hat{\mathbf{r}}$ and time $\hat{t}$ satisfy a system of reaction-diffusion equations (RDEs),

$$\frac{\partial \hat{c}_i}{\partial \hat{t}} = \mathscr{D}_i \hat{\nabla}^2 \hat{c}_i - k_{12} \hat{c}_1 \hat{c}_2 + k_3 \hat{c}_3 \quad \text{for} \quad \hat{\mathbf{r}} \in \Omega_l, \hat{t} > 0 \quad i = 1, 2 \qquad (3.2a)$$

$$\frac{\partial \hat{c}_3}{\partial \hat{t}} = \mathscr{D}_3 \hat{\nabla}^2 \hat{c}_3 + k_{12} \hat{c}_1 \hat{c}_2 - k_3 \hat{c}_3 \quad \text{for} \quad \hat{\mathbf{r}} \in \Omega_l, \hat{t} > 0, \qquad (3.2b)$$

subject to the boundary conditions on the (multi-connected) liquid-solid interface $\mathscr{A}_{ls}$

$$\mathbf{n} \cdot \hat{\nabla} \hat{c}_i = 0, \quad i = 1, 2; \qquad -\mathscr{D}_3 \mathbf{n} \cdot \hat{\nabla} \hat{c}_3 = k_p(\hat{c}_3 - c_{\text{eq}}) \qquad (3.3)$$

and the initial conditions

$$\hat{c}_i(\mathbf{x}, 0) = c_{i0}(\mathbf{x}), \quad i = 1, 2, 3, \qquad \Omega_l(0) = \Omega_{l0}, \qquad (3.4)$$

when concentration of $M_{4(s)}$ is strictly positive. Here the hatted quantities have appropriate units (physical dimensions), $c_{\text{eq}} = k_d/k_p$ is the equilibrium concentration, $\mathscr{D}_i$ $\left[L^2 T^{-1}\right]$ $(i = 1, 2, 3)$ are the diffusion coefficients of the aqueous species M_1, M_2, and M_3, respectively. Due to precipitation and dissolution, the liquid-solid interface $\mathscr{A}_{ls}(\hat{t})$, with the outward normal unit vector $\mathbf{n}(\hat{t})$, evolves in time $\hat{t}$ with velocity $\mathbf{v}$ $\left[LT^{-1}\right]$, according to $\rho_c \mathbf{v} \cdot \mathbf{n} = k_p(\hat{c}_3 - c_{\text{eq}})$, where ρ_c $\left[mol_s L^{-3}\right]$ is the molar density of the precipitate. The dynamics of the interface $\mathscr{A}_{ls}(\hat{t})$, result from a modeling assumption about the dependence of $\mathbf{v}$ on precipitation/dissolution rates and mass conservation [35].

Under certain assumptions, the system of RDEs (3.2) can be simplified by neglecting intermediate reactions [82, 43, 42, and the references therein]. In particular, if in (3.2b) reactions are faster than diffusion, and the diffusive term dominates the time-evolution term, then (3.2b) yields $c_3 \approx k_{12}/k_3 c_1 c_2$. Under these assumptions, the system (3.2)-(3.3) reduces to a system of two equations for $\hat{c}_i$ $(i = 1, 2)$: $\partial \hat{c}_i/\partial \hat{t} = \mathscr{D}_i \hat{\nabla}^2 \hat{c}_i$ subject to the interfacial conditions $\mathbf{n} \cdot \hat{\nabla} \hat{c}_i = 0$ and $\rho_c \mathbf{v} \cdot \mathbf{n} = k_c(\hat{c}_1 \hat{c}_2/k_{sp} - 1)$, where $k_c = k_p c_{\text{eq}}$ and $k_{sp} = k_3 c_{\text{eq}}/k_{12}$ is the solubility product. Calcite precipitation from calcium bicarbonate in water saturated with carbon dioxide, which follows the reaction path $Ca^{2+} + 2HCO_3^- \leftrightarrow Ca(HCO_3)_{2(l)} \leftrightarrow CaCO_{3(s)} + CO_{2(g)} + H_2O$, provides an example of geochemical systems for which these assumptions are not valid [83, 84]. For the sake of generality, we consider a more comprehensive system (3.2).

To be specific, we consider a scenario in which two identical solvents (e.g., water), one containing M_1 with concentration $\hat{c}_{10}$ and the other containing M_2 with concentration $\hat{c}_{20}$, are brought in contact with each other at time $\hat{t} = 0$. Since reactants M_1 and M_2 are initially separated, no reactions took place and the initial concentration of reaction product M_3 is $\hat{c}_{30} = 0$. This is a typical situation, corresponding, for example, to injection of a solution of M_1 into a porous medium occupied by a solution of M_2 [42].

The characteristic time scales associated with the chemical reactions (3.1) are $\tau_1 = \tau_2 = 1/k_{12}c_{10}$ for concentrations $\hat{c}_1$ and $\hat{c}_2$, and $\tau_3 = c_{\text{eq}}/k_{12}c_{10}^2$ for concentration $\hat{c}_3$. To simplify the presentation, we assume that the diffusion coefficients for reactants M_1 and M_2 and product $M_{3(l)}$ are the same, $\mathscr{D}_1 = \mathscr{D}_2 = \mathscr{D}_3 = \mathscr{D}$. Let us introduce dimensionless quantities

$$t = \frac{\hat{t}}{\tau}, \quad q = \frac{c_{\text{eq}}}{c_{10}}, \quad c_i = \frac{\hat{c}_i}{c_{10}}, \quad c_3 = \frac{\hat{c}_3}{c_{\text{eq}}}, \quad K = \frac{k_3 c_{eq}}{k_{12}c_{10}^2}, \quad \text{Da} = \frac{l^2 k_{12}c_{10}}{\mathscr{D}}, \quad (3.5)$$

where $i = 1, 2$; l denotes a characteristic length scale associated with pore structure; and Damköhler number Da is the ratio of diffusion and reaction time scales for species M_i (i=1,2,3). RDEs (3.2) can now be written in a dimensionless form as

$$\frac{\partial c_i}{\partial t} = \frac{l^2}{\text{Da}}\hat{\nabla}^2 c_i - c_1 c_2 + K c_3 \quad (i = 1, 2), \qquad q\frac{\partial c_3}{\partial t} = \frac{ql^2}{\text{Da}}\hat{\nabla}^2 c_3 + c_1 c_2 - K c_3. \quad (3.6)$$

Following [3], we define a Damköhler number for the precipitation/dissolution process as

$$\text{Da}_{ls} = \frac{k_p l}{\mathscr{D}}. \quad (3.7)$$

This yields a dimensionless form of the boundary conditions on the liquid-solid interface $\mathscr{A}_{ls}$,

$$\mathbf{n} \cdot \hat{\nabla} c_i = 0 \ (i = 1, 2), \quad \mathbf{n} \cdot l\hat{\nabla} c_3 = \text{Da}_{ls}(1 - c_3). \quad (3.8)$$

3.3 Macroscopic description of mixing-controlled heterogenous reactions

We proceed by employing the local volume averaging [8] to upscale the pore-scale equations (3.6) and (3.8) to the macroscopic scale. Section 3.3.1 contains definitions

of the averaging procedure. The derivation of upscaled equations is presented in Section 3.3.2. The results are summarized in Section 3.3.3, which presents a phase diagram identifying sufficient conditions under which the upscaled (macroscopic) description is valid.

3.3.1 Preliminaries

Consider a volume of the porous medium $\mathscr{V} \in \Omega$ whose volume is $|\mathscr{V}|$ and characteristic radius $r_0 \gg l$, where l is the pore-geometry length scale. Let $B(\hat{\mathbf{x}}) \in \mathscr{V}$ denote the volume of the liquid phase contained in $\mathscr{V}$, which is centered at $\hat{\mathbf{x}} \in \Omega$. If a characteristic length-scale of the macroscopic domain Ω is L, then the size of the averaging volume $\mathscr{V}$ is selected to satisfy $l \ll r_0 \ll L$.

Following [8], we define *superficial* and *intrinsic* averages of a quantity $c(\hat{\mathbf{r}})$ with $\hat{\mathbf{r}} \in \Omega_l$ as

$$\langle c \rangle(\hat{\mathbf{x}}) = \frac{1}{|\mathscr{V}|} \int_{B(\hat{\mathbf{x}})} c(\hat{\mathbf{r}}) \mathrm{d}^3 r \quad \text{and} \quad \langle c \rangle_B(\hat{\mathbf{x}}) = \frac{1}{|B(\hat{\mathbf{x}})|} \int_{B(\hat{\mathbf{x}})} c(\hat{\mathbf{r}}) \mathrm{d}^3 r, \tag{3.9}$$

respectively. The two averages are related through porosity $\phi \equiv |B|/|\mathscr{V}|$ by $\langle c \rangle = \phi \langle c \rangle_B$. The application of spatial averaging is facilitated by the spatial averaging theorem [8],

$$\langle \hat{\nabla} c \rangle = \hat{\nabla} \langle c \rangle + \frac{1}{|\mathscr{V}|} \int_{A_{ls}} c \mathbf{n} \mathrm{d}A, \tag{3.10}$$

where $A_{ls}(\hat{\mathbf{x}}) = \mathscr{V} \cap B(\hat{\mathbf{x}})$ is the liquid-solid interface contained in $\mathscr{V}$.

Let L_c, L_{c1} and L_ϕ denote characteristic length-scales associated with the macroscopic quantities $\langle c \rangle_B$, $\hat{\nabla} \langle c \rangle_B$ and ϕ, respectively. These scales are defined by [8, p.19]

$$\hat{\nabla} f_i(x) = \mathcal{O}\left(\frac{\Delta f_i}{L_i}\right), \qquad \Delta f_i(x) \equiv f_i\left(x + \frac{L_i}{2}\right) - f_i\left(x - \frac{L_i}{2}\right) \tag{3.11}$$

for $f_i = \{\langle c \rangle_B, \hat{\nabla} \langle c \rangle_B, \phi\}$ and $L_i = \{L_c, L_{c1}, L_\phi\}$, respectively. The notation

$$f = \mathcal{O}(g) \tag{3.12}$$

denotes an order of magnitude estimate in the following sense [85, p. 391]:

$$\frac{|g|}{\sqrt{10}} \leq |f| \leq |g|\sqrt{10}. \tag{3.13}$$

3.3.2 Upscaling via Volume Averaging

In this section, we upscale the third equation in (3.6). The remaining two equations in (3.6) are upscaled in a similar fashion.

We assume that reactions in the fluid phase are much faster than precipitation on the solid phase, so that $\langle \partial c_3/\partial t \rangle = \partial \langle c_3 \rangle/\partial t$. No assumptions are required for the upscaling of the linear term $\langle Kc_3 \rangle_B = K \langle c_3 \rangle_B$. The averaging procedure is presented below as a series of propositions. Their proofs are provided in Appendix A.

Proposition 3.3.1. *Suppose that the following scale constraints hold:*

1) $l \ll r_0$,

2) $r_0^2 \ll \overline{L}^2$ where $\overline{L} = min\{L_{c1}, L_\phi\}$,

3) $\epsilon \ll 1$ where $\epsilon = l/L_c$,

4) $r_0 \ll L_c$,

5) $r_0^2 \ll L_c L_{c1}$.

Then the average of the Laplacian in (3.6) can be approximated by

$$\langle \hat{\nabla}^2 c_3 \rangle = \phi \hat{\nabla}^2 \langle c_3 \rangle_B + \hat{\nabla}\phi \cdot \hat{\nabla} \langle c_3 \rangle_B + \frac{1}{|\mathcal{V}|} \hat{\nabla} \cdot \int_{A_{ls}} \tilde{c}_3 \mathbf{n}_{ls} \mathrm{d}A - a_v \, \mathrm{Da}_{ls} \frac{\langle c_3 \rangle_B - 1}{l} \quad (3.14)$$

where $a_v \equiv |\mathscr{A}_{ls}|/|\mathcal{V}|$ and $\tilde{c}_3$ is such that $c_3 = \langle c_3 \rangle_B + \tilde{c}_3$.

The scale constraints of Proposition 3.3.1 are routinely used in the method of volume averaging and other upscaling techniques to define the size of an averaging volume $\mathcal{V}$, which might or might not constitute a representative elementary volume (REV). Constraints 1 and 4 require $\mathcal{V}$ to be large enough to smooth out (average) pore-scale fluctuations of relevant variables (e.g., concentration) and small enough to capture their macro-scale variability, respectively. The remaining constraints guarantee that the average concentration at the centroid of $\mathcal{V}$ provides an adequate representation of the pore-scale concentration distribution at all points inside $\mathcal{V}$ [8].

Proposition 3.3.2. *Suppose that the scale constraints 3)–5) of the Proposition 3.3.1 hold. Then the average of the reaction term in (3.6) can be approximated by*

$$\langle c_1 c_2 \rangle = \phi \langle c_1 \rangle_B \langle c_2 \rangle_B . \quad (3.15)$$

While the approximation (3.15) can be improved upon, its importance for the present analysis stems from the observation that it does not introduce additional scale constraints.

Proposition 3.3.3. *Suppose that in addition to the constraints in Proposition 3.3.1 the following scale constraints hold:*

1) $a_v \approx l^{-1}$,

2) $t \gg \mathrm{Da}$,

3) $l \ll L_\phi$.

Then, the concentration fluctuations $\tilde{c}_3$ satisfy a differential equation

$$0 = \frac{ql^2}{\mathrm{Da}}\hat{\nabla}^2\tilde{c}_3 + \frac{qa_v l}{\phi}\frac{\mathrm{Da}_{ls}}{\mathrm{Da}}(\langle c_3\rangle_B - 1) + \tilde{c}_1\langle c_2\rangle_B + \tilde{c}_2\langle c_1\rangle_B + \tilde{c}_1\tilde{c}_2 - K\tilde{c}_3 \qquad (3.16)$$

subject to the boundary conditions

$$-\mathbf{n}\cdot\hat{\nabla}\tilde{c}_3 = \mathbf{n}\cdot\hat{\nabla}\langle c_3\rangle_B + \mathrm{Da}_{ls}\frac{\langle c_3\rangle_B + \tilde{c}_3 - 1}{l}. \qquad (3.17)$$

The scale constraint 1) corresponds to representations of solid grains by spheres, in which case specific surface a_v, surface A_{ls}, and volume B scale as l^{-1}, l^2 and l^3, respectively. The constraint 3) ensures that porosity changes smoothly enough for its gradient to be negligible.

Boundary-value problems for fluctuations $\tilde{c}_1$ and $\tilde{c}_2$ are derived in a similar manner. Further progress requires an assumption of periodicity of the porous medium.

Proposition 3.3.4. *Suppose that in addition to the scale constraints imposed by Propositions 3.3.1 and 3.3.3 the porous medium is periodic with a unit cell characterized by $\mathbf{n}(\hat{\mathbf{r}} + \hat{\mathbf{l}}_i) = \mathbf{n}(\hat{\mathbf{r}})$, where $\hat{\mathbf{l}}_i$ with $i = 1, 2, 3$ represents the three lattice vectors describing a spatially periodic porous medium. Then concentration fluctuations are periodic, $\tilde{c}(\hat{\mathbf{r}} + \hat{\mathbf{l}}_i) = \tilde{c}(\hat{\mathbf{r}})$, and $\langle c_3\rangle_B$ and $\hat{\nabla}\langle c_3\rangle_B$ in (3.16) and (3.17) are evaluated at the centroid.*

Mathematical representations of natural porous media as a periodic collection of unit cells might appear to be overly restrictive. However, this assumption often leads to homogenezation results (effective or continuum models) that are applicable to other

realistic heterogeneous environments. A detailed discussion of the practical utility of periodic conceptualizations of the pore-structure of porous media can be found in section 2 of [86].

Proposition 3.3.5. *Suppose that in addition to the constraint imposed by Proposition 3.3.3 the following constraints hold:*

1) $\mathrm{Da}_{ls} \ll \epsilon$.

2) $\mathrm{Da} \ll 1$,

Then concentration fluctuations $\tilde{c}_3$ can be represented in terms of the macroscopic variables as

$$\tilde{c}_3 = \hat{\mathbf{b}} \cdot \hat{\nabla} \langle c_3 \rangle_B + s \langle c_3 \rangle_B + \psi, \tag{3.18}$$

where the closure variables $\hat{\mathbf{b}}$, s and ψ are solutions of the boundary value problems (wherein $j = 1, 2, 3$)

$$\hat{\nabla}^2 \hat{\mathbf{b}} - \frac{k_3}{\mathscr{D}} \hat{\mathbf{b}} = \mathbf{0}, \qquad -\mathbf{n} \cdot \hat{\nabla} \hat{\mathbf{b}} = \mathbf{n} \quad at \quad A_{ls}, \qquad \hat{\mathbf{b}}(\hat{\mathbf{r}} + \hat{\mathbf{l}}_j) = \hat{\mathbf{b}}(\hat{\mathbf{r}}); \tag{3.19}$$

$$\hat{\nabla}^2 s - \frac{k_3}{\mathscr{D}} s = -\frac{a_v \mathrm{Da}_{ls}}{\phi l}, \qquad -\mathbf{n} \cdot \hat{\nabla} s = \frac{\mathrm{Da}_{ls}}{l} \langle c_3 \rangle^l \quad at \quad A_{ls}, \qquad s(\hat{\mathbf{r}} + \hat{\mathbf{l}}_j) = s(\hat{\mathbf{r}}); \tag{3.20}$$

$$\hat{\nabla}^2 \psi - \frac{k_3}{\mathscr{D}} \psi = \frac{a_v \mathrm{Da}_{ls}}{\phi l}, \qquad -\mathbf{n} \cdot \hat{\nabla} \psi = -\frac{\mathrm{Da}_{ls}}{l} \quad at \quad A_{ls}, \qquad \psi(\hat{\mathbf{r}} + \hat{\mathbf{l}}_j) = \psi(\hat{\mathbf{r}}). \tag{3.21}$$

The conditions 1) and 2) ensure that the system is well mixed at the pore scale, as discussed in section 3.3.3 below.

Combining the results from Propositions 3.3.1–3.3.5 with analogous results for $\langle c_1 \rangle_B$ and $\langle c_2 \rangle_B$, the volume averaging of (3.6) leads to a system of macroscopic equations (see Appendix A.6)

$$\phi \frac{\partial \langle c_i \rangle_B}{\partial t} = \frac{\epsilon^2}{\mathrm{Da}} \nabla \cdot (\phi \mathbf{D}_{\mathrm{eff}} \cdot \nabla \langle c_i \rangle_B) - \phi \langle c_1 \rangle_B \langle c_2 \rangle_B + \phi K \langle c_3 \rangle_B \qquad (i = 1, 2), \tag{3.22}$$

$$\phi q \frac{\partial \langle c_3 \rangle_B}{\partial t} = \frac{q \epsilon^2}{\mathrm{Da}} \nabla \cdot (\phi \mathbf{D}_{\mathrm{eff}} \cdot \nabla \langle c_3 \rangle_B) - q a_v l \frac{\mathrm{Da}_{ls}}{\mathrm{Da}} [\langle c_3 \rangle_B - 1] + \phi \langle c_1 \rangle_B \langle c_2 \rangle_B - \phi K \langle c_3 \rangle_B, \tag{3.23}$$

where the effective diffusivity tensor $\mathbf{D}_{\mathrm{eff}}$ is defined as

$$\mathbf{D}_{\mathrm{eff}} = \mathbf{I} + \frac{1}{|B|} \int_{A_{ls}} \mathbf{n} \hat{\mathbf{b}} \mathrm{d}A. \tag{3.24}$$

3.3.3 Applicability of macroscopic models

According to Proposition 3.3.5, a sufficient condition for the validity of the macroscopic description (3.22)–(3.23) requires that Da ≪ 1, which implies that on the pore scale the system is well-mixed with diffusion dominating reactions. Further insight is gained by relating different macroscopic diffusion and/or reaction regimes to the Damköhler number Da expressed in terms of the scale-separation parameter ϵ. (This is conceptually similar to the analysis of macroscopic dispersion equations [19], which identifies distinct transport regimes by expressing the Péclet number as powers of ϵ.) Interplay between the Damköhler number and ϵ determines whether macroscopic RDEs (3.22) and (3.23) are diffusion or reaction dominated. For Da $< \epsilon^2$, the macroscopic process is diffusion-driven and the nonlinear effects introduced by reactions are negligible. The two mechanisms are of the same order of magnitude in the region $\epsilon^2 <$ Da $< \epsilon$, and reactions dominate diffusion if $\epsilon <$ Da < 1.
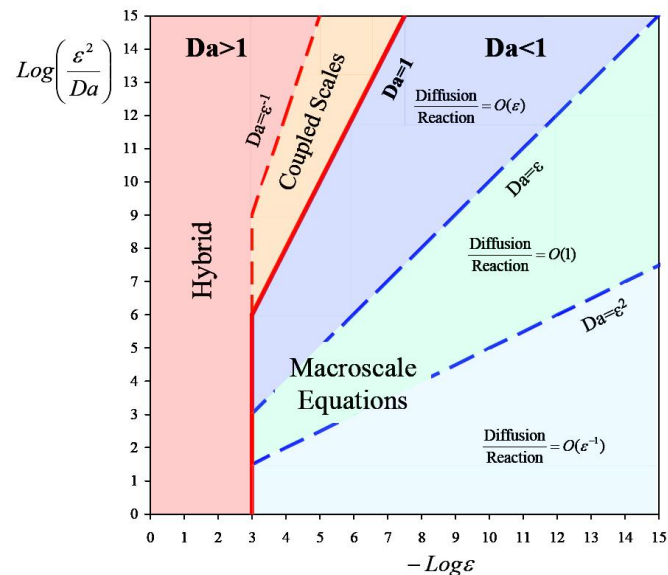
Figure 3.1: Phase diagram indicating the range of applicability of macroscopic equations for the reaction-diffusion system (3.6) in terms of Da. The blue regions identify the sufficient conditions under which the macroscopic equations hold. In the red and orange regions, macro- and micro-scale problems are coupled and have to be solved simultaneously.

Combining constraints 1 and 4 of Proposition 3.3.1 and 1 of Proposition 3.3.4, we can write $l \ll r_0 \ll \min\{L_c, L_{c1}\}$. As an example, let us assume that $L_c = \min\{L_c, L_{c1}\}$, where L_c is the typical length scale associated with the average concentration, as defined by (3.11). Recalling the operational definition of the order of magnitude $\mathcal{O}(\cdot)$ in (3.12)–(3.13) and the definition of ϵ in Proposition 3.3.1, we obtain a constraint $\epsilon \leq 10^{-3}$.

Figure 4.1 summarizes these constraints in the form of a phase diagram. The solid red line, which is composed of the straight lines $\mathrm{Da} = 1$, and $\epsilon = 10^{-3}$, separates the region where the macroscopic model (3.22)–(3.23) is valid (to the right of the red line) and the region where it is a priori not (to the left of the red line). The dashed blue lines $\mathrm{Da} = \epsilon^2$ and $\mathrm{Da} = \epsilon$ separate the diffusion-dominated, diffusion-reaction, and reaction-dominated regimes for (3.22)–(3.23). In the region $\epsilon^{-1} < \mathrm{Da} < 1$, a system of equations for pore-scale fluctuations [32] must be solved *simultaneously* with a macroscopic problem (see Appendix A.6). This region is labeled "Coupled Scales" in Fig. 4.1. Mixing-induced precipitation, which is characterized by $\mathrm{Da} \gg 1$, falls into the category of physical phenomena for which pore-scale or hybrid simulations are a priori necessary.

3.4 Comparison with Pore-Scale Simulations

In this section, we use pore-scale numerical simulations of (3.6) and (3.8) with $\mathrm{Da} > 1$ both to demonstrate that the constraints imposed by the averaging procedure outlined above are indeed not satisfied in the region "Hybrid" of the phase-diagram in Fig. 4.1 and to quantify various approximation errors. A computational example with $\mathrm{Da} = 4.4 \cdot 10^{-4}$, which represents the region in Fig. 4.1 where continuum models are expected to be valid, can be found in [6].

The RDEs (3.6) are defined for the pore space of a two-dimensional porous medium $[-L/2, L/2] \times [0, H]$, with $L = 32$ and $H = 8$. The porous medium is composed of circular grains with radius $l = 3$, which form periodically arranged unit cells, as shown in Figure 3.2. In addition to the boundary conditions (3.8), the RDEs (3.6) are subject to the exterior boundary conditions $\partial_x c_1(L/2, y, t) = 0$, $\partial_x c_2(-L/2, y, t) = 0$, $\partial_x c_3(\pm L/2, y, t) = 0$, $c_1(-L/2, y, t) = 1$, and $c_2(L/2, y, t) = 1$. The periodic boundary conditions are prescribed at $y = 0$ and $y = B$. The initial conditions are $c_1(-L/2 \leq$

$x \leq 0, y, 0) = 1$, $c_1(0 < x \leq L_2, y, 0) = 0$, $c_2(-L/2 \leq x < 0, y, 0) = 1$, and $c_2(0 \leq x \leq L_2, y, 0) = 0$.
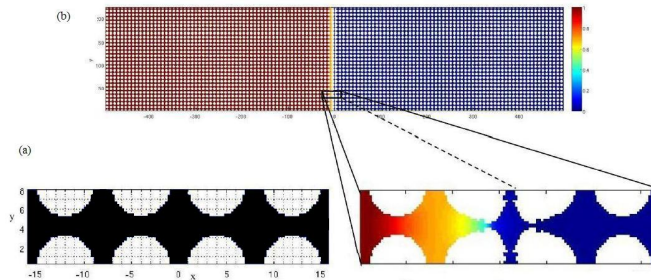
Figure 3.2: (a) Schematic representation of a unit cell of the porous medium at the pore scale. White spaces represent solid grains. (b) Concentration distribution for c_1 in the macroscopic domain, obtained by replicating the unit cell in the y-direction.

3.4.1 Numerical implementation

We used the mesh-free Smoothed Particle Hydrodynamics (SPH) simulations [3, 6] to solve this initial-boundary-value problem. SPH "particles" were placed on square lattices whose size is $\Delta x = \Delta y = 0.25$. Table 3.1 presents the parameter values used in our simulations. We consider $K \ll 1$ so that the backward homogeneous reaction can be neglected.

The macroscopic quantities, such as $\langle c_1 \rangle$, were computed from the pore-scale simulations by averaging over a volume $\mathscr{V}$ whose characteristic dimension is $r_0 \gg l$. Following [87], we define the size of the averaging volume, i.e., the value of r_0, as the minimum radius of $\mathscr{V}$ beyond which porosity ϕ remains constant as the averaging volume increases. For the geometric parameters used in our simulation, this yields $r_0 = 125$ which clearly satisfies the inequality $r_0 \gg l$. The intrinsic average $\langle c_1 \rangle_B$ in (3.9) was computed as

$$\langle c_1 \rangle_B (\mathbf{x}) \approx \frac{1}{N(\mathbf{x})} \sum_{b \in \mathscr{V}} c_1(\mathbf{y}_b) W_{\mathbf{x}, r_0}(\mathbf{y}_b), \tag{3.25}$$

where $N(\mathbf{x})$ is the number of liquid SPH "particles" contained in $\mathscr{V}(\mathbf{x})$, $\mathbf{y}_b$ is the position

of the "particle" b, and

$$W_{\mathbf{x},r_0}(\mathbf{y}) = \begin{cases} 1 & \text{if } |\mathbf{y} - \mathbf{x}| \leq r_0 \\ 0 & \text{if } |\mathbf{y} - \mathbf{x}| > r_0. \end{cases} \tag{3.26}$$

3.4.2 Simulation results

We start by investigating whether the mixing-induced precipitation described on the pore scale by the system of RDEs (3.6) lends itself to scale separation. It follows from (3.11) and (3.13) that

$$|\nabla\langle c_1\rangle_B| \leq \frac{|\Delta\langle c_1\rangle_B|}{L_c}\sqrt{10} \leq \frac{\sqrt{10}}{L_c}, \tag{3.27}$$

where the second inequality stems from the bound $|\Delta\langle c\rangle_B| \leq 1$, being $0 \leq \langle c\rangle_B \leq 1$. Using an operational definition of $\gg$ [88, p. 13], we express the constraint $L_c \gg r_0$, imposed by Proposition 3.3.1, in terms of an inequality $L_c \geq 10r_0$. Substituting this inequality into (3.27) gives an upper bound of the gradient of the average concentration,

$$|\nabla\langle c_1\rangle_B| \leq \frac{1}{\sqrt{10}r_0}, \tag{3.28}$$

which serves as a *necessary condition* for the scale separation to occur.
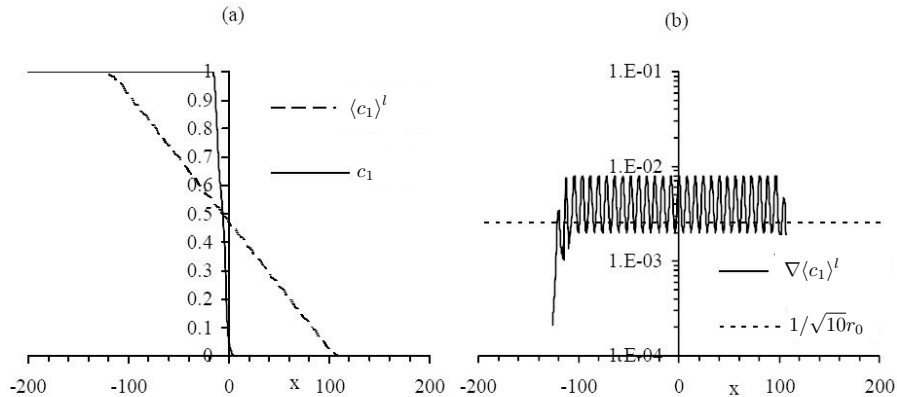
Figure 3.3: Horizontal cross-sections at $t = 15400$ of (a) pore-scale concentration c_1 and its intrinsic average $\langle c_1\rangle_B$, and (b) the horizontal component of the average concentration gradient $\nabla\langle c_1\rangle_B$.

Figure 3.3a exhibits profiles of $c_1(x)$ and $\langle c_1\rangle_B(x)$ along the cross-section $y = H/2+nH$, $n = \{0, 1, 2...\}$, which lies entirely in the fluid phase. Numerical differentiation

was further used to compute $\nabla\langle c_1\rangle_B$ along this cross-section. Small oscillations of the intrinsic average $\langle c_1\rangle_B(x)$ in Fig. 3.3a stem from its definition (3.9). As the averaging window of size $|\mathscr{V}|$ moves from left to right, the pore volume B varies periodically, giving rise to large periodic oscillation in $\nabla\langle c_1\rangle_B$ (Fig. 3.3b). One can see that the smoothed (average) gradient is $\nabla\langle c_1\rangle_B \approx \Delta\langle c_1\rangle_B/\Delta x \approx 1/200 = 0.005$, so that the bound (3.28) is not satisfied in the vicinity of the reacting front. This violates the constraint $L_c \gg r_0$, imposed by Proposition 3.3.1.

We now proceed to analyze how the lack of scale separation affects the accuracy of the closure approximation $\langle c_1 c_2\rangle_B \approx \langle c_1\rangle_B\langle c_2\rangle_B$, on which the macroscopic RDEs (3.22) and (3.23) are based. The proof of Proposition 3.3.2 in Appendix A.2 demonstrates that this closure requires one to neglect the terms $\langle\tilde{c}_1\tilde{c}_2\rangle_B$, $\langle\tilde{c}_1\langle c_2\rangle_B\rangle_B$ and $\langle\tilde{c}_2\langle c_1\rangle_B\rangle_B$, and to assume that $\langle\langle c_1\rangle_B\langle c_2\rangle_B\rangle_B \approx \langle c_1\rangle_B\langle c_2\rangle_B$. The results of our pore-scale simulations shown in Fig. 3.4 reveal that both $\langle\langle c_1\rangle_B\langle c_2\rangle_B\rangle_B$ and $\langle c_1\rangle_B\langle c_2\rangle_B$ significantly overestimate $\langle c_1 c_2\rangle_B$.
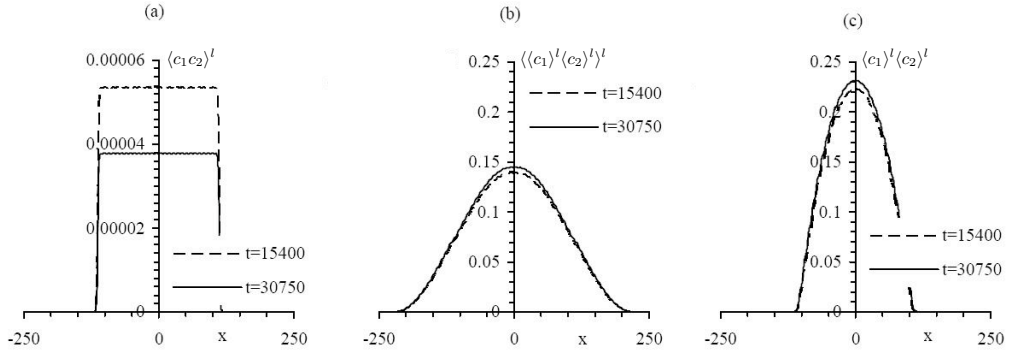
Figure 3.4: Horizontal cross-sections of (a) $\langle c_1 c_2\rangle_B$ and its approximations (b) $\langle\langle c_1\rangle_B\langle c_2\rangle_B\rangle_B$ and (c) $\langle c_1\rangle_B\langle c_2\rangle_B$.

This finding is further elaborated upon in Fig. 3.5, which depicts the relative errors in progressively improved approximations of the term $\langle c_1 c_2\rangle_B$,

$$E_i^\% = \frac{|E_i|}{\langle c_1 c_2\rangle_B} \qquad i = 1,\ldots,4, \tag{3.29}$$

where $E_1 = \langle c_1\rangle_B\langle c_2\rangle_B - \langle c_1 c_2\rangle_B$, $E_2 = E_1 + \langle\tilde{c}_1\tilde{c}_2\rangle_B$, $E_3 = E_2 + \langle\tilde{c}_1\langle c_2\rangle_B\rangle_B$, and $E_4 = E_3 + \langle\tilde{c}_2\langle c_1\rangle_B\rangle_B$. While the incorporation of more fluctuating terms slightly decreases the relative errors, they remain unacceptably high even when all the terms are included

$(E_4^\% \approx 10^3)$. This shows that $\langle\langle c_1\rangle_B\langle c_2\rangle_B\rangle_B \approx \langle c_1\rangle_B\langle c_2\rangle_B$ is the weakest approximation. (Recall that the definition of the intrinsic average $\langle\cdot\rangle_B$ in (3.9) implies that this indeed is only an approximation.) This finding is to be expected, since for $L_c = \mathcal{O}(l)$ a Taylor expansion around the centroid does not provide an accurate description of nonlocal terms.
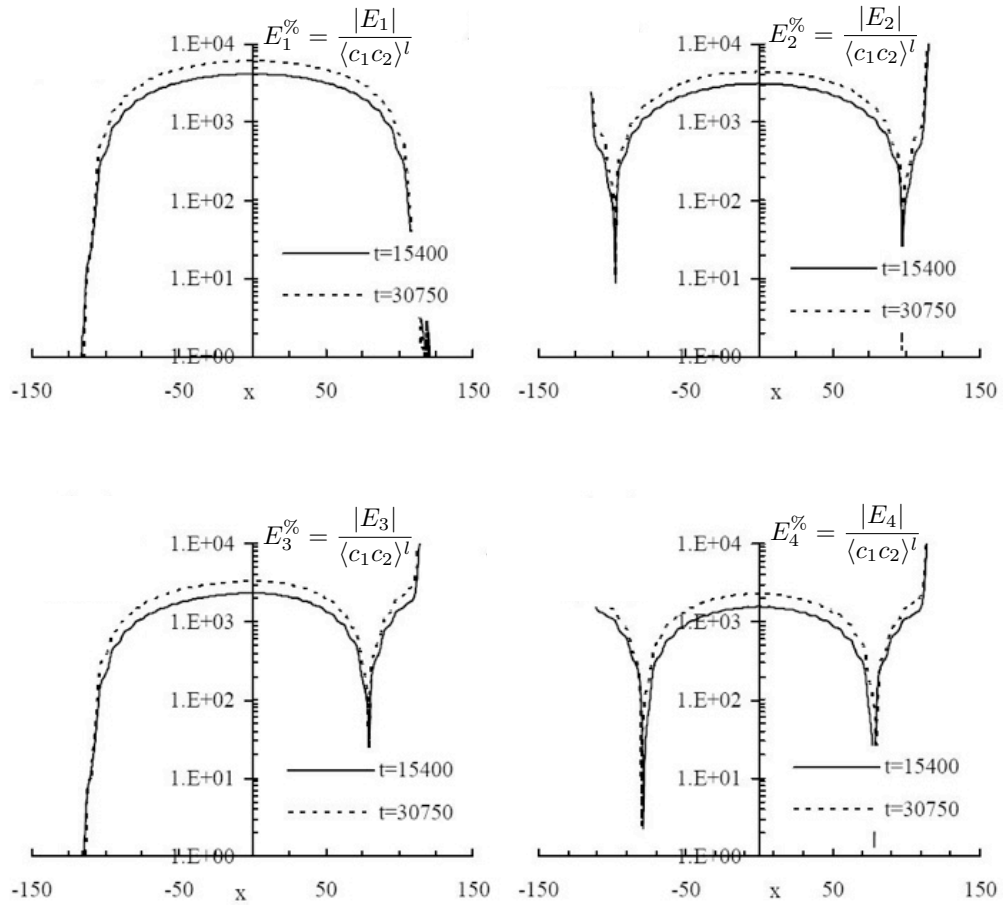
Figure 3.5: Relative errors $E_i^\%$ $(i = 1, \ldots, 4)$ in (3.29) introduced by various closure approximations.

3.5 Summary and conclusions

Reactive transport in fully saturated porous media is a complex nonlinear phenomenon that involves both homogeneous (bio-)chemical reactions between species dissolved in a fluid and heterogeneous reactions that occur on liquid-solid interfaces. We

Table 3.1: Parameter values (in model units) and corresponding dimensionless quantities used in pore-scale simulations.

Parameters	Units	Dimensionless parameters
$\mathscr{D} = 0.5$	$L^2 T^{-1}$	Da = 27
$k_{12} c_{10} = 1.5$	T^{-1}	$\text{Da}_{ls} = 120$
$k_p = 20$	$L T^{-1}$	$q = 0.3$
$c_{eq} = 0.15$	$\text{mol} L^{-2}$	
$c_{eq}/c_{10} = 0.3$	$-$	

considered processes that are dominated by two transport mechanisms, molecular diffusion and (bio-)chemical reactions, whose relative importance is quantified by the (dimensionless) Damköhler number Da. Specifically, we considered mixing-induced precipitation, in which two dissolved reactants produce a third species that, after reaching a threshold concentration value, precipitates on the solid matrix.

Our main goal was to establish sufficient conditions under which macroscopic reaction-diffusion equations (RDEs) provide an adequate averaged description of pore-scale processes, and to quantify predictive errors that occur when some or all of these conditions are violated. To accomplish this goal, we upscaled the pore-scale RDEs to the continuum (macroscopic) scale and used pore-scale numerical simulations to verify various upscaling assumptions. Our analysis leads to the following major conclusions.

1. The range of applicability of macroscopic RDEs and various transport regimes can be described with a phase diagram (Fig. 4.1) in the (Da, ϵ) space; and ϵ is the scale-separation parameter defined as the ratio of the characteristic lengths associated with pore-scale geometry and macroscopic concentrations of reacting species, respectively.

2. This phase diagram shows that highly localized phenomena in porous media, such as mixing-induced precipitation on (and/or dissolution of) a porous matrix, do not lend themselves to macroscopic (upscaled) descriptions. The use of macroscopic RDEs, such as (3.22) and (3.23), to describe such phenomena relies on a number of approximations whose accuracy cannot be ascertain a priori.

3. Validation of these approximations requires pore-scale simulations. Our simulations suggest that the largest error stems from the localization, $\langle \langle c_1 \rangle_B \langle c_2 \rangle_B \rangle_B \approx$

$\langle c_1 \rangle_B \langle c_2 \rangle_B$, of the product of macroscopic (averaged) concentrations $\langle c_i \rangle_B$ $(i = 1, 2)$ rather than from omission of the terms involving pore-scale fluctuations $\tilde{c}_i$. This suggests that a nonlocal (integro-differential) alternative of (3.22) and (3.23) might provide an accurate macroscopic approximation.

4. Hybrid pore-scale/continuum-scale simulations [2, 6] are a more rigorous (and more computationally intensive) alternative. The scale-separation constraint (3.28) can facilitate such simulations by identifying the regions in a continuum computational domain where average (continuum-scale) concentration gradients exceed the given bound.

In the next Chapter we will incorporate advection and dispersion into the analysis presented above and employ upscaling approaches other than the method of volume averaging to identify regions where continuum models break down.

Battiato, I., Tartakovsky, D. M., Tartakovsky, A. M., Scheibe T. D., (2009), 'On Breakdown of Macroscopic Models of Mixing-Controlled Heterogeneous Reactions in Porous Media'. Adv. Water Resour., doi:10.1016/j.advwatres.2009.08.008.

Chapter 4

Applicability Range of Macroscopic Equations: Advective-Diffusive-Reactive Systems

4.1   Introduction

In the present Chapter we investigate the conditions under which continuum descriptions of reactive transport, i.e., advection-dispersion-reaction equations (ARDEs), break down. In section 4.2, we formulate a pore-scale model of nonlinear crystal dissolution-precipitation, and identify the Damköhler and Péclet numbers as dimensionless parameters that control the phenomenon. In section 4.3, we employ a multiple-scale expansion [19, 16] to derive an effective ARDE and to specify sufficient conditions that guarantee its validity. The region of validity of this continuum description is represented by a phase diagram in the $(\mathrm{Da}, \mathrm{Pe})$ space. A number of special cases are discussed in section 4.4. The main results and conclusions are summarized in section 4.5.

4.2   Problem Formulation

Consider reactive transport in a porous medium $\hat{\Omega}$ whose characteristic length is L. Let us assume that the medium can be represented microscopically by a collection of spatially periodic "unit cells" $\hat{\mathscr{V}}$ with a characteristic length l, such that a scale parameter $\varepsilon \equiv l/L \ll 1$. Spatially periodic representations of micro-structures of porous media are routinely used to derive macroscopic properties and effective models of phenomena taking place in disordered media that lack such periodicity [86, Section 2]. The unit cell $\hat{\mathscr{V}} = \hat{B} \cup \hat{G}$ consists of the pore space $\hat{B}$ and the impermeable solid matrix $\hat{G}$ that are separated by the smooth surface $\hat{A}_{ls}$. The pore spaces $\hat{B}$ of each cell $\hat{\mathscr{V}}$ form a multi-connected pore-space domain $\hat{B}^{\varepsilon} \subset \hat{\Omega}$ bounded by the smooth surface $\hat{A}_{ls}^{\varepsilon}$.

4.2.1   Governing equations

Single-phase flow of an incompressible fluid in the pore-space $\hat{B}^{\varepsilon}$ is described by the Stokes and continuity equations subject to the no-slip boundary condition on $\hat{A}_{ls}^{\varepsilon}$,

$$\hat{\mu}\hat{\nabla}^2\hat{\mathbf{v}}_{\varepsilon} - \hat{\nabla}\hat{p} = 0, \quad \hat{\nabla} \cdot \hat{\mathbf{v}}_{\varepsilon} = 0, \quad \hat{\mathbf{x}} \in \hat{B}^{\varepsilon}, \qquad \hat{\mathbf{v}}_{\varepsilon} = \mathbf{0}, \quad \hat{\mathbf{x}} \in \hat{A}_{ls}^{\varepsilon}, \tag{4.1}$$

where $\hat{\mathbf{v}}_{\varepsilon}(\hat{\mathbf{x}})$ is the fluid velocity, $\hat{p}$ denotes the fluid dynamic pressure, and $\hat{\mu}$ is the dynamic viscosity. The fluid contains a dissolved species $\mathcal{M}$, whose molar concentration $\hat{c}_{\varepsilon}(\hat{\mathbf{x}}, \hat{t})$ $[molL^{-3}]$ at point $\hat{\mathbf{x}} \in \hat{B}^{\varepsilon}$ and time $\hat{t} > 0$ changes due to advection, molecular diffusion, and a nonlinear heterogeneous reaction at the solid-liquid interface $\hat{A}_{ls}^{\varepsilon}$. The first two phenomena are described by an advection-diffusion equation,

$$\frac{\partial \hat{c}_{\varepsilon}}{\partial \hat{t}} + \hat{\mathbf{v}}_{\varepsilon} \cdot \hat{\nabla}c_{\varepsilon} = \hat{\nabla} \cdot (\hat{\mathbf{D}}\hat{\nabla}\hat{c}_{\varepsilon}), \qquad \hat{\mathbf{x}} \in \hat{B}^{\varepsilon}, \quad \hat{t} > 0, \tag{4.2}$$

where the molecular diffusion coefficient $\hat{\mathbf{D}}$ is, in general, a positive-definite second-rank tensor. If diffusion is isotropic, $\hat{\mathbf{D}} = \hat{\mathscr{D}}_m\mathbf{I}$ where $\hat{\mathscr{D}}_m$ $[L^2T^{-1}]$ is the diffusion coefficient and $\mathbf{I}$ is the identity matrix.

Whenever the concentration $\hat{c}_{\varepsilon}$ exceeds a threshold value $\bar{c}$, a heterogeneous reaction $n\mathcal{M} \leftrightarrow \mathcal{N}_{(s)}$ occurs, in which n molecules of the solute $\mathcal{M}$ precipitate in the form of one molecule of a crystalline solid $\mathcal{N}_{(s)}$. At the solid-liquid interface $\hat{A}_{ls}^{\varepsilon}$ impermeable to flow, mass conservation requires that mass flux of the species $\mathcal{M}$ be balanced by the

difference between the precipitation rate R_p and the dissolution rate R_d,

$$-\mathbf{n} \cdot \hat{\mathbf{D}} \hat{\nabla} \hat{c}_\varepsilon = R_p - R_d, \tag{4.3}$$

where $\mathbf{n}$ is the outward unit normal vector of $\hat{A}^\varepsilon_{ls}$. Following [80], we assume that $R_p = \hat{k} \hat{c}^a_\varepsilon$ and $R_d = \hat{k} \bar{c}^a$, where $\hat{k}$ $[L^{3a-2} T^{-1} mol^{1-a}]$ is the reaction rate constant, $a \in \mathbb{Z}^+$ is related to the order of reaction n [89, Eq. 6], and the threshold concentration $\bar{c}$ represents the solubility product [89]. Mass conservation on the liquid-solid interface $\hat{A}^\varepsilon_{ls}$ yields a boundary condition [89, Eq. 5],

$$-\mathbf{n} \cdot \hat{\mathbf{D}} \hat{\nabla} \hat{c}_\varepsilon = \hat{k}(\hat{c}^a_\varepsilon - \bar{c}^a), \qquad \hat{\mathbf{x}} \in \hat{A}^\varepsilon_{ls}, \quad \hat{t} > 0. \tag{4.4}$$

In addition to (4.4), the flow and transport equations (5.1) and (4.2) are supplemented with proper boundary conditions on the external boundary of the flow domain $\hat{\Omega}$.

4.2.2 Dimensionless formulation

Let us introduce dimensionless quantities

$$c_\varepsilon = \frac{\hat{c}_\varepsilon}{\bar{c}}, \quad \mathbf{x} = \frac{\hat{\mathbf{x}}}{L}, \quad \mathbf{v}_\varepsilon = \frac{\hat{\mathbf{v}}_\varepsilon}{U}, \quad \mathbf{D} = \frac{\hat{\mathbf{D}}}{D}, \quad p = \frac{\hat{p} l^2}{\hat{\mu} U L}, \tag{4.5}$$

where D and U are characteristic values of $\mathbf{D}$ and $\mathbf{v}_\varepsilon$, respectively. The scaling of pressure $\hat{p}$ ensures that the pressure gradient and the viscous term are of the same order of magnitude, as prescribed by Stokes equation [19, Eqs. 15 and 16]. Furthermore, we define three time scales associated with diffusion $(\hat{t}_D)$, reactions $(\hat{t}_R)$ and advection $(\hat{t}_A)$ as

$$\hat{t}_D = \frac{L^2}{D}, \quad \hat{t}_R = \frac{L}{\hat{k} \bar{c}^{a-1}}, \quad \hat{t}_A = \frac{L}{U}. \tag{4.6}$$

Ratios between these time scales define the dimensionless Damköhler $(\mathrm{Da} = \hat{t}_D / \hat{t}_R)$ and Péclet $(\mathrm{Pe} = \hat{t}_D / \hat{t}_A)$ numbers,

$$\mathrm{Da} = \frac{L \hat{k} \bar{c}^{a-1}}{D} \quad \text{and} \quad \mathrm{Pe} = \frac{UL}{D}. \tag{4.7}$$

Rewriting (5.1)-(4.4) in terms of the dimensionless quantities (4.5) and the dimensionless time $t = \hat{t} / \hat{t}_D$ yields a dimensionless form of the flow equations

$$\varepsilon^2 \nabla^2 \mathbf{v}_\varepsilon - \nabla p = 0, \qquad \nabla \cdot \mathbf{v}_\varepsilon = 0, \qquad \mathbf{x} \in B^\varepsilon, \tag{4.8}$$

subject to

$$\mathbf{v}_\varepsilon = \mathbf{0}, \qquad \mathbf{x} \in A_{ls}^\varepsilon \tag{4.9}$$

and a dimensionless form of the transport equation

$$\frac{\partial c_\varepsilon}{\partial t} + \nabla \cdot (-\mathbf{D}\nabla c_\varepsilon + \mathrm{Pe}\mathbf{v}_\varepsilon c_\varepsilon) = 0, \qquad \mathbf{x} \in B^\varepsilon, \qquad t > 0, \tag{4.10}$$

subject to

$$-\mathbf{n} \cdot \mathbf{D}\nabla c_\varepsilon = \mathrm{Da}\left(c_\varepsilon^a - 1\right), \qquad \mathbf{x} \in A_{ls}^\varepsilon, \qquad t > 0. \tag{4.11}$$

4.2.3 Periodic geometry & periodic coefficients

The boundary-value problems (4.8)–(4.9) and (4.10)–(4.11) are defined for the pore-space B^ε composed of periodically repeating unit cells B. These problems have constant coefficients (the fluid viscosity μ and the molecular diffusion coefficient $\mathbf{D}$) but have to be solved in the highly irregular flow domain B^ε. Alternatively, one can define these problems on a regular domain, the porous medium Ω composed of both the solid matrix G and the pore space B, by introducing spatially varying coefficients. This is accomplished as follows (see [16] for more details).

Let us introduce a scaled membership function $\pi_\varepsilon(\mathbf{x}) = \pi(\mathbf{x}/\varepsilon)$, where $\pi(\mathbf{x})$ is an indicator (membership) function

$$\pi(\mathbf{x}) = \begin{cases} 1, & \mathbf{x} \in B \\ 0, & \mathbf{x} \in G. \end{cases} \tag{4.12}$$

Then one can define spatially varying coefficients everywhere in the domain Ω,

$$\mathbf{D}_\varepsilon(\mathbf{x}) \equiv \pi_\varepsilon(\mathbf{x})\mathbf{D}, \qquad \mu_\varepsilon(\mathbf{x}) \equiv \pi_\varepsilon(\mathbf{x})\mu, \qquad \mathbf{x} \in \Omega. \tag{4.13}$$

By construction, the functions $\mathbf{D}_\varepsilon(\mathbf{x})$ and $\mu_\varepsilon(\mathbf{x})$ are periodic with the period $\mathscr{V}$ determined by the unit cell size. Equations (4.8) and (4.10) can now be defined on the domain Ω,

$$\varepsilon^2 \mu_\varepsilon \nabla^2 \tilde{\mathbf{v}}_\varepsilon - \nabla \tilde{p}_\varepsilon = 0, \quad \frac{\partial \tilde{c}_\varepsilon}{\partial t} + \nabla \cdot (-\mathbf{D}_\varepsilon \nabla \tilde{c}_\varepsilon + \mathrm{Pe}\tilde{\mathbf{v}}_\varepsilon \tilde{c}_\varepsilon) = 0, \quad \mathbf{x} \in \Omega, \tag{4.14}$$

where the state variables $(\tilde{\mathbf{v}}_\varepsilon, \tilde{p}_\varepsilon, \tilde{c}_\varepsilon)$ are respective extensions to Ω of their counterparts $(\mathbf{v}_\varepsilon, p_\varepsilon, c_\varepsilon)$. The two sets of these state variables coincide in B^ε [16, pp.14,15,46].

4.3 Homogenization via Multiple-Scale Expansions

Homogenization aims to derive effective equations for average state variables that are representative of an averaging volume (e.g., Darcy scale). To this end, three types of local averages of a quantity $\mathcal{A}(\mathbf{x})$ can be defined,

$$\langle \mathcal{A} \rangle \equiv \frac{1}{|\mathcal{V}|} \int\limits_{B(\mathbf{x})} \mathcal{A} \mathrm{d}\mathbf{y}, \quad \langle \mathcal{A} \rangle_B \equiv \frac{1}{|B|} \int\limits_{B(\mathbf{x})} \mathcal{A} \mathrm{d}\mathbf{y}, \quad \langle \mathcal{A} \rangle_{ls} \equiv \frac{1}{|A_{ls}|} \int\limits_{A_{ls}(\mathbf{x})} \mathcal{A} \mathrm{d}\mathbf{y}, \qquad (4.15)$$

where $\langle \mathcal{A} \rangle = \phi \langle \mathcal{A} \rangle_B$ and $\phi = |B|/|\mathcal{V}|$ is the porosity. In the subsequent derivation of effective (continuum- or Darcy-scale) equations for average flow velocity $\langle \mathbf{v}(\mathbf{x}) \rangle$ and solute concentration $\langle c(\mathbf{x}, t) \rangle$, we employ the method of multiple-scale expansions [19, 16].

4.3.1 Upscaled flow equations

Upscaling of the Stokes equations (4.8)-(4.9) at the pore-scale to the continuum scale has been the subject of numerous investigations, including those relying on multiple-scale expansions [16, 19, 20, and references therein]. These studies have demonstrated that Darcy's law and the continuity equation for $\langle \mathbf{v} \rangle$,

$$\langle \mathbf{v} \rangle = -\mathbf{K} \cdot \nabla p_0, \qquad \nabla \cdot \langle \mathbf{v} \rangle = 0, \qquad \mathbf{x} \in \Omega, \qquad (4.16)$$

provide an effective representation of the pore-scale Stokes flow (e.g., [16, Eq. 4.7]). Such homogenization procedures also enable one to formally define the dimensionless permeability tensor $\mathbf{K}$ in (4.16) as the average, $\mathbf{K} = \langle \mathbf{k}(\mathbf{y}) \rangle$, of a "closure variable" $\mathbf{k}(\mathbf{y})$. The latter is the unique solution of a local, or unit cell, problem (e.g., [16, pp. 46-47, Theorem 1.1] and [19, Eq. 22])

$$\nabla^2 \mathbf{k} + \mathbf{I} - \nabla \mathbf{a} = \mathbf{0}, \qquad \nabla \cdot \mathbf{k} = \mathbf{0}, \qquad \mathbf{y} \in B \qquad (4.17)$$

subject to the boundary condition $\mathbf{k}(\mathbf{y}) = \mathbf{0}$ for $\mathbf{y} \in A_{ls}$. The vector $\mathbf{a}$ is $\mathcal{V}$-periodic and satisfies the condition $\langle \mathbf{a} \rangle = 0$. Consequently, the second-order tensor $\mathbf{k}$ is $\mathcal{V}$-periodic as well.

4.3.2 Upscaled transport equation

The method of multiple-scale expansions introduces a fast space variable $\mathbf{y}$ and two time variables τ_r and τ_a,

$$\mathbf{y} = \frac{\mathbf{x}}{\varepsilon}, \qquad \tau_r = \mathrm{Da}\, t = \frac{\hat{t}}{\hat{t}_R}, \qquad \tau_a = \mathrm{Pe}\, t = \frac{\hat{t}}{\hat{t}_A}. \tag{4.18}$$

Furthermore, it represents the concentration $c_\varepsilon(\mathbf{x}, t)$ in (4.10), or its counterpart in (4.14), as $c_\varepsilon(\mathbf{x}, t) := c(\mathbf{x}, \mathbf{y}, t, \tau_r, \tau_a)$. The latter is expanded into an asymptotic series in powers of ε,

$$c(\mathbf{x}, \mathbf{y}, t, \tau_r, \tau_a) = \sum_{m=0}^{\infty} \varepsilon^m c_m(\mathbf{x}, \mathbf{y}, t, \tau_r, \tau_a), \tag{4.19}$$

wherein $c_m(\mathbf{x}, \mathbf{y}, t, \tau_r, \tau_a)$ $(m = 0, 1, \ldots)$ are $\mathscr{V}$-periodic in $\mathbf{y}$. Finally, we set

$$\mathrm{Pe} = \varepsilon^{-\alpha} \quad \text{and} \quad \mathrm{Da} = \varepsilon^{\beta}, \tag{4.20}$$

with the exponents α and β determining the system behavior. For example, transport due to advection and dispersion at the pore scale is not homogenizable if $\alpha \geq 2$ [19, Sec. 3.5, Tab. 1].

We show in Appendix B that pore-scale reactive transport processes described by (4.10)–(4.11) can be homogenized, i.e., approximated up to order ε^2 with an effective ADRE

$$\phi \frac{\partial \langle c \rangle_B}{\partial t} = \nabla \cdot (\mathbf{D}^* \nabla \langle c \rangle_B - \mathrm{Pe} \langle c \rangle_B \langle \mathbf{v} \rangle) - \varepsilon^{-1} \phi \mathrm{Da} \mathscr{K}^* (\langle c \rangle_B^a - 1), \quad \mathbf{x} \in \Omega, \tag{4.21}$$

provided the following conditions are met:

1) $\varepsilon \ll 1$,

2) $\mathrm{Pe} < \varepsilon^{-2}$,

3) $\mathrm{Da}/\mathrm{Pe} < \varepsilon$,

4) $\mathrm{Da} < 1$,

5) $\langle \boldsymbol{\chi} \rangle_{ls} \approx \langle \boldsymbol{\chi} \rangle_B$.

In (4.21), the dimensionless effective reaction rate constant $\mathscr{K}^*$ is determined by the pore geometry,

$$\mathscr{K}^* = \frac{|A_{ls}|}{|B|}, \tag{4.22}$$

and the dispersion tensor $\mathbf{D}^*$ is given by

$$\mathbf{D}^* = \langle \mathbf{D}(\mathbf{I} + \nabla_{\mathbf{y}}\boldsymbol{\chi}) \rangle + \varepsilon \operatorname{Pe} \langle \boldsymbol{\chi}\mathbf{k} \rangle \nabla_{\mathbf{x}} p_0. \tag{4.23}$$

The closure variable $\boldsymbol{\chi}(\mathbf{y})$ has zero mean, $\langle \boldsymbol{\chi} \rangle = \mathbf{0}$, and is defined as a solution of the local problem

$$- \nabla_{\mathbf{y}} \cdot \mathbf{D}(\nabla_{\mathbf{y}}\boldsymbol{\chi} + \mathbf{I}) + \varepsilon \operatorname{Pe} \mathbf{v}_0 \nabla_{\mathbf{y}}\boldsymbol{\chi} = \varepsilon \operatorname{Pe} (\langle \mathbf{v}_0 \rangle_B - \mathbf{v}_0), \qquad \mathbf{y} \in B; \tag{4.24a}$$

$$- \mathbf{n} \cdot \mathbf{D}(\nabla_{\mathbf{y}}\boldsymbol{\chi} + \mathbf{I}) = 0, \qquad \mathbf{y} \in A_{ls}; \tag{4.24b}$$

where $\mathbf{v}_0 = -\mathbf{k}\cdot\nabla_{\mathbf{x}} p_0$ and the pressure p_0 is a solution of the effective flow equation (4.16).

Constraints 1)–4) ensure the separation of scales. While constraint 1) is almost always met in practical applications, the rest of them depend on the relative importance of advective, diffusive, and reactive mechanisms of transport. These conditions are summarized in the phase diagram in Fig. 4.1, where the line $\beta = 0$ refers to $\operatorname{Da} = 1$ and the half-space $\beta > 0$ to $\operatorname{Da} < 1$ because $\varepsilon < 1$; the line $\alpha = 2$ refers to $\operatorname{Pe} = \varepsilon^{-2}$ and the half-space $\alpha < 2$ refers to $\operatorname{Pe} < \varepsilon^{-2}$; the line $\alpha + \beta = 1$ refers to $\operatorname{Da}/\operatorname{Pe} = \varepsilon$; and the half-space underneath this line refers to $\operatorname{Da}/\operatorname{Pe} < \varepsilon$. Constraints 3) and 4) require that either diffusion or advection-diffusion dominate reactions at the pore scale. This allows one to decouple the pore- and continuum-scale descriptions (see Appendix B.2). Constraint 5) is not required for scale separation, but facilitates the derivation of the effective parameters (4.22) and (4.23). As shown in Appendix B.3, this constraint allows one to interchange the surface and volume averages, $\langle c_1 \rangle_{ls} \approx \langle c_1 \rangle_B$, within errors on the order of ε^2.

The results above generalize the conclusions of the analysis of reactive-diffusive transport performed in Chapter 3 [56], which relied on the method of volume averaging. While using different upscaling approaches, both analyses provide the same bound on the Damköhler number Da in the absence of advection. The effective reaction rate $\mathscr{K}^*$ for heterogeneous reactions (4.22) is likewise consistent with that obtained in [56]. This suggests that the conditions for validity and breakdown of continuum models of reactive transport presented in the phase diagram in Fig. 4.1 are universal and independent of the upscaling method. Finally, these upscaling results justify the use of reaction terms
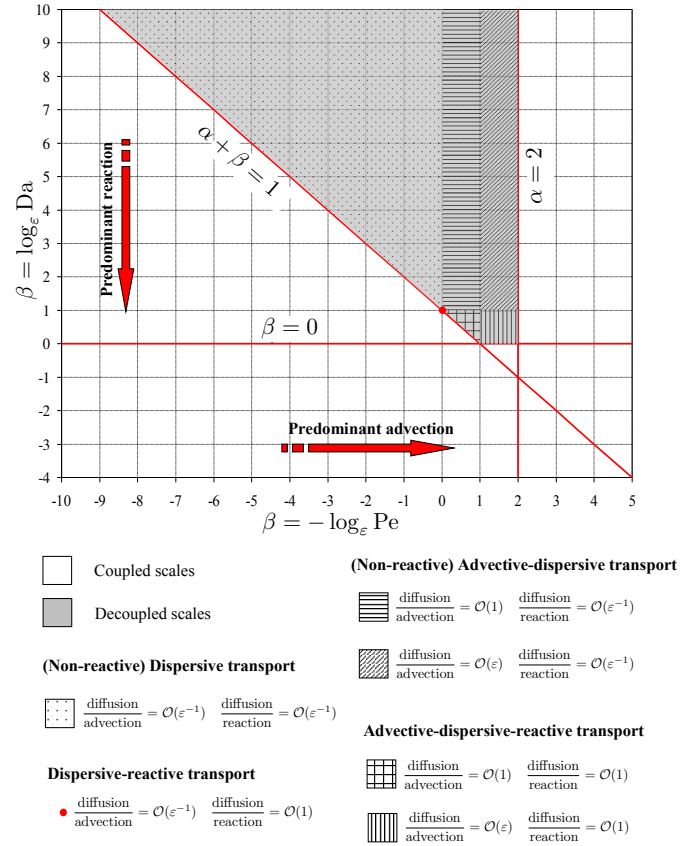
Figure 4.1: Phase diagram indicating the range of applicability of macroscopic equations for the advection-reaction-diffusion system (4.10)-(4.11) in terms of Pe and Da. The grey region identifies the sufficient conditions under which the macroscopic equations hold. In the white region, macro- and micro-scale problems are coupled and have to be solved simultaneously. Also identified are different transport regimes depending on the order of magnitude of Pe and Da. Diffusion, advection, and reaction are of the same order of magnitude at the point $(\alpha, \beta) = (1, 0)$.

similar to the one in (4.21) in continuum models of precipitation and dissolution processes in porous media (e.g., [90, 91, 92]).

4.4 Special cases

In this section, we explore specific flow and transport regimes under which general forms of the upscaled equation (4.21) and the closure problem (4.24) can be simplified. Specifically, we demonstrate how the conditions identified in [19] for advection-dispersion transport of conservative solute can be derived from (4.21) and (4.24). As briefly mentioned in section 4.3.2 and thoroughly discussed in Appendix B.2, constraints 3) and 4) ensure that reactions are negligible at the pore level. Hence, the following regimes are either diffusion or advection-diffusion dominated at the pore scale.

4.4.1 Transport regime with $\varepsilon \leq \mathrm{Pe} < 1$

In this regime $(-1 \leq \alpha < 0)$, diffusion dominates advection at the macro-scale and (4.21) reduces to a dispersion-reaction equation

$$\varepsilon\phi\frac{\partial\langle c\rangle_B}{\partial t} = \varepsilon\nabla_{\mathbf{x}} \cdot (\mathbf{D}^*\nabla_{\mathbf{x}}\langle c\rangle_B) - \mathrm{Da}\,\phi\,\mathscr{K}^*(\langle c\rangle_B^a - 1), \tag{4.25}$$

where $\mathbf{D}^* = \langle \mathbf{D}(\mathbf{I} + \nabla_{\mathbf{y}}\boldsymbol{\chi})\rangle$ and the closure problem (4.24) simplifies to

$$-\nabla_{\mathbf{y}} \cdot \mathbf{D}(\nabla_{\mathbf{y}}\boldsymbol{\chi} + \mathbf{I}) = 0, \qquad \mathbf{y} \in B; \tag{4.26a}$$

$$\mathbf{n} \cdot \mathbf{D}(\nabla_{\mathbf{y}}\boldsymbol{\chi} + \mathbf{I}) = 0, \qquad \mathbf{y} \in A_{ls}. \tag{4.26b}$$

The magnitude of the Damköhler number Da determines the effects of chemical reactions on transport.

Diffusion dominates reactions, $\mathrm{Da} < \varepsilon$

In this regime $(\beta > 1$, the dot-patterned region in Fig. 4.1), the diffusion term in the macro-scale equation (4.25) dominates the reaction term, so that (4.25) simplifies to a non-reactive dispersion equation

$$\phi\frac{\partial\langle c\rangle_B}{\partial t} = \nabla \cdot (\mathbf{D}^*\nabla\langle c\rangle_B), \tag{4.27}$$

which coincides with equations (45) and (46) in [19].

Diffusion and reaction are comparable, $\mathrm{Da} = \varepsilon$

In this regime ($\beta = 1$, the red dot in Fig. 4.1), the reaction term in the effective equation (4.25) cannot be neglected. Reactive transport at the macro-scale is described by the dispersion-reaction equation (4.25).

4.4.2   Transport regime with $1 \leq \mathrm{Pe} < \varepsilon^{-1}$

In this regime ($0 \leq \alpha < 1$), the effects of advection and diffusion at the macro-scale are of the same order. While the advective term can be neglected in the closure problem (4.24), it has to be retained in the effective equation (4.21). Consequently, reactive transport at the macro-scale is described by the advection-dispersion-reaction equation (4.21) with the effective dispersion tensor $\mathbf{D}^* = \langle \mathbf{D}(\mathbf{I} + \nabla\boldsymbol{\chi})\rangle$, in which the closure variable $\boldsymbol{\chi}(\mathbf{y})$ is a solution of (4.26).

Diffusion and advection dominate reactions, $\mathrm{Da} < \varepsilon$

In this regime ($\beta > 1$, the horizontal-line-patterned region in Fig. 4.1), (4.21) reduces to a non-reactive advection-dispersion equation

$$\phi\frac{\partial \langle c \rangle_B}{\partial t} = \nabla \cdot (\mathbf{D}^*\nabla\langle c\rangle_B) - \mathrm{Pe}\nabla \cdot (\langle c\rangle_B\langle\mathbf{v}\rangle), \tag{4.28}$$

and the closure problem is given by (4.26). This upscaled model is identical to that derived in [19, Eqs. 46 and 51] for advection-dispersion transport of passive solutes.

Diffusion and reactions are comparable, $\varepsilon \leq \mathrm{Da} < 1$

In this regime ($0 < \beta \leq 1$, the square-patterned region in Fig. 4.1), pore-scale transport is still diffusion driven, and $\boldsymbol{\chi}$ and $\mathbf{D}^*$ are defined by (4.26) and $\mathbf{D}^* = \langle \mathbf{D}(\mathbf{I} + \nabla\boldsymbol{\chi})\rangle$, respectively. At the macro-scale, the reaction term is not negligible, so that the effective transport equation (4.21) is to be used.

4.4.3   Transport regime with $\varepsilon^{-1} \leq \mathrm{Pe} < \varepsilon^{-2}$

In this regime ($1 \leq \alpha < 2$), advection dominates diffusion at the macro-scale and transport is described by (4.21). Since at the pore scale these two transport mechanisms

are of the same order, the effective dispersion tensor $\mathbf{D}^*$ is given by (4.23) and the closure variable $\boldsymbol{\chi}$ is obtained by solving the cell problem (4.24). The magnitude of the Damköhler number Da determines the following sub-regimes.

Diffusion dominates reactions, $\mathrm{Da} < \varepsilon$

In this regime ($\beta > 1$, the diagonal-line-patterned region in Fig. 4.1), diffusion dominates reactions at continuum scale. The effective transport equation (4.21) reduces to (4.28) wherein the dispersion tensor $\mathbf{D}^*$ is given by (4.23). The latter transport model coincides with that derived in [19, Eqs. 61, 65, 68].

Diffusion and reactions are comparable, $\varepsilon \leq \mathrm{Da} < 1$

In this regime ($0 < \beta \leq 1$, the vertical-line patterned region in Fig. 4.1), transport is advection-dominated (reactions are negligible) at the pore-scale, but diffusion and reactions at the macro-scale are of the same order of magnitude. Hence, both the effective dispersion tensor $\mathbf{D}^*$ and the closure variable $\boldsymbol{\chi}$ are defined as in section 4.4.3 and the effective transport model is the advection-dispersion-reaction equation (4.21).

4.5   Conclusions

Reactive transport in porous media is a complex nonlinear phenomenon that often involves both homogeneous and heterogeneous reactions of (bio-)chemical species dissolved in a liquid phase. The relative importance of advection, molecular diffusion, and reactions (three key pore-scale transport mechanisms) is quantified by the Péclet (Pe) and Damköhler (Da) numbers. We considered transport of a solute that undergoes nonlinear heterogeneous reactions: after reaching a threshold concentration, it precipitates on the solid matrix to form a crystalline solid. The main goal of this study was to establish sufficient conditions under which macroscopic advection-dispersion-reaction equations (ADREs) provide an accurate description of pore-scale processes. To accomplish this, we used multiple-scale expansions to upscale to the continuum (Darcy) scale a pore-scale advection-diffusion equation with reactions entering through a boundary condition on the fluid-solid interfaces. Our analysis leads to the following major conclusions.

1. The range of applicability of macroscopic ADREs and various transport regimes can be described with a phase diagram in the (Pe, Da) space (Fig. 4.1). The latter is parameterized with the scale-separation parameter ε that is defined as the ratio of characteristic lengths associated with the pore- and macro-scales.

2. This phase diagram reveals that transport phenomena dominated at the pore scale by reaction processes do not lend themselves to macroscopic (upscaled) descriptions. Under these conditions, the validity of assumptions and approximations underlying macroscopic ADREs, such as (4.21), cannot be ascertained a priori.

3. The constraints on Pe and Da obtained in the present analysis are consistent with those derived for diffusion-reaction transport in [56] by means of volume averaging, which suggests that these results are universal, i.e., are independent of the choice of an upscaling technique.

4. The constraints on Pe derived in [19] follow from our formulation as special cases.

5. For transport regimes, in which continuum (Darcy-scale) equations breakdown, non-local (integro-differential) or hybrid pore-scale/continuum-scale models should be used, as they provide a more rigorous alternative to classical upscaled models based on closure assumptions and approximations.

In following Chapters we will develop hybrid algorithms that couple a pore-scale model in the regions where the valididty of macroscale models cannot be ascertained a priori with continuum descriptions elsewhere in a computational domain.

Battiato, I., Tartakovsky, D. M., (2010), 'Applicability Regimes for Macroscopic Models of Reactive Transport in Porous Media'. Journ. Cont. Hydrol., Special Issue, Invited, http://dx.doi.org/10.1016/j.jconhyd.2010.05.005.

Chapter 5

Hybrid Model for Reactive Flow in a Fracture

5.1 Introduction

In this Chapter we present a hybrid algorithm that couples pore-scale simulations in a small domain Ω_p with continuum simulations elsewhere in the computational domain, Ω/Ω_p. The coupling is accomplished via an iterative procedure in a handshake region Ω_{pc}, where both pore-scale and continuum-scale descriptions are solved iteratively to ensure the continuity of state variables and their fluxes across the interface between Ω_p and the rest of the computational domain.

Section 5.1.1 contains a general formulation of flow and transport equations at the pore (section 5.1.1) and continuum (section 5.1.2) scales, as well as an outline of the proposed hybrid algorithm (section 5.1.3). Both the hybrid formulation and its numerical implementation are made concrete in section 5.2 by applying them to model Taylor dispersion in a planar fracture with chemically reactive walls. In section 5.3, we use this well-studied problem to validate our hybrid algorithm via comparison with analytical solutions and two-dimensional pore-scale numerical simulations.

5.1.1 Governing equations at the pore scale

Consider reactive transport in a fully-saturated porous medium Ω^T. Within the pore space Ω^T_{pore} contained in Ω^T, single-phase flow of an incompressible fluid is described by the Stokes and continuity equations,

$$\mu \nabla^2 \mathbf{v} - \nabla p = \mathbf{0}, \qquad \nabla \cdot \mathbf{v} = 0, \tag{5.1}$$

where $\mathbf{v}$, p and μ are the fluid's velocity, dynamic pressure, and dynamic viscosity, respectively. Flow equations (5.1) are subject to the no-slip boundary condition on the solid-liquid interface A^T_{sl}, which is taken to be impermeable to flow, i.e, $\mathbf{v} = \mathbf{0}$ for $\mathbf{x} \in A^T_{sl}$. The flow is driven by boundary conditions imposed on $\partial \Omega^T$, the external boundary of Ω^T.

The fluid contains a dissolved species with molar concentration $c(\mathbf{x}, t)$ $[ML^{-3}]$ that undergoes advection, molecular diffusion and a linear heterogeneous reaction at the solid-liquid interface A^T_{sl}. The evolution of $c(\mathbf{x}, t)$ is described by an advection-diffusion equation,

$$\frac{\partial c}{\partial t} + \nabla \cdot (\mathbf{v}c) = \mathscr{D} \nabla^2 c, \tag{5.2a}$$

subject to the boundary condition on the solid-fluid interface A^T_{sl},

$$-\mathbf{n} \cdot \mathscr{D} \nabla c = \mathscr{K} c, \tag{5.2b}$$

and proper boundary conditions on $\partial \Omega^T$. Here $\mathscr{D}$ $[L^2 T^{-1}]$ is the molecular diffusion coefficient, $\mathscr{K}$ $[LT^{-1}]$ is the reaction constant describing an interface reaction (e.g., linear microbial degradation), and $\mathbf{n}$ is the outward unit normal vector of A^T_{sl}.

5.1.2 Governing equations at the continuum scale

Let $\overline{A}(\mathbf{x}, t)$ denote the volumetric average of a pore-scale quantity $A(\mathbf{x}, t)$ defined as

$$\overline{\mathcal{A}}(\mathbf{x}, t) \equiv \frac{1}{\phi ||\mathscr{V}||} \int_{\mathscr{V}(\mathbf{x})} \mathcal{A}(\mathbf{y}, t) \mathrm{d}\mathbf{y}, \tag{5.3}$$

where ϕ is the porosity of a porous medium and the averaging volume $\mathcal{V}$ might or might not constitute a representative elementary volume (REV). Averaging (5.1), i.e., upscaling the flow equations from the pore scale to the continuum scale, leads to Darcy's law [19],

$$\mathbf{V} = -\mathbf{K}\nabla\overline{p}, \tag{5.4}$$

where $\mathbf{K}$ is the permeability of the porous medium, and $\mathbf{V} = \phi\overline{\mathbf{v}}$ is Darcy's flux. Among other simplifying assumptions, the validity of (5.4) requires that the Reynolds number Re_c satisfy the inequality [17, p.74, and the references therein]

$$\mathrm{Re}_c \equiv \frac{|\mathbf{V}|d}{\nu} < 10, \tag{5.5}$$

where d is a typical length associated with grain geometry, and ν is the fluid's kinematic viscosity.

A corresponding continuum-scale formulation of the pore-scale transport problem (5.2) typically used in practice is

$$\phi\frac{\partial\overline{c}}{\partial t} + \phi\nabla\cdot(\mathbf{V}\overline{c}) = \nabla\cdot(\mathbf{D}\nabla\overline{c}) - K\overline{c}, \tag{5.6}$$

where $\mathbf{D}$ is the dispersion tensor, and K is the effective reaction rate. Equation (5.6) can be derived by standard upscaling methodologies, e.g., multiple-scale expansions or volumetric averaging, e.g. [55, and references therein]. Regardless of the choice of an upscaling technique, a number of simplifying approximations are required for (5.6) to be valid [55, 56].

5.1.3   General hybrid formulation

We are concerned with transport regimes in which $\mathrm{Re}_c < 10$, i.e., the Darcy law (5.4) is valid over the whole computational domain Ω^T but one or more of the sufficient conditions [55, 56] for the validity of the continuum-scale transport equation (5.6) break down in a sub-domain Ω_p of the computational domain Ω (Fig. 5.1). In Ω_p the averaging of (5.2) results in an integro-differential equation

$$\phi\frac{\mathrm{d}\overline{c}}{\mathrm{d}t} + \overline{\nabla\cdot(\mathbf{v}c)} = \mathscr{D}\overline{\nabla^2 c}, \tag{5.7}$$

where the averaging (5.3) is now defined over $\mathscr{V} \equiv \Omega_p(\mathbf{x}^\star)$ and $\mathbf{x}^\star$ is the centroid of Ω_p, i.e., the subdomain Ω_p shrinks to a point $\mathbf{x}^\star \in \Omega^T$. Violation of some of the sufficient conditions [55, 56] prevents the averaging integrals in (5.7) from being converted into the corresponding terms for the macroscopic (average) concentration $\bar{c}$ in (5.6).
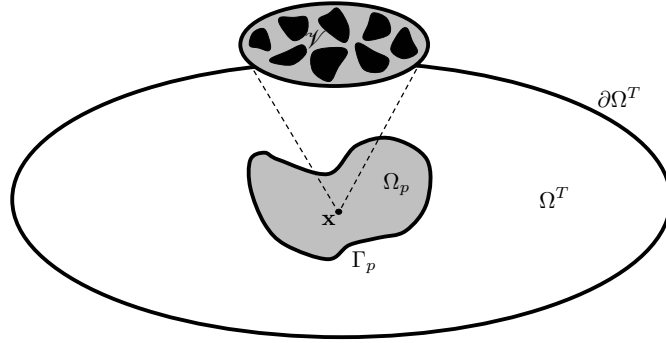
Figure 5.1: A schematic representation of the pore- and continuum-scale domains.

Then, according to Gauss' theorem, (5.7) can be rewritten as

$$\phi \frac{\mathrm{d}\bar{c}}{\mathrm{d}t} = \frac{1}{\phi \|\Omega_p\|} \int_{A_p} \mathbf{n} \cdot (\mathscr{D}\nabla c - \mathbf{v}c)\mathrm{d}s, \tag{5.8}$$

where A_p is the bounding surface of Ω_p, and $\mathrm{d}s$ is an infinitesimal element of A_p. Since the surface $A_p = A_{ll}^p \cup A_{sl}^p$ consists of liquid-liquid (A_{ll}^p) and solid-liquid (A_{sl}^p) segments, boundary condition (5.2b) and the no-slip condition yield

$$\phi \frac{\mathrm{d}\bar{c}}{\mathrm{d}t} = -\frac{1}{\phi \|\Omega_p\|} \int_{A_{ll}^p} q_n \, \mathrm{d}s - \frac{1}{\phi \|\Omega_p\|} \int_{A_{sl}^p} \mathscr{K} c \, \mathrm{d}s, \tag{5.9}$$

where $q_n = \mathbf{n} \cdot (\mathbf{v}c - \mathscr{D}\nabla c)$ is the flux through the liquid-liquid portion of the boundary, A_p. The right hand side of (5.9) depends on pore-scale quantities. It represents the fluxes exchanged at the boundary A_p between the pore- and continuum-scale descriptions. Multiscale approaches [52, 47, 44, among others] aim to decouple the two descriptions by employing closure assumptions for the the unresolved flux, q_n. A typical strategy is to represent the pore-scale concentration $c = \bar{c} + c'$ as the sum of its average $\bar{c}$ and corresponding fluctuations c', to linearize $f(c) = f(\bar{c}) + c'(\mathrm{d}f/\mathrm{d}c)_{|c=\bar{c}} + \cdots$, to postulate a numerical or analytical closure for c', and to impose boundary conditions on A_p (the most common being a periodic condition).

In contrast, our goal is to preserve the nonlinearity of the problem and to compute the unresolved normal flux q_n without any assumption on the microscale behavior. This will allow us to bypass the assumptions needed for continuum-scale models. To this end, we obtain the pore-scale concentration $c(\mathbf{x}, t)$ in (5.9) by solving the transport problem (5.2) defined on Ω_p. The boundary condition (5.2b) is now defined on the union of all solid-liquid surfaces A_{sl} contained in Ω_p. On the fluid-fluid segments A_{ll}^p, mass conservation requires that $\mathbf{n} \cdot (\mathscr{D}\nabla c - \mathbf{v}c) = q_n$. The flux q_n, which represents a boundary condition for the pore-scale problem (5.2) and a source term for the continuum-scale equation (5.9), is unknown.

In summary, the hybrid pore-scale/continuum scale algorithm contains the three unknowns $(c, \bar{c}, q_n)$ that satisfy a system of coupled nonlinear partial-differential equations,

$$\phi\frac{\partial\bar{c}}{\partial t} + \phi\nabla\cdot(\mathbf{V}\bar{c}) = \nabla\cdot(\mathbf{D}\nabla\bar{c}) - K\bar{c}, \qquad \mathbf{x}\in\Omega^T, \quad t > 0 \qquad (5.10)$$

$$\phi\frac{\mathrm{d}\bar{c}}{\mathrm{d}t} = \frac{1}{\phi||\Omega_p||}\int\limits_{A_{ll}} q_n\mathrm{d}\mathbf{x} - \frac{1}{\phi||\Omega_p||}\int\limits_{A_{sl}} \mathscr{K}c\mathrm{d}\mathbf{x}, \qquad \mathbf{x} = \mathbf{x}^\star, \quad t > 0 \qquad (5.11)$$

$$\frac{\partial c}{\partial t} + \nabla\cdot(\mathbf{v}c) = \mathscr{D}\nabla^2 c, \qquad \mathbf{x}\in\Omega_p, \quad t > 0 \qquad (5.12)$$

$$\mathbf{n}\cdot(\mathscr{D}\nabla c - \mathbf{v}c) = q_n, \qquad \mathbf{x}\in A_{ll}, \quad t > 0 \qquad (5.13)$$

$$-\mathbf{n}\cdot\mathscr{D}\nabla c = \mathscr{K}c, \qquad \mathbf{x}\in A_{sl}, \quad t > 0, \qquad (5.14)$$

supplemented by boundary conditions on the external domain $\partial\Omega^T$ and initial conditions.

In the following section we apply this hybrid algorithm to analyze Taylor dispersion in a fracture with chemically reactive walls.

5.2 Taylor dispersion in a fracture with reactive walls

Consider transport of a reactive solute by advection and diffusion in a fracture of width $2H$. The solute undergoes a first-order heterogeneous reaction at the walls of the channel. The flow domain $\Omega = \{(x, y) : x \in (0, \infty), |y| < H\}$ has the boundary $A = \{(x, y) : x \in (0, \infty), |y| = H\}$.

Assuming laminar, fully developed flow inside the fracture, the "pore-scale" ve-

locity in (5.1) is given by Poiseuille's law, $\mathbf{v} = (u, 0)^T$, where

$$u(y) = u_m \left[1 - \left(\frac{y}{H} \right)^2 \right] \tag{5.15}$$

and u_m is the maximum velocity at the center of the fracture $(y = 0)$. General pore-scale transport equations (5.2) reduce to

$$\frac{\partial c}{\partial t} + u(y) \frac{\partial c}{\partial x} - \mathscr{D} \left(\frac{\partial^2 c}{\partial x^2} + \frac{\partial^2 c}{\partial y^2} \right) = 0, \qquad (x, y) \in \Omega, \quad t > 0 \tag{5.16a}$$

$$-\mathscr{D} \frac{\partial c}{\partial y} = \mathscr{K} c, \qquad (x, y) \in A, \quad t > 0. \tag{5.16b}$$

The average concentration $\bar{c}(x, t)$ in (5.3) is now defined as

$$\bar{c}(x, t) \equiv \frac{1}{2H} \int\limits_{-H}^{H} c(x, y, t) \mathrm{d}y. \tag{5.17}$$

It satisfies a version of the continuum or Darcy-scale transport equation (5.6) that has the form [20]

$$\frac{\partial \bar{c}}{\partial t} + U \frac{\partial \bar{c}}{\partial x} + K \bar{c} = D \frac{\partial^2 \bar{c}}{\partial x^2}, \qquad x \in (0, \infty), \quad t > 0, \tag{5.18a}$$

where

$$U = u_m \left(\frac{2}{3} + \frac{4 \mathrm{Da}_y}{45} \right), \quad K = \frac{\mathscr{K}}{H} \left(1 - \frac{\mathrm{Da}_y}{3} \right), \quad D = \mathscr{D} \left(1 + \frac{8 \mathrm{Pe}_y^2}{945} \right) \tag{5.18b}$$

and

$$\mathrm{Pe}_y = \frac{u_m H}{\mathscr{D}}, \qquad \mathrm{Da}_y = \frac{\mathscr{K} H}{\mathscr{D}}. \tag{5.18c}$$

The validity of (5.18) requires that L, a macroscopic characteristic length scale in the x direction, be much larger than H, i.e., $\epsilon = H/L \ll 1$; and places a number of constraints on the order of magnitude of Pe and Da (see the phase diagram in [55]).

Our focus is on transport regimes wherein one or more of these constraints are violated in a small portion of the computational domain, $\Omega_p = \{(x, y) : x \in (a, b), |y| < H\}$. Equation (5.18) is valid in the rest of the computational domain. To simplify the presentation, we assume that Ω_p corresponds to a single macroscale grid block. Domains Ω_p that are larger than a single grid block can be easily handled by following a procedure

similar to that described below. Possible effects on numerical robustness are discussed in [47, p. 511].

Since (5.18) is no longer valid in Ω_p, we employ its nonlocal counterpart (5.9), which for the problem under consideration takes the form

$$\frac{\partial \overline{c}}{\partial t} = \mathscr{D}\frac{\partial^2 \overline{c}}{\partial x^2} - \frac{\mathscr{K} J_c}{2H} - \overline{u(y)\frac{\partial c}{\partial x}}, \qquad (x, y) \in \Omega_p \tag{5.19}$$

where $J_c = c(x, H) + c(x, -H)$ and the pore-scale concentration $c(x, y, t)$ satisfies (5.16). Equation (5.19) is supplemented by the boundary conditions at the internal boundary $A_p = \{(x, y) : x = a, b; y \in (-H, H)\}$,

$$\mathbf{n} \cdot (\mathbf{v}c - \mathscr{D}\nabla c) = q_n. \tag{5.20}$$

The following sections contain a finite-volume discretization of the averaged equations (5.18) and (5.19). A finite-volume discretization of the pore-scale equations (5.16) is standard and not presented explicitly.

5.2.1 Finite-volume formulation

We discretize the macroscopic space-time domain into N_X and N_T intervals of width ΔX_I and ΔT, respectively (Fig. 5.2). Spatial nodes of the macroscopic domain, Ω/Ω_p, are defined as

$$X_{I+1} = X_I + (\Delta X_I + \Delta X_{I+1})/2, \qquad I = 1, \ldots, N_X \tag{5.21}$$

and their temporal counterparts are defined as

$$T_N = N\Delta T, \qquad N = 0, 1, \ldots, N_T. \tag{5.22}$$

The western and eastern boundaries of each control volume (CV) centered at X_I are given by $X_{I-1/2} = X_I - \Delta X_I/2$ and $X_{I+1/2} = X_I + \Delta X_I/2$, respectively. The distance between two adjacent nodes is $\Delta X_{I+1/2} = X_{I+1} - X_I$. The western and eastern boundaries of the computational domain coincide with the western and eastern boundaries of the first and last CVs, $X_{1/2}$ and $X_{N_T+1/2}$, respectively.

Let $I^\star$ denote the index of the CV in which the standard macroscopic equation (5.18) breaks down, and both its nonlocal counterpart (5.19) and the pore-scale
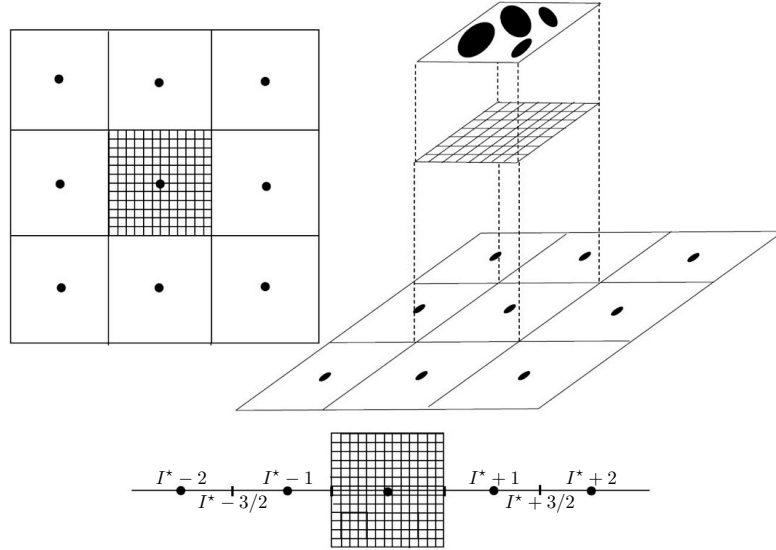
Figure 5.2: A finite-volume discretization of the computational domain for a fully 2D coupling (top images) and a hybrid 1D/2D formulation (bottom image).

transport equation (5.16) have to be solved instead. In the rest of the computational domain, (5.18) is valid. The $I^\star$-th CV is discretized into n_x and n_y intervals of width Δx_i and Δy_j in the x and y directions, respectively. Spatial nodes (x_i, y_i) of the microscopic domain Ω_p (the $I^\star$-th CV) are defined as

$$x_{i+1} = x_i + (\Delta x_i + \Delta x_{i+1})/2, \qquad\qquad i = 1, \ldots, n_x \qquad (5.23a)$$

$$y_{j+1} = y_j + (\Delta y_j + \Delta y_{j+1})/2, \qquad\qquad j = 1, \ldots, n_y. \qquad (5.23b)$$

The four surfaces bounding a CV centered at (x_i, y_j) are at locations $x_{i-1/2} = x_i - \Delta x_i/2$ (west), $x_{i+1/2} = x_i + \Delta x_i/2$ (east), $y_{j-1/2} = y_j - \Delta y_j/2$ (south), and $y_{j+1/2} = y_j + \Delta y_j/2$ (north). The distances between two adjacent nodes in the x and y directions are $\Delta x_{i+1/2} = x_{i+1} - x_i$ and $\Delta y_{j+1/2} = y_{j+1} - y_j$, respectively. The western and eastern boundaries of Ω_p coincide with the western and eastern boundaries of the $I^\star$-th macroscopic CV, $X_{I^\star - 1/2}$ and $X_{I^\star + 1/2}$, respectively (see the bottom image in Fig. 5.2). Time t in the pore-scale simulations is discretized into n_t intervals of width Δt, such that $\Delta T = n_t \Delta t$ and $t_n = n \Delta t$ with $n = 0, 1, \ldots$.

Let us define $\bar{c}_I^N = \bar{c}(X_I, T_N)$ and $c_{i,j}^n = c(x_i, y_j, t_n)$. In Appendix C.1 we derive a finite-volume fully-implicit approximation of macroscopic equations (5.18) and (5.19)

for nodes $I = \{1, \cdots, I^\star - 1\} \cup \{I^\star + 1, \cdots, N_X\}$,

$$A_{I-1}\bar{c}_{I-1}^{N+1} + A_I \bar{c}_I^{N+1} + A_{I+1}\bar{c}_{I+1}^{N+1} = \text{RHS}_I^N, \tag{5.24}$$

where

$$A_{I-1} = -a_{I-1}, \quad A_I = \frac{\Delta X_I}{\Delta T} + \bar{a}_I, \quad A_{I+1} = -a_{I+1}, \quad a_0 = 0 \tag{5.25a}$$

$$a_{I+1} = \max\left(-U, \mathcal{D}_{I+1/2} - \frac{U}{2}, 0\right), \quad \mathcal{D}_{I+1/2} = \frac{D}{\Delta X_{I+1/2}} \tag{5.25b}$$

$$a_{I-1} = \max\left(-U, \mathcal{D}_{I-1/2} + \frac{U}{2}, 0\right), \quad \mathcal{D}_{I-1/2} = \frac{D}{\Delta X_{I-1/2}} \tag{5.25c}$$

$$a_{N_X a} = 0, \quad \bar{a}_I = a_{I-1} + a_{I+1} + K\Delta X_I - \overline{S}_I \tag{5.25d}$$

$$\text{RHS}_I^N = \frac{\Delta X_I}{\Delta T}\bar{c}_I^N + \tilde{S}_I, \tag{5.25e}$$

and $\tilde{S}_I$ and $\overline{S}_I$ can be obtained through numerical discretization of boundary conditions at the macroscale.

At node $I^\star$, the coefficients in (5.24) take the form (Appendix C.2)

$$A_{I^\star-1} = -d_{I^\star-1/2}, \quad A_I^\star = \frac{\Delta X_{I^\star}}{\Delta T} + d_{I^\star-1/2} + d_{I^\star+1/2}, \quad A_{I^\star+1} = -d_{I^\star+1/2}, \tag{5.26a}$$

$$\text{RHS}_{I^\star}^N = \frac{\Delta X_{I^\star}}{\Delta T}\bar{c}_{I^\star}^N + \frac{1}{2HN_T}\sum_{k=1}^{n_t} G^{k+1} \tag{5.26b}$$

with

$$G^k = -\mathcal{K}\sum_{i=1}^{n_x}\Delta x_i(c_{i,H}^k + c_{i,-H}^k) - \begin{cases} \int_{-H}^H g_1^k \mathrm{d}y & \text{if Pe} \in (-2,2) \\ \int_{-H}^H g_2^k \mathrm{d}y & \text{if Pe} \notin (-2,2) \end{cases}, \tag{5.26c}$$

$$g_1^k = \sum_{i=2}^{n_x-1}\frac{u_y}{2}(c_{i+1,y}^k - c_{i-1,y}^k) + \frac{u_y}{2}\left[c_{2,y}^k + \frac{(-\varphi_{1/2} + u_y/2)c_{1,y}^k + q_W^k}{\varphi_{1/2} + u_y/2}\right]$$

$$+ \frac{u_y}{2}\left[\frac{q_E^k - (\varphi_{n_x+1/2} + u_y/2)c_{n_x,y}^k}{-\varphi_{n_x+1/2} + u_y/2} - c_{n_x-1,y}^k\right], \tag{5.26d}$$

$$g_2^k = \sum_{j=2}^{n_x-1}\left[\xi_y(c_{i,y}^k - c_{i+1,y}^k) + \eta_y(c_{i,y}^k - c_{i-1,y}^k)\right] + \xi_y(c_{1,y}^k - c_{2,y}^k)$$

$$+ \eta_y(c_{n_x,y}^k - c_{n_x-1,y}^k) - \frac{u_y c_{1,y}^k + q_W^k}{\varphi_{1/2} + \eta_y} - \frac{q_E^k - u_y c_{n_x,y}^k}{\varphi_{n_x+1/2} + \eta_y}, \tag{5.26e}$$

where Pe $= u/d$, $u_y = u(y)$, $\xi_y = \max(-u_y, 0)$, $\eta_y = \max(u_y, 0)$; $\varphi_s = d_s/\mathcal{A}_s$ ($s = 1/2$ and $s = n_x + 1/2$); $d_{i+1/2} = \mathscr{D}\mathcal{A}_{i+1/2}/\Delta x_{i+1/2}$; $d_{i-1/2} = \mathscr{D}\mathcal{A}_{i-1/2}/\Delta x_{i-1/2}$ and $\mathcal{A}_{i+1/2}$ and $\mathcal{A}_{i-1/2}$ are the lengths of the eastern and western boundaries of the CV centered at x_i, respectively; q_W and q_E are the unknown fluxes at the western and eastern internal boundaries separating pore- and continuum-scale representations. We stress that $RHS_{I^\star}$ is a function of pore-scale concentration and that the latter depends on q_W and q_E. An iterative algorithm to solve (5.24)–(5.26) is described below.

5.2.2 Hybrid algorithm

The solution of the nonlinear coupled system (5.16)–(5.20) or its discretized form (5.24)–(5.26) reduces to finding zeros (q_E, q_W) of an algebraic system of equations in the form

$$F(q_E, q_W) = 0, \qquad G(q_E, q_W) = 0, \tag{5.27}$$

where $q_E = q_{I^\star+1/2}$ and $q_W = q_{I^\star-1/2}$ are the unknown fluxes at the boundaries of Ω_p. The hybrid pore-scale / continuum-scale algorithm can be formulated as follows.

1. *Initialization.* At timestep T^N, c^N and $\bar{c}^N$ are known.

2. *Guess for fluxes.* Make a guess for q_W and q_E. This imposes the Robin conditions at the eastern and western boundaries of the porous domain,

$$\mathscr{D}\frac{\partial c}{\partial x} - uc = q_W, \qquad x = X_{I^\star-1/2}, \quad y \in [-H, H], \tag{5.28a}$$

$$-\mathscr{D}\frac{\partial c}{\partial x} + uc = q_E, \qquad x = X_{I^\star+1/2}, \quad y \in [-H, H]. \tag{5.28b}$$

The boundary conditions at the north and south boundaries (solid walls of the fracture) are defined by (5.16b).

3. *Pore-scale evolution and source-term evaluation.* The pore-scale problem (5.16), supplemented with the boundary conditions (5.28) is evolved from T^N to T^{N+1}. The source term G at node $I^\star$ is evaluated from (5.26c)–(5.26e).

4. *Continuum-scale evolution.* The continuum-scale concentration $\bar{c}$ is evolved from T^N to T^{N+1} by using the Thomas algorithm to solve the tri-diagonal system (5.24).

5. *Continuum-scale fluxes computation.* Continuum-scale fluxes $\tilde{q}_W$ and $\tilde{q}_E$ at locations $X_{I^\star-1/2}$ and $X_{I^\star+1/2}$ are computed by means of (C.2) and compared with the q_W and q_E computed at step 2.

6. *Convergence check and iteration.* Select an acceptable tolerance ϵ. If $|\tilde{q}_W - q_W| > \epsilon$ or $|\tilde{q}_E - q_E| > \epsilon$, use, e.g., the Broyden method, to refine the guess of q_W and q_E and go to step 2. If both $|\tilde{q}_W - q_W| \le \epsilon$ and $|\tilde{q}_E - q_E| \le \epsilon$, then the convergence is reached. March forward in time ($N := N + 1$) and go to step 1.

5.3 Numerical results

In section 5.3.1, we use advective-diffusive transport in a fracture with uniform reaction rates. This setting admits an analytical solution and, hence, is used to analyze the accuracy of the hybrid algorithm relative to that of its continuum (upscaled) counterpart. In section 5.3.2, the reaction coefficient is taken to be highly heterogeneous. For this situation, we compare the hybrid solution with both a solution of the upscaled equation (5.18) and an averaged solution of the fully two-dimensional problem ("pore-scale simulations").

5.3.1 Hybrid validation

We consider the macroscopic problem (5.18) subject to the initial and boundary conditions

$$\bar{c}(x,0) = 1, \qquad \bar{c}(0,t) = 0, \qquad \frac{\partial \bar{c}}{\partial x}(\infty, t) = 0. \tag{5.29}$$

Its unique solution is

$$\bar{c}(x,t) = \mathrm{e}^{-Kt}\left(1 - \frac{1}{\sqrt{\pi}}\mathrm{e}^{Ux/D}\int\limits_{\frac{x+Ut}{2\sqrt{Dt}}}^{+\infty} \mathrm{e}^{-\eta^2}\,\mathrm{d}\eta + \frac{1}{\sqrt{\pi}}\int\limits_{\frac{x-Ut}{2\sqrt{Dt}}}^{+\infty} \mathrm{e}^{-\eta^2}\,\mathrm{d}\eta\right). \tag{5.30}$$

This exact solution is used to verify the accuracy of both the hybrid solution and the numerical solution of the continuum problem (5.18) for advective-diffusive transport (Fig. 5.3) and advective-diffusive-reactive transport with uniform reaction rates

(Figs. 5.4–5.6) . The set of parameters used for these simulation are summarized in Table 5.1. These values are typical for flow and transport processes through fractured media: experiments of transport in fractured media [93, 94] with fracture aperture in the order of microns $(0.6 - 120\mu\text{m})$ and weighted average velocity of 0.75 m/day have Péclet number in the range of $2.6 \cdot 10^{-3} - 0.52$.

Table 5.1: Parameter values used to validate hybrid algorithm for advection-diffusion-reaction equation. The dimensionless parameters are defined as $\text{Pe} = UL/D$, $\text{Pe}_y = u_m H/\mathscr{D}$, $\text{Da} = KL/D$, $\text{Da}_y = \mathscr{K}H/\mathscr{D}$, $\text{Da}_{out} = K_{out}L/D$, $\text{Da}_{y,out} = \mathscr{K}_{out}H/\mathscr{D}$.

Parameters	Continuum-scale	Pore-scale
Domain length in x	$L = 20$ $[L]$	$\Delta X = 0.25$ $[L]$
Domain length in y	$-$	$2H = 0.25$ $[L]$
Nodes in x-direction	$N_X = 80$	$n_x = 30$
Nodes in y-direction	$-$	$n_x = 20$ $[-]$
Hybrid node	$I^\star = 15$	$-$
Time step	$\Delta T = 0.0005$ $[T]$	$\Delta t = 0.00001$ $[T]$
Diffusion coefficient	$D = 20.0015$ $[L^2/T]$	$\mathscr{D} = 20$ $[L^2/T]$
Kinematic viscosity	$-$	$\nu = 0.01$ $[L^2/T]$
Case 1: Advection-diffusion		
Time domain	$[0, 0.4]$ $[T]$	$[0, 0.4]$ $[T]$
Maximum velocity	$U = 3.33$ $[L/T]$	$u_m = 5$ $[L/T]$
Reaction coefficient	$K = 0$ $[1/T]$	$\mathscr{K} = 0$ $[L/T]$
Péclet number	$\text{Pe} \approx 10$	$\text{Pe}_y \approx 0.03$
Damköhler number	$\text{Da} = 0$	$\text{Da}_y = 0$
Case 2: Advection-diffusion-reaction (homogeneous $\mathscr{K}$)		
Time domain	$[0, 0.2]$ $[T]$	$[0, 0.2]$ $[T]$
Maximum velocity	$U = 10.0417$ $[L/T]$	$u_m = 15$ $[L/T]$
Reaction coefficient	$K = 39.5833$ $[1/T]$	$\mathscr{K} = 5$ $[L/T]$
Péclet number	$\text{Pe} \approx 5$	$\text{Pe}_y \approx 0.1$
Damköhler number	$\text{Da} \approx 40$	$\text{Da}_y \approx 0.03$
Case 3: Advection-diffusion-reaction (heterogeneous $\mathscr{K}$)		
Time domain	$[0, 0.25]$ $[T]$	$[0, 0.25]$ $[T]$
Maximum velocity	$U = 0$ $[L/T]$	$u_m = 0$ $[L/T]$
Reaction coefficient	$K_{out} = 0.8$ $[1/T]$	$\mathscr{K}_{out} = 0.1$ $[L/T]$
	$K_{in} = 478$ $[1/T]$	$\mathscr{K}_{in} = 410$ $[L/T]$
Péclet number	$\text{Pe} = 0$	$\text{Pe}_y = 0$
Damköhler number	$\text{Da}_{out} \approx 0.8$	$\text{Da}_{y,out} = 6.25 \cdot 10^{-4}$
	$\text{Da} \approx 478$	$\text{Da}_y = 2.56$

Figures 5.3–5.5 show a perfect agreement between analytical and hybrid solution. This is to be expected since all the necessary conditions for the validity of the macroscopic

(averaged) transport equation (5.18) hold for the flow and transport regimes considered in Cases 1 and 2. The comparison between the numerical and analytical solutions of (5.18) also demonstrates that the choice of space-time discretization is adequate to ensure the required accuracy. It helps to ensure that the discrepancy between hybrid (and pore-scale) and continuum simulations observed in section 5.3.2 is due to the breakdown of the latter rather than numerical errors.

Figure 5.6 depicts pore-scale concentration distribution at the macro-scale node $I^\star$ at four different temporal snapshots. The accumulation and depletion areas close to the boundaries are a consequence of assuming a parabolic profile for velocity everywhere in the pore-scale domain. The assumption of fully-developed flow represents an approximation that is not necessary for the hybrid algorithm but, at this stage, significantly simplifies the numerical treatment of the problem while still being able to capture key features of the transport phenomena. In reality, entrance effects in a laminar flow regime are not negligible in an inlet (and outlet) region whose *entrance length*, L_e, is the distance between the inlet (or outlet) and the location where the flow field is fully developed. L_e can be determined from an empirical relation

$$\frac{L_e}{2H} = 0.06 \text{Re}_p, \tag{5.31}$$

where ν is the kinematic viscosity $[L^2/T]$ and $\text{Re}_p = 2Hu_m/\nu$ is pore-scale Reynolds number. Re_p can be related to $\text{Re}_c = 2HU/\nu$ by

$$\text{Re}_c = \left(\frac{2}{3} + \frac{4}{45}\text{Da}_y\right)\text{Re}_p. \tag{5.32}$$

A bound on L_e places a constraint on the size of the pore-scale simulations domain, ΔX, e.g.,

$$L_e < \Delta X/10, \tag{5.33}$$

which requires that the sum of the entrance and exit regions should be significantly smaller than ΔX. Combining (5.33) with (5.5), and recognizing that $\text{Pe}_y = \nu \text{Re}_p/2\mathscr{D}$, we obtain

$$\text{Pe}_y < \frac{5\nu}{\mathscr{D}} \min\left\{\frac{5}{3}\frac{\Delta X}{H}, 3\left(1 + \frac{2}{15}\text{Da}_y\right)^{-1}\right\}. \tag{5.34}$$

This bound on Pe_y guarantees that Darcy's law holds true in the whole computational domain while the inlet and outlet effects are confined to a limited region close to the boundaries of the pore-scale simulations domain.

Figure 5.6 shows that even when the bound (5.34) is not satisfied and entrance effects become non-negligible at the pore-scale, the average concentration is still well captured (Fig. 5.4 and 5.5). Solution of flow problem with inlet and outlet boundary conditions for porous media with complex (and more realistic) geometry will be addressed in future research.
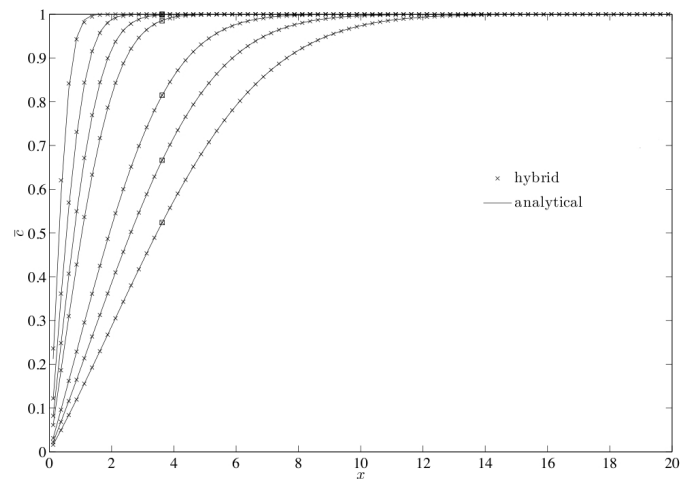
Figure 5.3: Temporal snapshots of the average concentration $\bar{c}$ obtained analytically by (5.30) (solid line) and from hybrid simulation ($\times$) at times $t = 0.005$, $t = 0.015$, $t = 0.03$, $t = 0.05$, $t = 0.15$, $t = 0.25$, and $t = 0.395$ (from left to right). Symbol $\square$ indicates the location where pore- and continuum-scales are coupled (i.e. node $I^\star$). Case 1 of Table 5.1.

5.3.2 Hybrid simulations for highly localized heterogeneous reaction

In the last example we investigate the effects heterogenous reaction coefficient. Specifically we assume $\mathscr{K}$ at the $I^\star$-th node to be four orders of magnitude bigger than in the rest of the channel, with a typical Damköhler number ranging from $6.25 \cdot 10^{-4}$ to 2.56. Equation (5.18) fails for $\mathrm{Da}_y \geq 3$ as the effective reaction coefficient K changes sign for increasing positive values of $\mathscr{K}$ (i.e., increasing mass loss at the solid-liquid interface):
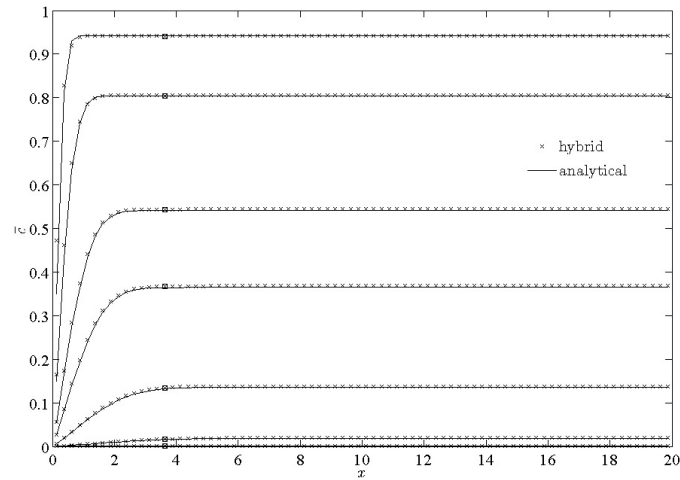
Figure 5.4: Temporal snapshots of the average concentration $\bar{c}$ obtained analytically by (5.30) (solid line) and from hybrid simulation ($\times$) at times $t = 0.001$, $t = 0.005$, $t = 0.015$, $t = 0.025$, $t = 0.05$, $t = 0.1$, and $t = 0.195$ (from top to bottom). Symbol $\square$ indicates the location where pore- and continuum-scales are coupled (i.e. node $I^\star$). Case 2 of Table 5.1.

Figure 5.5: Breakthrough curves at three different locations (upstream and downstream of the hybrid node (figures on the left and on the right, respectively) and at the hybrid location (center) obtained analytically by (5.30) (solid line), from hybrid simulation ($\times$), and the numerical solution of the continuum model (5.18) (dashed line). Case 2 of Table 5.1.
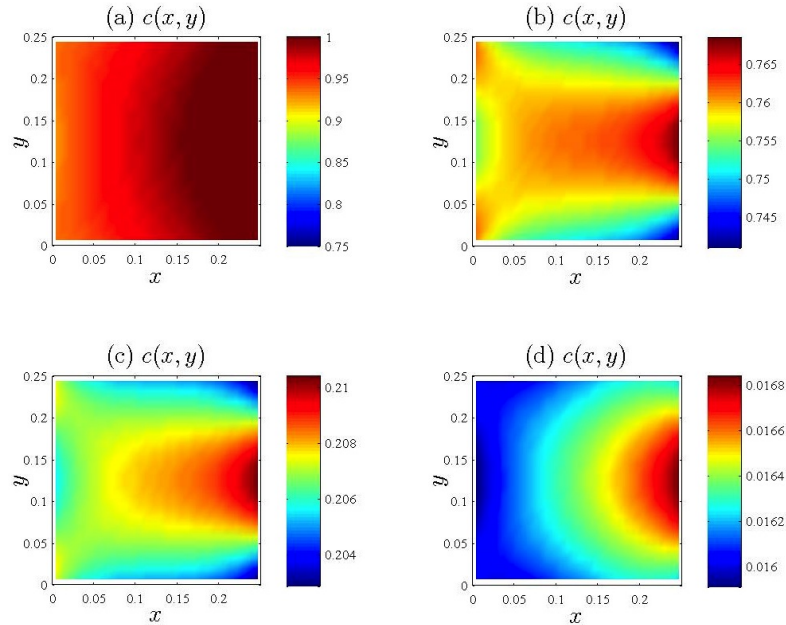
Figure 5.6: Pore-sale concentration distribution at macro-scale node $I^\star$ at times $t = 0.0005$ (a), $t = 0.007$ (b), $t = 0.04$ (c), and $t = 0.1$ (d). Case 2 of Table 5.1.

this leads to the unphysical behavior of $K < 0$ (i.e., source) while mass is absorbed (degraded, etc) at the micro-scale (i.e., sink). While it is clear that differences between the upscaled model (5.18) and a fully 2D pore-scale solution will be more dramatic for Da ≥ 3, we show here that significant deviations from the "pore-scale" solution occur even for Da < 3. This is done by comparing the results of our hybrid simulations with that of the upscaled 1D equation and the average of the fully 2D solution.

Figures 5.7 and 5.8 show the continuum-scale concentration and breakthrough curves at node $I^\star$ obtained from the upscaled 1D continuum-scale, hybrid and fully 2D pore-scale equations. At the location of high heterogeneity, the continuum-scale equation overestimates the concentration, with values that double the true concentration obtained from the pore-scale simulations. On the contrary, the hybrid simulation significantly improves the predictions.

Figure 5.9 depicts the concentration profile at the pore-scale at two different times and shows how the highly reacting walls produce strong concentration gradients between areas where mass is more quickly depleted because of fast reactions (close to
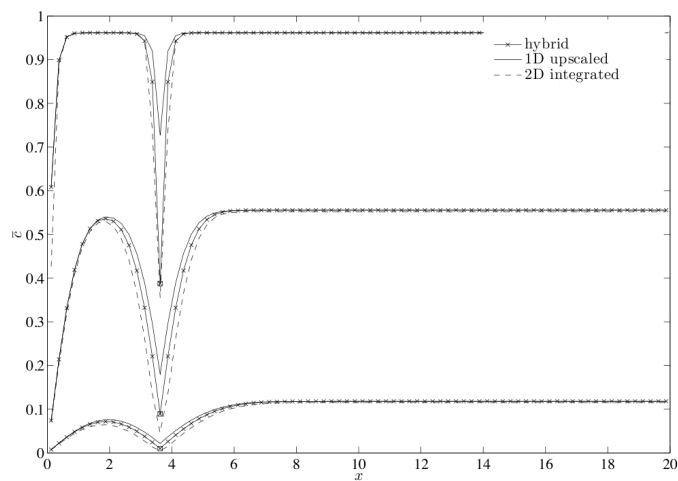
Figure 5.7: Profile of the average concentration $\bar{c}$ obtained by 1D upscaled equation (solid line), from hybrid $(-\times-)$ and fully 2D pore-scale (dashed line) simulations at times $t = 0.0005$ (top), $t = 0.015$ (center) and $t = 0.055$ (bottom). Symbol $\square$ indicates the location where pore- and continuum-scales are coupled (i.e. node $I^\star$). Case 3 of Table 5.1.

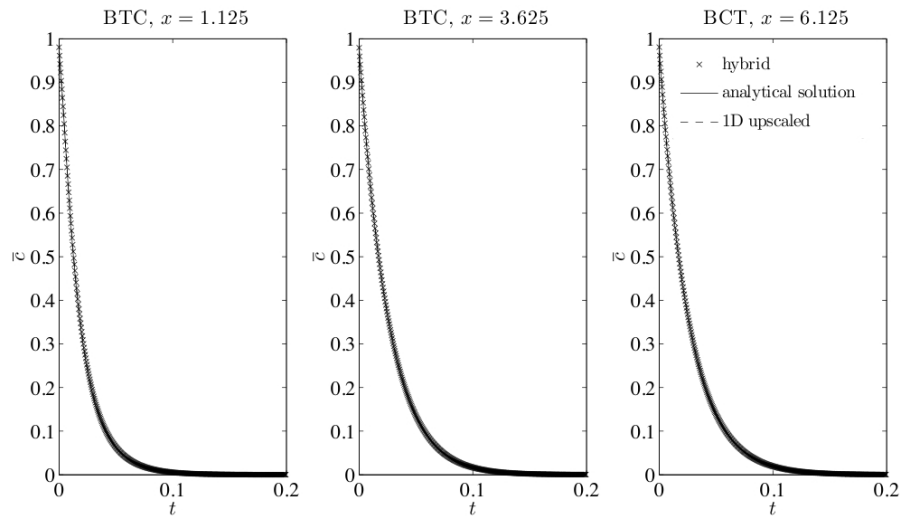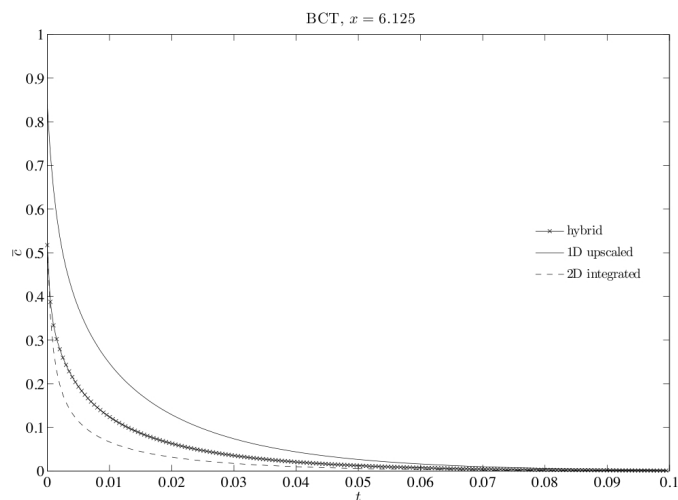Figure 5.8: Breakthrough curves at the hrybrid node location obtained from numerical solution of 1D upscaled equation (5.30) (solid line), hybrid simulation $(-\times-)$, and the fully 2D problem (dashed line). Case 3 of Table 5.1.

the walls) relative to others where the major transport mechanism is diffusion (in the center of the channel).
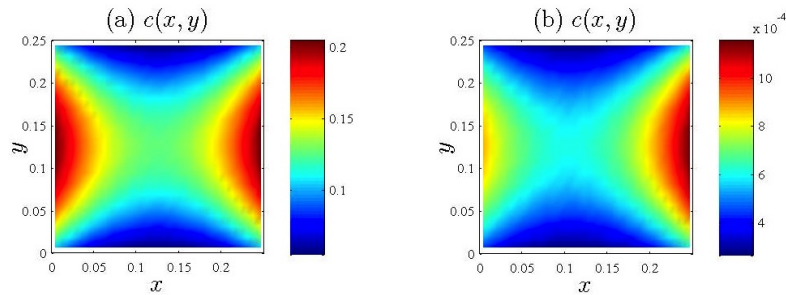
Figure 5.9: Pore-scale concentration profile c at macro-scale node $I^\star$ obtained from hybrid simulations at times $t = 0.004$ (a) and $t = 0.1$ (b). Case 3 of Table 5.1.

5.4 Summary and conclusions

We developed a general algorithm to incorporate pore-scale (subgrid) effects into continuum (coarse-grid) models of reactive transport in porous and fractured media. Unlike other multiscale methods, which are based on empirical closure and/or approximations, our approach employs a formulation that does not require any assumptions on the macroscopic behavior of pore-scale variables. This is attained by treating the normal fluxes through the internal boundaries separating the two formulations as unknown quantities. Given the intrinsic nonlinearity of such a formulation, the solution is found through an iterative procedure.

We applied our algorithm to model Taylor dispersion in a fracture with chemically reactive walls. A finite volume solution of the hybrid formulation was compared with its analytical counterpart, when available, and/or with "pore-scale" simulations of two-dimensional transport inside the fracture.

Our study leads to the following major conclusions:

- The proposed hybrid algorithm enables one to determine pore- and continuum-scale concentration and fluxes exchanged at their internal boundary without any approximation and/or hypothesis.

- The hybrid formulation does not require additional parameters besides continuum properties of the porous media, properties of the solute and fluid and pore-scale geometry.

- The hybrid model formulation reduces to a zero-finding algorithm for a vector function. Such a formulation suggests its high adaptability to a wide variety of problems and different numerical schemes.

- Although not pursued here, the general hybrid formulation presented in section 5.1.3 is suitable for implementation in commercial numerical codes.

- The proposed method is capable of handling highly localized heterogeneities, which provides a considerable improvement in accuracy and enables one to properly capture the pore-scale physics.

In the next Chapter we propose a hybrid algorithm that does not require overlap between pore- and continuum-scale models.

Battiato, I., Tartakovsky, D. M., Tartakovsky, A. M., Scheibe, T.D., (2010),'Hybrid Simulations of Reactive Transport in Fractures'. Adv. Water Resour., Special Issue, Submission code: AWR-10-234.

Chapter 6

Nonintrusive Hybridization

6.1 Introduction

In the previous Chapter we developed an intrusive hybrid algorithm that requires the modification of some of the coefficients of the system of discretized equations. While not limited to systems with simple geometry, the application of the algorithm is greatly simplified in those situations. Even though its formulation is quite general and can be applied to a variety of different numerical schemes, its implementation in legacy codes, in which discretized equations cannot be easily modified by the user, is challenging. Complex pore geometries introduce another complication.

Hence, a desirable feature of a hybrid algorithm is its portability and implementation in existing codes. This can be accomplished by eliminating the overlapping ("handshake") region and formulating appropriate conditions at the interfaces separating the two computational subdomains, while ensuring the continuity of state variables and fluxes. Within this framework, pore-scale simulations affect a continuum-scale solution through boundary conditions (and not as a modification of continuum-scale discretized equations): this will facilitate hybrid implementation for existing codes and/or software.

6.2 Advection-diffusion equations

Consider advective-diffusive transport in a fully saturated porous medium Ω^T. Within the pore space $\Omega^T_{pore} \subset \Omega^T$, single-phase flow of an incompressible fluid is described by the Stokes and continuity equations (5.1). Flow equations are subject to the no-slip boundary condition on the solid-liquid interface $A^T_{s\ell}$, which is taken to be impermeable to flow. The flow is driven by boundary conditions imposed on $\partial \Omega^T$, the external boundary of Ω^T. The fluid contains a dissolved species with molar concentration $c(\mathbf{x}, t)$ that is advected and diffused in the system.

6.2.1 Governing equations at the pore-scale

The evolution of the concentration $c(\mathbf{x}, t)$ of a tracer undergoing advection and diffusion is described by

$$\frac{\partial c}{\partial t} + \nabla \cdot (\mathbf{v}c) = \mathscr{D}\nabla^2 c, \tag{6.1}$$

subject to a no-flux boundary condition on the solid-fluid interface $A^T_{s\ell}$

$$-\mathbf{n} \cdot \mathscr{D}\nabla c = 0, \tag{6.2}$$

and proper boundary conditions on $\partial \Omega^T$.

6.2.2 Governing equations at the continuum scale

Let $\overline{A}(\mathbf{x}, t)$ denote the spatial average of a pore-scale quantity $A(\mathbf{x}, t)$ defined as in (5.3). Then, as discussed in section 5.1.2, the spatial averaging of (6.1) leads to an upscaled equation

$$\phi\frac{\partial \overline{c}}{\partial t} + \phi\nabla \cdot (\mathbf{V}\overline{c}) = \nabla \cdot (\mathbf{D}^*\nabla\overline{c}), \tag{6.3}$$

where $\mathbf{V}$ is the average macroscopic velocity and $\mathbf{D}^*$ is the dispersion coefficient.

6.2.3 Derivation of coupling boundary conditions

We are concerned with transport regimes in which the validity of the continuum-scale transport equation (6.3) breaks down in a subdomain $\Omega_p \subset \Omega^T_{pore}$ with boundary
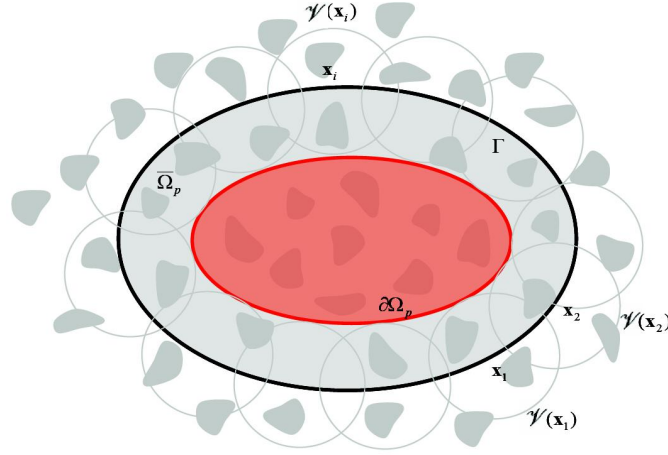
Figure 6.1: A schematic representation of the pore- and continuum-scale domains. The subdomain where continuum-scale representation breaks down is depicted in red. Its boundary is $\partial\Omega_p$. The boundary Γ is constructed as the locus of the centers of the family of averaging volumes $\mathscr{V}(\mathbf{x})$ whose envelope is $\partial\Omega_p$.

$\partial\Omega_p$ of the computational domain Ω. We define Γ to be the locus of the centers of the family of the averaging volumes $\mathscr{V}(\mathbf{x})$, whose envelope is $\partial\Omega_p$ as shown in Fig. 6.1. We denote $\overline{\Omega}_p$ the domain bounded by Γ. Let $A_{s\ell} = \overline{\Omega}_p \cap A_{s\ell}^T$.

Let $\overline{c}^{\leftarrow}$ denote the limiting value of $\overline{c}(\mathbf{x})$ as $\mathbf{x} \to \mathbf{x}^{\leftarrow} \in \Gamma$ from the *exterior* of $\overline{\Omega}_p$, and $\overline{c}^{\rightarrow} = \overline{c}(\mathbf{x}^{\rightarrow})$ as $\mathbf{x} \to \mathbf{x}^{\rightarrow} \in \Gamma$ from the *interior* of $\overline{\Omega}_p$. Since average concentration is a continuous function everywhere in Ω, it is continuous across Γ

$$\overline{c}^{\leftarrow} = \overline{c}^{\rightarrow} \quad \text{for} \quad |\mathbf{x}^{\rightarrow} - \mathbf{x}^{\leftarrow}| \to 0. \tag{6.4}$$

Let $\mathscr{V}^{in}(\mathbf{x}) := \mathscr{V}(\mathbf{x}) \cap \overline{\Omega}_p$ and $\mathscr{V}^{out}(\mathbf{x}) := \mathscr{V}(\mathbf{x}) \setminus \mathscr{V}^{in}(\mathbf{x})$ to form a partition of $\mathscr{V}$ where pore-scale is explicitly resolved and where only a continuum-scale representation exists, respectively (see Fig. 6.2). Then (6.4) can be written as

$$\overline{c}^{\leftarrow} = \frac{1}{\phi||\mathscr{V}||} \int_{\mathscr{V}^{in}(\mathbf{x}^{\rightarrow})} c(\mathbf{y})\,\mathrm{d}\mathbf{y} + \frac{1}{\phi||\mathscr{V}||} \int_{\mathscr{V}^{out}(\mathbf{x}^{\rightarrow})} c(\mathbf{y})\,\mathrm{d}\mathbf{y}. \tag{6.5}$$

Expanding $c(\mathbf{y})$ into a Taylor series around the centroid $\mathbf{x}$ and retaining the leading term yields

$$\int_{\mathscr{V}^{out}(\mathbf{x}^{\rightarrow})} c\,\mathrm{d}\mathbf{y} \approx ||\mathscr{V}^{out}(\mathbf{x}^{\rightarrow})||c^{\rightarrow}(\mathbf{x}^{\rightarrow}). \tag{6.6}$$

Inserting (6.6) into (6.5), we obtain

$$\overline{c}^{\leftarrow} = \frac{1}{\phi||\mathscr{V}||} \int_{\mathscr{V}^{in}(\mathbf{x}^{\rightarrow})} c(\mathbf{y})\, \mathrm{d}\mathbf{y} + \frac{||\mathscr{V}^{out}(\mathbf{x}^{\rightarrow})||}{\phi||\mathscr{V}||} c^{\rightarrow}. \tag{6.7}$$

To establish a flux continuity condition across Γ, we first derive an average equation that is valid everywhere in Ω. The volume averaging of the pore-scale equation (6.1) yields

$$\phi\frac{\partial \overline{c}}{\partial t} + \phi\overline{\nabla \cdot (-\mathscr{D}\nabla c + \mathbf{v}c)} = 0. \tag{6.8}$$

Invoking the spatial averaging theorem, and accounting for the no-slip and no-flux boundary conditions on the solid-liquid interface $A_{s\ell}$, leads to

$$\phi\frac{\partial \overline{c}}{\partial t} + \phi\nabla \cdot \overline{(-\mathscr{D}\nabla c + \mathbf{v}c)} = 0. \tag{6.9}$$

Integrating (6.9) over an arbitrary volume $\mathscr{I}$ containing the interface Γ, we obtain

$$\phi\frac{\partial}{\partial t} \int_{\mathscr{I}} \overline{c}\mathrm{d}\mathbf{y} = -\phi \int_{\mathscr{I}_{in}} \nabla \cdot \overline{(-\mathscr{D}\nabla c + \mathbf{v}c)}\mathrm{d}\mathbf{y} - \phi \int_{\mathscr{I}_{out}} \nabla \cdot \overline{(-\mathscr{D}\nabla c + \mathbf{v}c)}\mathrm{d}\mathbf{y}, \tag{6.10}$$

where $\mathscr{I}_{in}$ and $\mathscr{I}_{out}$ form a partition of $\mathscr{I}$, such that $\mathscr{I}_{in} \cup \mathscr{I}_{out} = \mathscr{I}$ (see Fig. 6.3). In $\mathscr{I}_{out}$, the upscaled model (6.3) holds, so that

$$\phi\frac{\partial}{\partial t} \int_{\mathscr{I}} \overline{c}\mathrm{d}\mathbf{y} = -\phi \int_{\mathscr{I}_{in}} \nabla \cdot \overline{(-\mathscr{D}\nabla c + \mathbf{v}c)}\mathrm{d}\mathbf{y} - \int_{\mathscr{I}_{out}} \nabla \cdot (\phi\mathbf{V}\overline{c} - \mathbf{D}^*\nabla\overline{c})\mathrm{d}\mathbf{y}. \tag{6.11}$$

This gives

$$\phi\frac{\partial}{\partial t} \int_{\mathscr{I}} \overline{c}\mathrm{d}\mathbf{y} = -\phi \int_{\Gamma_{in}} \mathbf{n} \cdot \overline{(-\mathscr{D}\nabla c + \mathbf{v}c)}\mathrm{d}\mathbf{y} - \phi \int_{\Gamma} \mathbf{n} \cdot \overline{(-\mathscr{D}\nabla c + \mathbf{v}c)}\mathrm{d}\mathbf{y}$$
$$- \int_{\Gamma_{out}} \mathbf{n} \cdot (\phi\mathbf{V}\overline{c} - \mathbf{D}^*\nabla\overline{c})\mathrm{d}\mathbf{y} + \int_{\Gamma} \mathbf{n} \cdot (\phi\mathbf{V}\overline{c} - \mathbf{D}^*\nabla\overline{c})\mathrm{d}\mathbf{y}. \tag{6.12}$$

Mass conservation requires that

$$-\phi \int_{\Gamma} \mathbf{n} \cdot \overline{(-\mathscr{D}\nabla c + \mathbf{v}c)}\mathrm{d}\mathbf{y} + \int_{\Gamma} \mathbf{n} \cdot (\phi\mathbf{V}\overline{c} - \mathbf{D}^*\nabla\overline{c})\mathrm{d}\mathbf{y} = 0, \tag{6.13}$$

which yields the second condition on the interface Γ,

$$\mathbf{n} \cdot (-\mathbf{D}^*\nabla\overline{c}^{\leftarrow} + \phi\mathbf{V}\overline{c}^{\leftarrow}) = \mathbf{n} \cdot \phi\overline{(-\mathscr{D}\nabla c + \mathbf{v}c)}^{\rightarrow}, \tag{6.14}$$

where the superscripts $\leftarrow$ and $\rightarrow$ denote the respective limits from the exterior and interior.

It remains to express the right hand side of (6.14) in terms of pore-scale concentration. The average $\overline{(-\mathscr{D}\nabla c + \mathbf{v}c)}$ at point $\mathbf{x}$ is defined as

$$\overline{(-\mathscr{D}\nabla c + \mathbf{v}c)}(\mathbf{x}) = \frac{1}{\phi\|\mathscr{V}\|}\int_{\mathscr{V}(\mathbf{x})}[-\mathscr{D}\nabla c(\mathbf{y}, t) + \mathbf{v}(\mathbf{y}, t)c(\mathbf{y}, t)]\mathrm{d}\mathbf{y}. \qquad (6.15)$$

Therefore

$$\mathbf{n}\cdot(\mathbf{D}^*\nabla\bar{c}^{\leftarrow} - \phi\mathbf{V}\bar{c}^{\leftarrow}) = \frac{1}{\|\mathscr{V}\|}\mathbf{n}\cdot\int_{\mathscr{V}^{in}(\mathbf{x}^{\rightarrow})}(-\mathscr{D}\nabla c + \mathbf{v}c)\mathrm{d}\mathbf{y} + q_n, \qquad (6.16)$$

where

$$q_n(\mathbf{x}) := \frac{1}{\|\mathscr{V}\|}\mathbf{n}\cdot\int_{\mathscr{V}^{out}(\mathbf{x})}(-\mathscr{D}\nabla c + \mathbf{v}c)\mathrm{d}\mathbf{y} \qquad (6.17)$$

is an unknown flux through Γ. This flux serves as a coupling condition at the interface
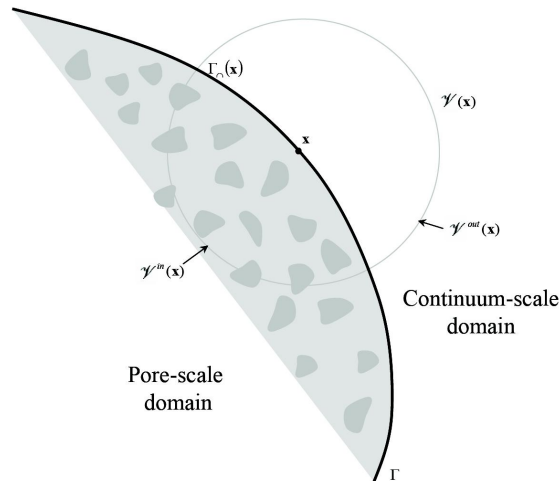
Figure 6.2: A schematic representation of the averaging procedure across the boundary separating pore- and continuum-scale representations. On the left of Γ pore-scale is fully resolved while on the right only a continuum-scale representation exists.

between pore- and continuum-scale subdomains.

The final form of the nonlinear coupled system of equations for the hybrid algo-
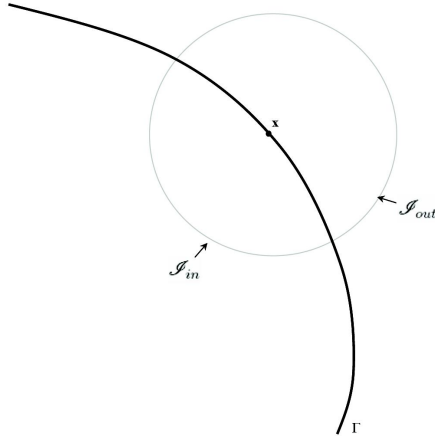
Figure 6.3: A schematic representation of the averaging procedure across Γ.

rithm is

$$\phi\frac{\partial\bar{c}}{\partial t} + \phi\nabla\cdot(\mathbf{V}\bar{c}) = \nabla\cdot(\mathbf{D}^*\nabla\bar{c}), \qquad \mathbf{x}\in\Omega\setminus\overline{\Omega}_p, \tag{6.18}$$

$$\frac{\partial c}{\partial t} + \nabla\cdot(\mathbf{v}c) = \mathscr{D}\nabla^2 c, \qquad \mathbf{x}\in\overline{\Omega}_p, \tag{6.19}$$

$$-\mathbf{n}\cdot\mathscr{D}\nabla c = 0, \qquad \mathbf{x}\in A_{s\ell}, \tag{6.20}$$

$$\mathbf{n}\cdot(-\mathscr{D}\nabla c + \mathbf{v}c) = q_n, \qquad \mathbf{x}\in\Gamma \tag{6.21}$$

$$\bar{c}^{\leftarrow} = \frac{1}{\phi||\mathscr{V}||}\int_{\mathscr{V}^{in}(\mathbf{x})} c\,\mathrm{d}\mathbf{y} + \frac{||\mathscr{V}^{out}||}{\phi||\mathscr{V}||}c^{\rightarrow}, \qquad \mathbf{x}\in\Gamma, \tag{6.22}$$

$$\mathbf{n}\cdot(\mathbf{D}^*\nabla\bar{c}^{\leftarrow} - \phi\mathbf{V}\bar{c}^{\leftarrow}) = q_n + \frac{1}{||\mathscr{V}||}\mathbf{n}\cdot\int_{\mathscr{V}^{in}(\mathbf{x}^{\rightarrow})}(-\mathscr{D}\nabla c + \mathbf{v}c)\,\mathrm{d}\mathbf{y}, \quad \mathbf{x}\in\Gamma. \tag{6.23}$$

The interfacial conditions (6.22) and (6.23) are reminiscent of the macroscopic Dirichlet and Neumann boundary conditions derived by the method of volume averaging in [95]. While similar in spirit, our conditions do not require a closure approximation, relying on pore-scale simulations instead.

Coupling conditions for Taylor dispersion problem are derived as a special case of our more general formulation in the following paragraph.

6.2.4 Taylor dispersion between parallel plates:
$$\mathcal{V} \cap \overline{\Omega}_p = \emptyset$$

Whenever the average of a pore-scale variable $\xi(\mathbf{x})$ with $\mathbf{x} = (x_1, x_2, x_3) \in \Omega_1 \times \Omega_2 \times \Omega_3$ is defined by integrating one of the independent variables x_i over Ω_i, $i = 1, 2, 3$, the dimensionality of the correspondent continuum-scale equation is reduced. An example is the problem of Taylor dispersion between two infinite parallel plates where $\Omega_1 = (-\infty, +\infty)$, $\Omega_2 = (-H, H)$, with $2H$ the distance between the plates and the average of a generic pore-scale variable defined as

$$\xi(x) = \frac{1}{2H} \int_{-H}^{H} \xi(x, y) \mathrm{d}y. \qquad (6.24)$$

This allows one to derive a one-dimensional effective equation starting from a two-dimensional pore-scale problem. In such situation, $\mathcal{V} = \mathcal{V}^{out}$ and $\mathcal{V}^{in} = \emptyset$. The boundary Γ reduces to a point and to a vertical segment of length $2H$ on the continuum- and pore-scale subdomains, respectively. The generalized coupling conditions for state variables and fluxes at the boundary Γ extablished by equations (6.22) and (6.23) simplify to the following conditions

$$\bar{c}^{\leftarrow} = c^{\rightarrow}, \qquad\qquad\qquad \mathbf{x} \in \Gamma, \qquad (6.25)$$

$$\mathbf{n} \cdot (\mathbf{D}^* \nabla \bar{c}^{\leftarrow} - \phi \mathbf{V} \bar{c}^{\leftarrow}) = q_n, \qquad\qquad \mathbf{x} \in \Gamma, \qquad (6.26)$$

given $\phi = 1$. The previous conditions establish that pore-scale concentration and flux are constant along the boundary and equal the continuum-scale value on the boundary exterior.

In the following section we propose an algorithm to solve the system (6.18)-(6.23).

6.2.5 Hybrid algorithm

The solution of the nonlinear coupled system (6.18)-(6.23) reduces to finding zeros of a system of equations in the form

$$F(q_n, c^{\rightarrow}) = 0, \quad G(q_n, c^{\rightarrow}) = 0, \qquad (6.27)$$

where

$$F(q_n, c^{\rightarrow}) = \mathbf{n} \cdot (\mathbf{D}^* \nabla \bar{c}^{\leftarrow} - \phi \mathbf{V} \bar{c}^{\leftarrow}) - \frac{1}{||\mathscr{V}||} \int\limits_{\mathscr{V}^{in}(\mathbf{x}^{\rightarrow})} \mathbf{n} \cdot (-\mathscr{D}\nabla c + \mathbf{v}c)\mathrm{d}\mathbf{y}$$

$$-\frac{||\Gamma(\mathbf{x}^{\rightarrow})||}{||\mathscr{V}||}q_n, \qquad (6.28)$$

$$G(q_n, c^{\rightarrow}) = \bar{c}^{\leftarrow} - \frac{1}{\phi||\mathscr{V}||} \int\limits_{\mathscr{V}^{in}(\mathbf{x})} c\mathrm{d}\mathbf{y} - \frac{||\mathscr{V}^{out}||}{\phi||\mathscr{V}||}c^{\rightarrow}. \qquad (6.29)$$

The hybrid pore-scale / continuum-scale algorithm can be formulated as follows.

1. *Initialization.* At timestep T^N, $c(t = T^N)$ and $\bar{c}(t = T^N)$ are known.

2. *Guess for flux.* Make a guess for q_n. This imposes the Robin condition (6.21) at interface Γ.

3. *Pore-scale evolution.* The pore-scale equation (6.19), supplemented with boundary condition (6.20), is evolved from T^N to T^{N+1}.

4. *Evaluation of boundary integrals.* The right hand side of (6.29) is evaluated together with the integral term in (6.23). The latter imposes the Robin condition (6.23) at the interface Γ.

5. *Continuum-scale evolution.* The continuum-scale concentration $\bar{c}$ is evolved from T^N to T^{N+1} by (6.18).

6. *Continuum-scale concentration evaluation.* The function G is computed by means of (6.29).

7. *Convergence check and iteration.* For a given tolerance ϵ, if $|G(q_n, c_\Gamma)| > \epsilon$, the Broyden method (or another root-finding algorithm) is used to refine the guess of q_n and go to step 2. If $|G(q_n, c_\Gamma)| \leq \epsilon$, then the convergence is reached. March forward in time ($N := N + 1$) and go to step 1.

Chapter 7

Conclusions

This dissertation leads to the following major conclusions:

1. Continuum-scale descriptions of flow in porous media can be successfully applied to model elastic response of carbon nanotube (CNT) forests to aerodynamic loading. Such models represent mesoscopic structural and dynamics methods which seem to be suitable for describing crowded systems at the nanoscale. Specifically, the treatment of CNTs forests as porous media allowed us to develop closed-form expressions for i) the drag force exerted by laminar and turbulent flows on CNT forests and the corresponding drag coefficient, ii) the bending profile of individual CNTs caused by hydrodynamic loading, and iii) maximum deflection at a CNT's tip. The latter can serve to estimate the Young bending modulus of CNTs. We demonstrated good agreement between our model predictions and experimental data. Such encouraging results suggest possible generalizations to describe i) non-linear bending due to kink development and ii) heat and mass transfer processes in CNT composites through effective models for transport in porous media.

2. While very powerful in describing many processes at a variety of different scales, macroscopic models might breakdown. We established conditions under which macroscopic reaction-diffusion equations (RDEs) provide an adequate averaged description of pore-scale processes. We showed that the range of applicability of macroscopic RDEs and various transport regimes can be described by a phase diagram in a space

spanned by the dimensionless Damköhler number and a scale separation parameter. This was accomplished by upscaling a system of nonlinear diffusion-reaction equations at the pore-scale by means of volume averaging technique. For physical phenomena that do not satisfy such conditions, an upscaled (local) equation does not generally exist and integro-differential (non-local in space and time) alternatives or hybrid models must be used instead.

3. The previous result was generalized by considering macroscopic advection-dispersion-reaction equations (ADREs). The method of multiple-scale expansion was used to upscale to the continuum (Darcy) scale a pore-scale advection-diffusion equation with nonlinear reactions entering through a boundary condition on the fluid-solid interfaces. The range of applicability of macroscopic ADREs can be described with a phase diagram in the (Da,Pe)- space (where Da and Pe are Damköhler and Péclet numbers, respectively). The latter is parametrized with a scale-separation parameter, defined as the ratio of characteristic lengths associated with the pore-and macro-scales. This phase diagram revealed that transport phenomena dominated at the pore-scale by reaction processes do not lend themselves to macroscopic descriptions and effective parameters do not generally exist. These results generalize our previous findings relative to RDEs and suggest that they are universal, i.e., independent of the choice of an upscaling technique.

4. When the validity of continuum-scale models cannot be ascertained a priori in small portions of the computational domain, hybrid models that couple pore- and continuum-scale representations can be used. We developed a general intrusive hybrid algorithm to incorporate pore-scale effects into continuum models of reactive transport in fractured media. This formulation is based on overlapping the pore-and continuum-scale representations and therefore requires the modification of some coefficients in the discretized system of equations. We applied our algorithm to model Taylor dispersion in a planar fracture with chemically reactive walls. Existing analytical solutions served as validation. The hybrid model formulation reduces to a zero-finding algorithm for a vector function: this suggests its high applicability to a wide variety of problems and numerical schemes. The proposed method is capable of

handling highly localized heterogeneities, which provides a considerable improvement in accuracy and enables one to properly capture the pore-scale physics.

5. A desirable feature of a hybrid model is its ability to be easily incorporated into existing (legacy) codes/software. Even though not necessary to this purpose, a formalization that is not intrusive would render such a task much easier. Therefore we developed an alternate formalization for the hybridization that is nonintrusive and a priori does not require mesh refinement on the continuum-scale subdomain to match the mesh dimension on the pore-scale subdomain.

Appendix A

Proofs of Propositions

A.1 Proposition 3.3.1

A detailed derivation of the proof can be found in [8]. It is reproduced here for completeness in order to identify all the relevant constraints.

Applying the averaging theorem (3.10) to $\hat{\nabla}^2 c_3$ twice, while accounting for the boundary condition (3.8), using the decomposition $c_3 = \langle c_3 \rangle_B + \tilde{c}_3$, and keeping the two leading terms in a Taylor expansion of the average concentration $\langle c_3 \rangle_B(\hat{\mathbf{x}} + \hat{\mathbf{y}}_B)$ under the volume integrals, one obtains [8, Eqs. 1.3-8]

$$\langle \hat{\nabla}^2 c_3 \rangle = \hat{\nabla} \cdot \left(\phi \hat{\nabla} \langle c_3 \rangle_B - \hat{\nabla} \langle \hat{\mathbf{y}}_B \rangle \cdot \hat{\nabla} \langle c_3 \rangle_B - \frac{1}{2} \hat{\nabla} \langle \hat{\mathbf{y}}_B \hat{\mathbf{y}}_B \rangle : \hat{\nabla} \hat{\nabla} \langle c_3 \rangle_B \right.$$
$$\left. + \frac{1}{|\mathcal{V}|} \int_{A_{ls}} \tilde{c}_3 \mathbf{n} \mathrm{d}A \right) - a_v \mathrm{Da}_{ls} \frac{\langle c_3 \rangle_{ls} - 1}{l}, \tag{A.1}$$

where

$$\langle c_3 \rangle_{ls} \equiv \frac{1}{|\mathscr{A}_{ls}|} \int_{\mathscr{A}_{ls}} c_3 \mathrm{d}A$$

and $\hat{\nabla} \langle \hat{\mathbf{y}}_B \rangle$ is a second order tensor and $\hat{\nabla} \langle \hat{\mathbf{y}}_B \hat{\mathbf{y}}_B \rangle$ is a third-order tensor.

The first constraint, $r_0 \gg l$, ensures that $\hat{\nabla} \langle \hat{\mathbf{y}}_B \rangle \cdot \hat{\nabla} \langle c_3 \rangle_B$ is much smaller than $\phi \hat{\nabla} \langle c_3 \rangle_B$ and, hence, can be neglected [8, p. 18]. The second constraint, $r_0^2 \ll L_\phi L_{c1}$, implies that $\hat{\nabla} \langle \hat{\mathbf{y}}_B \hat{\mathbf{y}}_B \rangle : \hat{\nabla} \hat{\nabla} \langle c_3 \rangle_B$ is much smaller than $\phi \hat{\nabla} \langle c_3 \rangle_B$ and can be neglected [8, p. 20]. With these approximations, (A.1) reduces to

$$\langle \hat{\nabla}^2 c_3 \rangle = \hat{\nabla} \cdot \left(\phi \hat{\nabla} \langle c_3 \rangle_B + \frac{1}{|\mathcal{V}|} \int_{A_{ls}} \tilde{c}_3 \mathbf{n} \mathrm{d}A \right) - a_v \mathrm{Da}_{ls} \frac{\langle c_3 \rangle_{ls} - 1}{l}. \tag{A.2}$$

To complete the proof, one has to show that $\langle c_3 \rangle_{ls}$ can be replaced with $\langle c_3 \rangle_B$. The third constraint, $l \ll L_c$, is required for the inequality $\langle c_3 \rangle_B \gg \tilde{c}_3$ to hold [8, p. 29, Eqs. 1.4-23], so that $\langle c_3 \rangle_{ls} \approx \langle\langle c_3 \rangle_B \rangle_{ls}$. The fourth, $r_0 \ll L_c$, and fifth, $r_0^2 \ll L_c L_{c1}$, constraints guarantee that $\langle\langle c_3 \rangle_B \rangle_{ls} \approx \langle c_3 \rangle_B$ [8, p. 20]. Substituting $\langle c_3 \rangle_{ls} = \langle c_3 \rangle_B$ into (A.2) leads to (3.14).

A.2 Proposition 3.3.2

Using the decomposition $c_i = \langle c_i \rangle_B + \tilde{c}_i$ $(i = 1, 2)$ in the average of the nonlinear term $\langle c_1 c_2 \rangle$ yields

$$\langle c_1 c_2 \rangle = \langle\langle c_1 \rangle_B \langle c_2 \rangle_B \rangle + \langle \tilde{c}_1 \langle c_2 \rangle_B \rangle + \langle\langle c_1 \rangle_B \tilde{c}_2 \rangle + \langle \tilde{c}_2 \tilde{c}_1 \rangle. \tag{A.3}$$

The constraint 3 of Proposition 3.3.1, $\epsilon \ll 1$, allows one to disregard the terms containing pore-scale fluctuations $\tilde{c}_i$ $(i = 1, 2)$ so that

$$\langle c_1 c_2 \rangle \approx \langle\langle c_1 \rangle_B \langle c_2 \rangle_B \rangle = \frac{1}{|\mathscr{V}|} \int_B \langle c_1 \rangle_B (\hat{\mathbf{x}} + \hat{\mathbf{y}}_B) \langle c_2 \rangle^l (\hat{\mathbf{x}} + \hat{\mathbf{y}}_B) \mathrm{d}^3 r. \tag{A.4}$$

Taylor expansions of the averaged concentrations around the centroid $\hat{\mathbf{x}}$ leads to

$$\langle c_1 c_2 \rangle \approx \phi \langle c_1 \rangle_B \langle c_2 \rangle_B + \langle c_1 \rangle_B \langle \hat{\mathbf{y}}_B \rangle \cdot \hat{\nabla} \langle c_2 \rangle_B + \frac{1}{2} \langle c_1 \rangle_B \langle \hat{\mathbf{y}}_B \hat{\mathbf{y}}_B \rangle : \hat{\nabla} \hat{\nabla} \langle c_2 \rangle_B$$
$$+ \langle c_2 \rangle_B \langle \hat{\mathbf{y}}_B \rangle \cdot \hat{\nabla} \langle c_1 \rangle_B + \frac{1}{2} \langle c_2 \rangle_B \langle \hat{\mathbf{y}}_B \hat{\mathbf{y}}_B \rangle : \hat{\nabla} \hat{\nabla} \langle c_1 \rangle_B + \hat{\nabla} \langle c_1 \rangle_B \langle \hat{\mathbf{y}}_B \hat{\mathbf{y}}_B \rangle \hat{\nabla} \langle c_2 \rangle_B + \dots \tag{A.5}$$

Since $\langle \hat{\mathbf{y}}_B \rangle = \mathcal{O}(\phi r_0)$ [8, p. 31], the constraint (4) of Proposition 3.3.1, $r_0 \ll L_c$, gives the following estimate

$$\langle c_1 \rangle_B \langle \hat{\mathbf{y}}_B \rangle \cdot \hat{\nabla} \langle c_2 \rangle_B = \mathcal{O}\left(\frac{r_0}{L_c} \phi \langle c_1 \rangle_B \langle c_2 \rangle_B \right) \ll \langle c_1 \rangle_B \langle c_2 \rangle_B. \tag{A.6}$$

An analogous estimate holds for $\langle c_2 \rangle_B \langle \hat{\mathbf{y}}_B \rangle \cdot \hat{\nabla} \langle c_1 \rangle_B$. Since $\langle \hat{\mathbf{y}}_B \hat{\mathbf{y}}_B \rangle = \mathcal{O}(\phi r_0^2)$ [8, p. 19], the constraint 5 of Proposition 3.3.1, $r_0^2 \ll L_c L_{c1}$, leads to an estimate

$$\langle c_1 \rangle_B \langle \hat{\mathbf{y}}_B \hat{\mathbf{y}}_B \rangle : \hat{\nabla} \hat{\nabla} \langle c_2 \rangle_B = \frac{r_0^2}{L_c L_{c1}} \mathcal{O}(\phi \langle c_1 \rangle_B \langle c_2 \rangle^l) \ll \langle c_1 \rangle_B \langle c_2 \rangle_B. \tag{A.7}$$

An analogous estimate holds for $\langle c_2 \rangle_B \langle \hat{\mathbf{y}}_B \hat{\mathbf{y}}_B \rangle : \hat{\nabla} \hat{\nabla} \langle c_1 \rangle_B$. Finally, the constraint 4 of Proposition 3.3.1, $r_0^2 \ll L_c^2$, yields an estimate

$$\hat{\nabla} \langle c_1 \rangle_B \langle \hat{\mathbf{y}}_B \hat{\mathbf{y}}_B \rangle \hat{\nabla} \langle c_2 \rangle_B = \frac{r_0^2}{L_c^2} \mathcal{O}(\phi \langle c_1 \rangle_B \langle c_2 \rangle_B) \ll \langle c_1 \rangle_B \langle c_2 \rangle_B. \tag{A.8}$$

Substituting these estimates into (A.5) leads to the approximation (3.15).

A.3   Proposition 3.3.3

Given the approximations (3.14) and (3.15), the volume averaging of (3.6) yields

$$q\frac{\partial\langle c_3\rangle_B}{\partial t} = \frac{ql^2}{\mathrm{Da}}\left(\hat{\nabla}^2\langle c_3\rangle_B + \frac{1}{\phi}\hat{\nabla}\phi\cdot\hat{\nabla}\langle c_3\rangle_B + \frac{1}{\phi|\mathscr{V}|}\hat{\nabla}\cdot\int_{A_{ls}}\tilde{c}_3\mathbf{n}_{ls}\mathrm{d}A\right)$$
$$- \frac{qa_vl}{\phi}\frac{\mathrm{Da}_{ls}}{\mathrm{Da}}(\langle c_3\rangle_B - 1) + \langle c_1\rangle_B\langle c_2\rangle_B - K\langle c_3\rangle_B. \tag{A.9}$$

The equation governing the dynamics of the concentration fluctuations $\tilde{c}_3$ is obtained by subtracting (A.9) from (3.6),

$$q\frac{\partial\tilde{c}_3}{\partial t} = \frac{ql^2}{\mathrm{Da}}\left(\hat{\nabla}^2\tilde{c}_3 - \frac{1}{\phi}\hat{\nabla}\phi\cdot\hat{\nabla}\langle c_3\rangle_B - \frac{1}{\phi|\mathscr{V}|}\hat{\nabla}\cdot\int_{A_{ls}}\tilde{c}_3\mathbf{n}_{ls}\mathrm{d}A\right)$$
$$+ \frac{qa_vl}{\phi}\frac{\mathrm{Da}_{ls}}{\mathrm{Da}}(\langle c_3\rangle_B - 1) + c_1c_2 - \langle c_1\rangle_B\langle c_2\rangle_B - K\tilde{c}_3. \tag{A.10}$$

The constraint 1 of Proposition 3.3.3, $a_v \approx l^{-1}$, implies that the integral term in (A.10) is much smaller than $\hat{\nabla}^2\tilde{c}_3$ and, hence, can be neglected [8, p. 26]. If $t \gg \mathrm{Da}$, the constraint 2 of Proposition 3.3.3, the closure problem can be considered quasi-steady, i.e., the time derivative in (A.10) can be dropped. The constraint 3 of Proposition 3.3.3, $l \ll L_\phi$, ensures that $\phi^{-1}\hat{\nabla}\phi\cdot\hat{\nabla}\langle c_3\rangle_B$ can be neglected [8, p. 27]. Combining these approximations with the decomposition $c_i = \langle c_i\rangle_B + \tilde{c}_i$ $(i = 1, 2)$ of the term c_1c_2 in (A.10) yields the equation for fluctuations (3.16). A similar procedure leads to the boundary condition (3.17).

A.4   Proposition 3.3.4

Further progress requires one to assume that a porous medium is spatially periodic [18], [8]. This allows one to solve for $\tilde{c}$ in some representative region and then use this solution to construct a closure. Since boundary conditions on the surface of a computational domain have negligible influence on $\tilde{c}$-field almost everywhere [96], one can impose a periodic condition at the boundary of the unit cell, $\tilde{c}(\hat{\mathbf{r}}+\hat{\mathbf{l}}_i) = \tilde{c}(\hat{\mathbf{r}})$, where $\hat{\mathbf{l}}_i$ $(i = 1, 2, 3)$ represent the three non-unique lattice vectors describing a spatially periodic porous medium. It is important to recognize that this periodic boundary condition is consistent with the equations for fluctuations only if the geometry is periodic and source terms are either constant or spatially periodic inside the representative volume.

Expanding $\langle c_3 \rangle_B$ and $\hat{\nabla} \langle c_3 \rangle_B$ in (3.16) and (3.17) into Taylor series around the centroid $\hat{\mathbf{x}}$ and invoking the constraint 4 of Proposition 3.3.1 to neglect the higher-order terms, one obtains a local formulation for the $\tilde{c}_3$-field [8, p. 32]. In this formulation, reactive sources (the terms proportional to $\langle c_i \rangle_B$) and diffusive sources (the terms proportional to $\hat{\nabla} \langle c_i \rangle_B$) are evaluated at the centroid $\hat{\mathbf{x}}$ and, hence, are treated as constant and spatially periodic, respectively [8, p. 32]. This ensures that the periodic boundary conditions $\tilde{c}(\hat{\mathbf{r}} + \hat{\mathbf{l}}_i) = \tilde{c}(\hat{\mathbf{r}})$ are consistent with (3.16) and (3.17).

A.5 Proposition 3.3.5

Let $c_4 \equiv c_3 - 1$. Hence, $\langle c_3 \rangle_B - 1 = \langle c_4 \rangle_B$ and $\tilde{c}_3 = \tilde{c}_4$. Equation and boundary condition for deviation $\tilde{c}_4$ can be obtained respectively from (3.16) and (3.17) through the previous substitutions. An order-of-magnitude analysis of boundary condition for $\tilde{c}_4$ leads to estimates

$$\tilde{c}_4 = \mathcal{O}\left(\frac{\epsilon + \mathrm{Da}_{ls}}{1 + \mathrm{Da}_{ls}} \langle c_4 \rangle_B \right) \qquad \Rightarrow \qquad \tilde{c}_4 = \mathcal{O}\left(\epsilon \langle c_4 \rangle_B \right). \tag{A.11}$$

The second estimate in (A.11) stems from the constraint 3 of Proposition 3.3.1, $\epsilon \ll 1$, and the constraint 1 of Proposition 3.3.5, $\mathrm{Da}_{ls} \ll \epsilon$. The estimate (A.11) allows one to simplify the boundary condition for $\tilde{c}_4$ and consequently to approximate the boundary condition (3.17) with

$$-\mathbf{n} \cdot \hat{\nabla} \tilde{c}_3 = \mathbf{n} \cdot \hat{\nabla} \langle c_3 \rangle_B + \mathrm{Da}_{ls} \frac{\langle c_3 \rangle_B - 1}{l} \qquad \text{on } \mathscr{A}_{ls}. \tag{A.12}$$

The estimate (A.11) also leads to the following order-of-magnitude estimates of the terms in the equation for $\tilde{c}_4$: $ql^2 \hat{\nabla}^2 \tilde{c}_4 / \mathrm{Da} = \mathcal{O}(q\epsilon \langle c_4 \rangle_B / \mathrm{Da})$, $qa_v l \mathrm{Da}_{ls} \langle c_4 \rangle_B / \phi \mathrm{Da} = \mathcal{O}(q \mathrm{Da}_{ls} \langle c_4 \rangle_B / \mathrm{Da})$, $K \tilde{c}_4 = \mathcal{O}(\epsilon K \langle c_4 \rangle_B)$, $\langle c_i \rangle_B \tilde{c}_j = \mathcal{O}(\epsilon \langle c_i \rangle_B \langle c_j \rangle_B)$ for $i, j = \{1, 2\}$ such that $i \neq j$, and $\tilde{c}_1 \tilde{c}_2 = \mathcal{O}(\epsilon^2 \langle c_1 \rangle_B \langle c_2 \rangle_B)$. An order-of magnitude relation between $\langle c_4 \rangle_B$ and $\langle c_1 \rangle_B$ (or $\langle c_2 \rangle_B$) is needed in order to compare the terms containing perturbations $\tilde{c}_1$ and $\tilde{c}_2$ with those containing $\tilde{c}_4$ and $\langle c_4 \rangle_B$. It is obtained from equations for $\tilde{c}_1$ (or $\tilde{c}_2$) by recognizing that $-l^2 \hat{\nabla}^2 \tilde{c}_1 / \mathrm{Da} = ql^2 \hat{\nabla}^2 \tilde{c}_4 / \mathrm{Da} + qa_v l \mathrm{Da}_{ls} \langle c_4 \rangle_B / \phi \mathrm{Da}$, which leads to estimates

$$\langle c_4 \rangle_B = \mathcal{O}\left(\frac{\epsilon}{\epsilon + \mathrm{Da}_{ls}} \frac{\langle c_1 \rangle_B}{q} \right) \qquad \Rightarrow \qquad \langle c_4 \rangle_B = \mathcal{O}\left(\frac{\langle c_1 \rangle_B}{q} \right). \tag{A.13}$$

The estimate (A.13) combined with the constraint 2 of Proposition 3.3.5 allows one to neglect the terms containing deviation $\tilde{c}_1$ and $\tilde{c}_2$ (i.e., $\tilde{c}_1\tilde{c}_2$ and $\langle c_i\rangle_B\tilde{c}_j$ for $i,j = \{1,2\}$ such that $i \neq j$) relative to the diffusion term $ql^2\hat{\nabla}^2\tilde{c}_4/\text{Da}$. For example, the order of magnitude of the ratio between $ql^2\hat{\nabla}^2\tilde{c}_4/\text{Da}$ and $\langle c_1\rangle_B\tilde{c}_2$ is $\mathcal{O}(\text{Da}\langle c_2\rangle_B)$ for $\langle c_1\rangle_B \neq 0$. Since $0 \leq \langle c_2\rangle_B \leq 1$, this yields $\langle c_1\rangle_B\tilde{c}_2 \ll ql^2\hat{\nabla}^2\tilde{c}_4/\text{Da}$ if $\text{Da} \ll 1$. Neglecting the fluctuation terms in the equation for $\tilde{c}_4$ allows one to approximate (3.16) as

$$\hat{\nabla}^2\tilde{c}_3 - \frac{k_3}{\mathscr{D}}\tilde{c}_3 = -\frac{a_v\text{Da}_{ls}}{\phi l}\left(\langle c_3\rangle_B - 1\right) \qquad \text{in } V_l. \tag{A.14}$$

In the spirit of [8], we represent a solution of (A.12) and (A.14) as

$$\tilde{c}_3 = \hat{\mathbf{b}} \cdot \hat{\nabla}\langle c_3\rangle_B + s\langle c_3\rangle_B + \psi, \tag{A.15}$$

where $\hat{\mathbf{b}}$, s and ψ are undetermined functions called closure variables. They are specified as solutions of the boundary value problems (3.19), (3.20) and (3.21), which are obtained by substituting (A.15) into (A.14).

Condition 2 of Proposition 3.3.5 is required for similar analysis of equations for c_1 and c_2.

A.6   Miscellaneous

Derivation of (3.22) *and* (3.23). Substitution of (A.15) into (A.9) gives

$$q\frac{\partial\langle c_3\rangle_B}{\partial t} = \frac{ql^2}{\phi\text{Da}}\hat{\nabla} \cdot \left[\phi(\mathbf{D}_{\text{eff}} \cdot \hat{\nabla}\langle c_3\rangle_B + \mathbf{u}\langle c_3\rangle_B + \mathbf{p})\right] - \frac{qa_v l}{\phi}\frac{\text{Da}_{ls}}{\text{Da}}[\langle c_3\rangle_B - 1]$$
$$+ \langle c_1\rangle_B\langle c_2\rangle_B - K\langle c_3\rangle_B \tag{A.16}$$

where $\mathbf{D}_{\text{eff}}$ is given by (3.24) and $\mathbf{u}$ and $\mathbf{p}$ are defined as

$$\mathbf{u} = \frac{1}{|B|}\int_{A_{ls}} s\mathbf{n}_{ls}\text{d}A, \qquad \mathbf{p} = \frac{1}{|B|}\int_{A_{ls}} \psi\mathbf{n}_{ls}\text{d}A. \tag{A.17}$$

The constraint 1 of Proposition 3.3.3, $a_v \approx l^{-1}$, and Equation (3.20), that provides an estimate for s, imply that $ql^2\hat{\nabla}\cdot(\phi\mathbf{u}\langle c_3\rangle_B)/\phi\text{Da}$ is much smaller than $qa_v l\text{Da}_{ls}\langle c_3\rangle_B/\phi\text{Da}$ and, thus, can be neglected [8, p. 36]. Similar results can be obtained for $ql^2\hat{\nabla}\cdot(\phi\mathbf{p})/\phi\text{Da}$ that can be neglected respect to $qa_v l\text{Da}_{ls}/\phi\text{Da}$. With this approximations (A.16) reduces

to (3.23), wherein the space coordinates are scaled with a typical macroscopic length, e.g., L_c.

A similar procedure leads to (3.22).

Analysis of Ochoa-Tapia et al. [32]. The derivation of macroscopic equations (3.22) and (3.23) is tantamount to a closure for $\langle c_1 c_2 \rangle$ in which all terms containing concentration fluctuations, i.e., $\tilde{c}_1 \tilde{c}_2$ and $\tilde{c}_k \langle c_j \rangle_B$ ($k, j = \{1, 2\}$ such that $k \neq j$), are neglected. It requires the set of constraints specified in Propositions 3.3.1–3.3.5. Ochoa-Tapia et al. [32] neglects $\tilde{c}_1 \tilde{c}_2$ while retaining $\tilde{c}_k \langle c_j \rangle_B$ ($k, j = \{1, 2\}$ such that $k \neq j$). This leads to a closure for $\langle c_1 c_2 \rangle$ where one of these constraints, $\mathrm{Da} \ll 1$, needs to be replaced with $1 \ll \mathrm{Da} \ll 1/\epsilon$. The closure results in a system of equations for pore-scale fluctuations $A_{ij} \tilde{c}_j = b_i$—where $A_{11} = (l^2/\mathrm{Da})\hat{\nabla}^2 - \langle c_2 \rangle_B$, $A_{22} = (l^2/\mathrm{Da})\hat{\nabla}^2 - \langle c_1 \rangle_B$, $A_{33} = (q l^2/\mathrm{Da})\hat{\nabla}^2 - K$, $A_{12} = -\langle c_1 \rangle_B$, $A_{21} = -\langle c_2 \rangle_B$, $A_{31} = \langle c_2 \rangle_B$, $A_{32} = \langle c_1 \rangle_B$, $b_3 = -(q a_v l \mathrm{Da}_{ls}/\phi \mathrm{Da})(\langle c_3 \rangle_B - 1)$, $A_{13} = A_{23} = K$ and $b_1 = b_2 = 0$—that must be solved *simultaneously* with a macroscopic problem (see Fig. 4.1).

Appendix B

Homogenization of Transport Equations

Replacing $c_\varepsilon(\mathbf{x}, t)$ with $c(\mathbf{x}, \mathbf{y}, t, \tau_r, \tau_a)$ gives the following relations for the spatial and temporal derivatives,

$$\nabla c_\varepsilon = \nabla_\mathbf{x} c + \frac{1}{\varepsilon} \nabla_\mathbf{y} c \tag{B.1}$$

and

$$\frac{\partial c_\varepsilon}{\partial t} = \frac{\partial c}{\partial t} + \mathrm{Da} \frac{\partial c}{\partial \tau_r} + \mathrm{Pe} \frac{\partial c}{\partial \tau_a}. \tag{B.2}$$

Substitution of (B.1) and (B.2) into (4.10) and (4.11) yields

$$\frac{\partial c}{\partial t} + \mathrm{Da} \frac{\partial c}{\partial \tau_r} + \mathrm{Pe} \frac{\partial c}{\partial \tau_a} + \nabla_\mathbf{x} \cdot \left[-\mathbf{D}(\nabla_\mathbf{x} c + \varepsilon^{-1} \nabla_\mathbf{y} c) + \mathrm{Pe}\, \mathbf{v}\, c \right]$$
$$+ \varepsilon^{-1} \nabla_\mathbf{y} \cdot \left[-\mathbf{D}(\nabla_\mathbf{x} c + \varepsilon^{-1} \nabla_\mathbf{y} c) + \mathrm{Pe}\, \mathbf{v}\, c \right] = 0, \qquad \mathbf{y} \in B \tag{B.3}$$

and

$$-\mathbf{n} \cdot \mathbf{D}(\nabla_\mathbf{x} c + \varepsilon^{-1} \nabla_\mathbf{y} c) = \mathrm{Da}(c^a - 1), \qquad \mathbf{y} \in A_{ls}, \tag{B.4}$$

respectively. Substituting (4.19) and (4.20) into (B.3) leads to

$$
\varepsilon^{-2}\left[\nabla_{\mathbf{y}}\cdot(-\mathbf{D}\nabla_{\mathbf{y}}c_0 + \varepsilon^{1-\alpha}c_0\mathbf{v}_0)\right]
$$

$$
+\varepsilon^{-1}\Big\{-\nabla_{\mathbf{x}}\cdot\mathbf{D}\nabla_{\mathbf{y}}c_0 - \nabla_{\mathbf{y}}\cdot\mathbf{D}(\nabla_{\mathbf{y}}c_1 + \nabla_{\mathbf{x}}c_0)
$$

$$
+ \varepsilon^{1-\alpha}\left[\frac{\partial c_0}{\partial\tau_a} + \varepsilon^{\alpha+\beta}\frac{\partial c_0}{\partial\tau_r} + \nabla_{\mathbf{x}}\cdot(c_0\mathbf{v}_0) + \nabla_{\mathbf{y}}\cdot(c_1\mathbf{v}_0 + c_0\mathbf{v}_1)\right]\Big\}
$$

$$
+\varepsilon^{0}\Big\{\frac{\partial c_0}{\partial t} - \nabla_{\mathbf{x}}\cdot\mathbf{D}(\nabla_{\mathbf{x}}c_0 + \nabla_{\mathbf{y}}c_1) - \nabla_{\mathbf{y}}\cdot\mathbf{D}\left(\nabla_{\mathbf{x}}c_1 + \nabla_{\mathbf{y}}c_2\right) +
$$

$$
+ \varepsilon^{1-\alpha}\left[\frac{\partial c_1}{\partial\tau_a} + \varepsilon^{\alpha+\beta}\frac{\partial c_1}{\partial\tau_r} + \nabla_{\mathbf{x}}\cdot(c_1\mathbf{v}_0 + c_0\mathbf{v}_1)\right.
$$

$$
\left.+ \nabla_{\mathbf{y}}\cdot(c_1\mathbf{v}_1 + c_0\mathbf{v}_2 + c_2\mathbf{v}_0)\right]\Big\} = \mathcal{O}\left(\varepsilon\right), \qquad \mathbf{y}\in B. \qquad \text{(B.5)}
$$

Similarly, boundary condition (B.4) can be written as

$$
\varepsilon^{-1}(-\mathbf{n}\cdot\mathbf{D}\nabla_{\mathbf{y}}c_0) + \varepsilon^{0}\big[-\mathbf{n}\cdot\mathbf{D}(\nabla_{\mathbf{x}}c_0 + \nabla_{\mathbf{y}}c_1) - \varepsilon^{\beta}(c_0^a - 1)\big]
$$

$$
+\varepsilon\big[-\mathbf{n}\cdot\mathbf{D}(\nabla_{\mathbf{x}}c_1 + \nabla_{\mathbf{y}}c_2) - \varepsilon^{\beta}c_0^{a-1}c_1\big] = \mathcal{O}\left(\varepsilon^2\right), \qquad \mathbf{y}\in A_{ls}. \qquad \text{(B.6)}
$$

Next, we collect the terms of like-powers in ε under condition that $\alpha < 2$, which is required for the homogenizability of the advection-dispersion equation [19, Sec. 3.5, Tab. 1].

B.1 Terms of order $\mathcal{O}\left(\varepsilon^{-2}\right)$

Collecting the leading-order terms in (B.5) and (B.6), we obtain a partial differential equation (PDE),

$$
\nabla_{\mathbf{y}}\cdot(-\mathbf{D}\nabla_{\mathbf{y}}c_0 + \varepsilon^{1-\alpha}c_0\mathbf{v}_0) = 0, \qquad \mathbf{y}\in B, \qquad \text{(B.7)}
$$

subject to the boundary condition

$$
-\mathbf{n}\cdot(\mathbf{D}\nabla_{\mathbf{y}}c_0) = 0, \qquad \mathbf{y}\in A_{ls}. \qquad \text{(B.8)}
$$

The homogeneity of both (B.7) and (B.8) ensures that this boundary-value problem has a trivial solution, i.e., that c_0 is independent of $\mathbf{y}$,

$$
c_0 = c_0(\mathbf{x}, t, \tau_r, \tau_a), \qquad \text{for any } \alpha < 2. \qquad \text{(B.9)}
$$

Note that this result does not require the convoluted analysis presented in [19, Eq. 48-49].

B.2   Terms of order $\mathcal{O}\left(\varepsilon^{-1}\right)$

Since $\nabla_{\mathbf{y}} c_0 \equiv \mathbf{0}$, the next order terms in (B.5) and (B.6) give rise to a PDE

$$-\nabla_{\mathbf{y}} \cdot \mathbf{D}(\nabla_{\mathbf{y}} c_1 + \nabla_{\mathbf{x}} c_0) + \varepsilon^{1-\alpha}\left[\frac{\partial c_0}{\partial \tau_a} + \varepsilon^{\alpha+\beta}\frac{\partial c_0}{\partial \tau_r} + \nabla_{\mathbf{x}} \cdot (c_0 \mathbf{v}_0)\right.$$
$$\left. + \nabla_{\mathbf{y}} \cdot (c_1 \mathbf{v}_0 + c_0 \mathbf{v}_1)\right] = 0, \qquad \mathbf{y} \in B. \qquad (B.10)$$

subject to the boundary condition

$$-\mathbf{n} \cdot \mathbf{D}(\nabla_{\mathbf{x}} c_0 + \nabla_{\mathbf{y}} c_1) - \varepsilon^{\beta}(c_0^a - 1) = 0, \qquad \mathbf{y} \in A_{ls}. \qquad (B.11)$$

Integrating (B.10) over B with respect to $\mathbf{y}$, while accounting for the no-slip boundary condition on A_{ls}, the boundary condition (B.11), and the periodicity of the coefficients on the external boundary of the unit cell $\partial\mathscr{V}$, we obtain

$$\varepsilon^{1-\alpha}\frac{\partial c_0}{\partial \tau_a} + \varepsilon^{1+\beta}\frac{\partial c_0}{\partial \tau_r} = -\varepsilon^{1-\alpha}\nabla_{\mathbf{x}} \cdot (c_0 \langle \mathbf{v}_0 \rangle_B) - \varepsilon^{\beta}\mathscr{K}^*(c_0^a - 1) \qquad (B.12)$$

where $\mathscr{K}^*$ is defined by (4.22).

Combining (B.12) with (B.10) to eliminate the temporal derivatives, we obtain

$$\varepsilon^{1-\alpha}\left[-\nabla_{\mathbf{x}} \cdot (c_0 \langle \mathbf{v}_0 \rangle_B) - \varepsilon^{\alpha+\beta-1}\mathscr{K}^*(c_0^a - 1) + \nabla_{\mathbf{x}} \cdot (c_0 \mathbf{v}_0)\right]$$
$$+ \nabla_{\mathbf{y}} \cdot (c_1 \mathbf{v}_0 + c_0 \mathbf{v}_1) - \nabla_{\mathbf{y}} \cdot \mathbf{D}\left(\nabla_{\mathbf{y}} c_1 + \nabla_{\mathbf{x}} c_0\right) = 0. \qquad (B.13)$$

Since $\nabla_{\mathbf{y}} \cdot \mathbf{v}_0 = 0$ [19, Eq. 20], $\nabla_{\mathbf{x}} \cdot \langle \mathbf{v}_0 \rangle_B = 0$ [19, Eq. 26], $\nabla_{\mathbf{y}} \cdot \mathbf{v}_1 + \nabla_{\mathbf{x}} \cdot \mathbf{v}_0 = 0$ [19, Eq. 25], and $\nabla_{\mathbf{y}} c_0 = \mathbf{0}$ from (B.9), this gives

$$\varepsilon^{1-\alpha}\left[(\mathbf{v}_0 - \langle \mathbf{v}_0 \rangle_B)\nabla_{\mathbf{x}} c_0 - \varepsilon^{\alpha+\beta-1}\mathscr{K}^*(c_0^a - 1) + \mathbf{v}_0\nabla_{\mathbf{y}} c_1\right]$$
$$- \nabla_{\mathbf{y}} \cdot \mathbf{D}(\nabla_{\mathbf{y}} c_1 + \nabla_{\mathbf{x}} c_0) = 0. \qquad (B.14)$$

Equations (B.14) and (B.11) form a boundary value problem for c_1. Following [19, Eq. 40] and [16, p. 10, Eqs. 3.6–3.7], we look for a solution in the form

$$c_1(\mathbf{x}, \mathbf{y}, t, \tau_r, \tau_a) = \boldsymbol{\chi}(\mathbf{y}) \cdot \nabla_{\mathbf{x}} c_0(\mathbf{x}, t, \tau_r, \tau_a) + \bar{c}_1(\mathbf{x}, t, \tau_r, \tau_a). \qquad (B.15)$$

Substitution of (B.15) into (B.14) and (B.11) leads to the following cell problem for the closure variable $\boldsymbol{\chi}(\mathbf{y})$:

$$\left[-\nabla_{\mathbf{y}} \cdot \mathbf{D}(\nabla_{\mathbf{y}}\boldsymbol{\chi} + \mathbf{I}) + \varepsilon^{1-\alpha}\mathbf{v}_0 \cdot \nabla_{\mathbf{y}}\boldsymbol{\chi}\right] \cdot \nabla_{\mathbf{x}} c_0 = \varepsilon^{1-\alpha}(\langle \mathbf{v}_0 \rangle_B - \mathbf{v}_0) \cdot \nabla_{\mathbf{x}} c_0$$
$$+ \varepsilon^{\beta}\mathscr{K}^*(c_0^a - 1), \qquad \mathbf{y} \in B; \qquad (B.16a)$$

subject to $\langle \boldsymbol{\chi} \rangle = 0$ and

$$-[\mathbf{n} \cdot \mathbf{D}(\nabla_{\mathbf{y}}\boldsymbol{\chi} + \mathbf{I})] \cdot \nabla_{\mathbf{x}}c_0 = \varepsilon^{\beta}(c_0^a - 1), \qquad \mathbf{y} \in A_{ls}. \tag{B.16b}$$

Note that $\boldsymbol{\chi}(\mathbf{y})$ is a $\mathcal{V}$-periodic vector field.

The boundary-value problem (B.16) couples the pore scale with the continuum scale, in the sense that the closure variable $\boldsymbol{\chi}(\mathbf{y})$—a solution of the pore-scale cell problem (B.16)—is influenced by the continuum scale through its dependence on the macroscopic concentration $c_0(\mathbf{x})$. This coupling is incompatible with the general representation (B.15). This inconsistency is resolved by imposing the following constraints on the exponents α and β.

We start with the boundary condition in (B.16b), whose left-hand-side is of order ϵ^0. If we chose $\beta > 0$, then the right-hand-site, which is of order ϵ^{β}, can be neglected since $\epsilon \ll 1$ (Constraint 1 of section 4.3.2). Next, we observe that for the term $\varepsilon^{\beta} \mathscr{K}^*(c_0^a - 1)$ to be negligible relative to the smallest term in (B.16a) it is necessary that $\beta > \max\{0, 1 - \alpha\}$. Since homogenizability of pore-scale advection-diffusion transport of a conservative solute requires that $\alpha < 2$ [19, Sec. 3.5, Tab. 1], this condition yields either $\beta + \alpha > 1$ if $\alpha < 1$ or $\beta > 0$ if $1 < \alpha < 2$.

The selection of proper α and β ensures that $\boldsymbol{\chi}$ is independent of c_0. The dependence of $\boldsymbol{\chi}$ on $\nabla_{\mathbf{x}}c_0$ is eliminated by defining $\boldsymbol{\chi}$ as a solution of the related cell problem (4.24). Finally, recalling the definitions of Da and Pe in (4.20) allows us to reformulate the conditions on α and β in the form of constraints 2)–4) of section 4.3.2.

Having identified the conditions that guarantee homogenizability, we proceed to derive the effective transport equation (4.21).

B.3   Terms of order $\mathcal{O}\left(\varepsilon^0\right)$

Collecting the zeroth-order terms in (B.5) and (B.6), we obtain

$$\begin{aligned}
\frac{\partial c_0}{\partial t} &- \nabla_{\mathbf{x}} \cdot \mathbf{D}(\nabla_{\mathbf{x}}c_0 + \nabla_{\mathbf{y}}c_1) - \nabla_{\mathbf{y}} \cdot \mathbf{D}(\nabla_{\mathbf{x}}c_1 + \nabla_{\mathbf{y}}c_2) \\
&+ \varepsilon^{1-\alpha}\left[\frac{\partial c_1}{\partial \tau_a} + \varepsilon^{\alpha+\beta}\frac{\partial c_1}{\partial \tau_r} + \nabla_{\mathbf{x}} \cdot (c_1\mathbf{v}_0 + c_0\mathbf{v}_1)\right. \\
&\left. + \nabla_{\mathbf{y}} \cdot (c_1\mathbf{v}_1 + c_0\mathbf{v}_2 + c_2\mathbf{v}_0)\right] = 0, \qquad \mathbf{y} \in B, \tag{B.17}
\end{aligned}$$

with the boundary condition

$$- \mathbf{n} \cdot \mathbf{D}(\nabla_{\mathbf{x}} c_1 + \nabla_{\mathbf{y}} c_2) - a\varepsilon^{\beta} c_0^{a-1} c_1 = 0, \qquad \mathbf{y} \in A_{ls}. \tag{B.18}$$

Integrating (B.17) over B with respect to $\mathbf{y}$ and using the boundary condition (B.18) leads to

$$\frac{\partial \langle c_0 \rangle_B}{\partial t} - \nabla_{\mathbf{x}} \cdot (\phi^{-1} \mathbf{D}^{**} \nabla_{\mathbf{x}} c_0) + a\varepsilon^{\beta} \mathscr{K}^* c_0^{a-1} \langle c_1 \rangle_{ls}$$
$$+ \varepsilon^{1-\alpha} \left[\frac{\partial \langle c_1 \rangle_B}{\partial \tau_a} + \varepsilon^{\alpha+\beta} \frac{\partial \langle c_1 \rangle_B}{\partial \tau_r} + \nabla_{\mathbf{x}} \cdot (\langle c_1 \mathbf{v}_0 \rangle_B + c_0 \langle \mathbf{v}_1 \rangle_B) \right] = 0 \tag{B.19}$$

where $\mathbf{D}^{**} = \langle \mathbf{D}(\mathbf{I} + \nabla_{\mathbf{y}} \boldsymbol{\chi}) \rangle$. Combining (B.19) with (B.15), while making use of (B.18), the definition $|A_{ls}| \langle c_1 \rangle_{ls} = \int_{A_{ls}} c_1 d\mathbf{y}$, and the relations $c_0 = \langle c_0 \rangle_B$ and $\mathbf{v}_0 = -\mathbf{k}(\mathbf{y}) \cdot \nabla_{\mathbf{x}} p_0$ [19, Eq. 21], we obtain

$$\frac{\partial \langle c_0 \rangle_B}{\partial t} + \varepsilon^{1-\alpha} \frac{\partial \langle c_1 \rangle_B}{\partial \tau_a} + \varepsilon^{1+\beta} \frac{\partial \langle c_1 \rangle_B}{\partial \tau_r} = \nabla_{\mathbf{x}} \cdot (\phi^{-1} \mathbf{D}^* \nabla_{\mathbf{x}} c_0) - a\varepsilon^{\beta} \mathscr{K}^* c_0^{a-1} \langle c_1 \rangle_{ls}$$
$$- \phi^{-1} \varepsilon^{1-\alpha} \nabla_{\mathbf{x}} \cdot (c_0 \langle \mathbf{v}_1 \rangle + \bar{c}_1 \langle \mathbf{v}_0 \rangle), \tag{B.20}$$

where $\mathbf{D}^*(\mathbf{x})$ is given by (4.23).

Next we recall that

$$\langle c \rangle_B = \langle c_\varepsilon \rangle_B = \langle c_0 \rangle_B + \varepsilon \langle c_1 \rangle_B + \mathcal{O}(\varepsilon^2). \tag{B.21}$$

Multiplying the temporal derivative of (B.21) with ε, using (4.20), and recognizing that $\partial \langle c_1 \rangle_B / \partial t$ is of order ε^2, we obtain

$$\varepsilon \frac{\partial \langle c \rangle_B}{\partial t} = \left(\varepsilon^{\beta+1} \frac{\partial \langle c_0 \rangle_B}{\partial \tau_r} + \varepsilon^{1-\alpha} \frac{\partial \langle c_0 \rangle_B}{\partial \tau_a} \right)$$
$$+ \varepsilon \left(\frac{\partial \langle c_0 \rangle_B}{\partial t} + \varepsilon^{\beta+1} \frac{\partial \langle c_1 \rangle_B}{\partial \tau_r} + \varepsilon^{1-\alpha} \frac{\partial \langle c_1 \rangle_B}{\partial \tau_a} \right) + \mathcal{O}\left(\varepsilon^2\right). \tag{B.22}$$

Multiplying (B.20) with ε, adding the result to (B.12), and using (B.22), we obtain

$$\varepsilon \frac{\partial \langle c \rangle_B}{\partial t} = \varepsilon \nabla_{\mathbf{x}} \cdot (\phi^{-1} \mathbf{D}^* \nabla \langle c_0 \rangle_B) - \phi^{-1} \varepsilon^{1-\alpha} \nabla \cdot (\langle c_0 \rangle \langle \mathbf{v}_0 \rangle_B + \varepsilon c_0 \langle \mathbf{v}_1 \rangle + \varepsilon \bar{c}_1 \langle \mathbf{v}_0 \rangle)$$
$$+ \varepsilon^{\beta} \mathscr{K}^* \left(1 - c_0^a - a\varepsilon c_0^{a-1} \langle c_1 \rangle_{ls} \right). \tag{B.23}$$

Since $\bar{c}_1 = \langle c_1 \rangle_B$ (i.e., $\langle \boldsymbol{\chi} \rangle = \phi \langle \boldsymbol{\chi} \rangle_B = \mathbf{0}$) and $\langle c_0 \rangle_B \langle \mathbf{v}_0 \rangle = \langle c_0 \rangle \langle \mathbf{v}_0 \rangle_B$, an expansion

$$\langle c \rangle_B \langle \mathbf{v} \rangle = \langle c_0 \rangle_B \langle \mathbf{v}_0 \rangle + \varepsilon \langle c_0 \rangle_B \langle \mathbf{v}_1 \rangle + \varepsilon \langle c_1 \rangle_B \langle \mathbf{v}_0 \rangle + \mathcal{O}(\varepsilon^2) \tag{B.24}$$

gives

$$\langle c \rangle_B \langle \mathbf{v} \rangle = \langle c_0 \rangle \langle \mathbf{v}_0 \rangle_B + \varepsilon c_0 \langle \mathbf{v}_1 \rangle + \varepsilon \bar{c}_1 \langle \mathbf{v}_0 \rangle + \mathcal{O}(\varepsilon^2). \tag{B.25}$$

Combining this result with an expansion $\varepsilon \langle c \rangle_B = \varepsilon \langle c_0 \rangle_B + \mathcal{O}(\varepsilon^2) = \varepsilon c_0 + \mathcal{O}(\varepsilon^2)$ allows one to express the diffusive term in (B.23) in terms of $\langle c \rangle_B$, which leads to

$$\phi \frac{\partial \langle c \rangle_B}{\partial t} = \nabla_{\mathbf{x}} \cdot (\mathbf{D}^* \nabla_{\mathbf{x}} \langle c \rangle_B) - \mathrm{Pe} \nabla_{\mathbf{x}} \cdot (\langle c \rangle_B \langle \mathbf{v} \rangle)$$
$$+ \varepsilon^{-1} \mathrm{Da} \, \phi \, \mathscr{K}^* \left(1 - \langle c_0 \rangle_B^a - a \varepsilon \langle c_0 \rangle_B^{a-1} \langle c_1 \rangle_{ls} \right). \tag{B.26}$$

If one can assume that $\langle \boldsymbol{\chi} \rangle_{ls} \approx \langle \boldsymbol{\chi} \rangle_B$, then $\langle c_1 \rangle_{ls} \approx \langle c_1 \rangle_B$ and

$$\langle c_0 \rangle_B^a + \varepsilon a \langle c_0 \rangle_B^{a-1} \langle c_1 \rangle_{ls} \approx \langle c_0 \rangle_B^a + \varepsilon a \langle c_0 \rangle_B^{a-1} \langle c_1 \rangle_B = \langle c \rangle_B^a + \mathcal{O}(\varepsilon^2). \tag{B.27}$$

The previous approximation can be derived by observing that

$$\langle c \rangle_B^a = (\langle c_0 \rangle_B + \varepsilon \langle c_1 \rangle_B)^a + \mathcal{O}(\varepsilon^2) = \sum_{\substack{\lambda_0 + \lambda_1 = a \\ \lambda_1 < 2 \\ 0 \leq \lambda_i \in \mathbb{Z}}} \binom{a}{\lambda_0, \lambda_1} \varepsilon^{\lambda_1} \langle c_0 \rangle_B^{\lambda_0} \langle c_1 \rangle_B^{\lambda_1}$$
$$= \langle c_0 \rangle_B^a + \varepsilon a \langle c_0 \rangle_B^{a-1} \langle c_1 \rangle_B + \mathcal{O}(\varepsilon^2). \tag{B.28}$$

Substitution of (B.27) into (B.26) leads to (4.21), which governs the dynamics of $\langle c \rangle_B$ up to ε^2.

Appendix C

Discretized Equations

C.1 Discrete form of (5.18) for nodes other than $I^\star$

Integration of (5.18) over a CV centered at X_I gives

$$\frac{\partial \bar{c}_I}{\partial T} \Delta X_I + (U\bar{c})_{I+1/2} - (U\bar{c})_{I-1/2} = \mathcal{D}_{I+1/2}(\bar{c}_{I+1} - \bar{c}_I) - \mathcal{D}_{I-1/2}(\bar{c}_I - \bar{c}_{I-1})$$
$$- K\bar{c}_I \Delta X_I, \qquad \text{(C.1)}$$

where $\mathcal{D}_s = D/\Delta X_s$ with $s = I - 1/2$ and $I + 1/2$. The total fluxes through the western and eastern faces of the CV centered at X_I are [97]

$$q_{I-1/2} = (U\bar{c})_{I-1/2} - \mathcal{D}_{I-1/2}\left(\bar{c}_I - \bar{c}_{I-1}\right), \qquad \text{(C.2a)}$$

$$q_{I+1/2} = (U\bar{c})_{I+1/2} - \mathcal{D}_{I+1/2}\left(\bar{c}_{I+1} - \bar{c}_I\right), \qquad \text{(C.2b)}$$

respectively. Concentrations $\bar{c}_{I+1/2}$ and $\bar{c}_{I-1/2}$ have to be determined in function of $\bar{c}_I$, $\bar{c}_{I-1}$ and $\bar{c}_{I+1}$. Combining (C.1) and (C.2) and integrating over the macroscopic time step $[T_N, T_{N+1}]$, we obtain

$$(\bar{c}_I^{N+1} - \bar{c}_I^N)\frac{\Delta X_I}{\Delta T} = \theta(q_{I-1/2}^{N+1} - q_{I+1/2}^{N+1} - K\bar{c}_I^{N+1}\Delta X_I)$$
$$+ (1 - \theta)(q_{I-1/2}^N - q_{I+1/2}^N - K\bar{c}_I^N \Delta X_I), \qquad \text{(C.3)}$$

where $\theta \in [0, 1]$. Setting $\theta = 0$, $\theta = 1/2$, or $\theta = 1$ results in an explicit, Cranck-Nicolson, or fully implicit scheme, respectively. The fluxes are evaluated by means of the hybrid

differencing scheme [98], based on a combination of a central (second order accurate) and an upwind (first order accurate) differencing scheme. Accordingly,

$$q_{I-1/2} = \frac{U_{I-1/2}}{2}\left[\left(1 + \frac{2}{\hat{\mathrm{Pe}}_{I-1/2}}\right)\bar{c}_{I-1} + \left(1 - \frac{2}{\hat{\mathrm{Pe}}_{I-1/2}}\right)\bar{c}_I\right], \qquad \text{(C.4a)}$$

$$q_{I+1/2} = \frac{U_{I+1/2}}{2}\left[\left(1 - \frac{2}{\hat{\mathrm{Pe}}_{I+1/2}}\right)\bar{c}_{I+1} + \left(1 + \frac{2}{\hat{\mathrm{Pe}}_{I+1/2}}\right)\bar{c}_I\right], \qquad \text{(C.4b)}$$

$$\text{where} \quad \hat{\mathrm{Pe}}_i = \begin{cases} \mathrm{Pe}_i, & \mathrm{Pe}_i \in (-2,2) \\ 2, & \mathrm{Pe}_i \geq 2 \\ -2, & \mathrm{Pe}_i \leq -2 \end{cases}, \qquad \text{(C.5)}$$

$i = I - 1/2$ and $I + 1/2$, and $\mathrm{Pe}_i = U_i/\mathcal{D}_i$. Combination of (C.3) and (C.4) with the fully implicit time integration scheme ($\theta = 1$) leads to (5.24), where

$$A_{I-1} = -a_{I-1}, \quad A_I = \frac{\Delta X_I}{\Delta T} + \bar{a}_I, \quad A_{I+1} = -a_{I+1}, \quad a_0 = 0 \qquad \text{(C.6a)}$$

$$a_{I+1} = \max\left(-U_{I+1/2}, \mathcal{D}_{I+1/2} - \frac{U_{I+1/2}}{2}, 0\right), \quad \mathcal{D}_{I+1/2} = \frac{D}{\Delta X_{I+1/2}} \qquad \text{(C.6b)}$$

$$a_{I-1} = \max\left(-U_{I-1/2}, \mathcal{D}_{I-1/2} + \frac{U_{I-1/2}}{2}, 0\right), \quad \mathcal{D}_{I-1/2} = \frac{D}{\Delta X_{I-1/2}} \qquad \text{(C.6c)}$$

$$a_{N_X a} = 0, \quad \bar{a}_I = a_{I-1} + a_{I+1} + (U_{I+1/2} - U_{I-1/2}) + K\Delta X_I - \overline{S}_I \qquad \text{(C.6d)}$$

$$\mathrm{RHS}_I^N = \frac{\Delta X_I}{\Delta T}\bar{c}_I^N + \tilde{S}_I, \qquad \text{(C.6e)}$$

and $\tilde{S}_I$ and $\overline{S}_I$ are determined by numerical discretization of boundary conditions at the macroscale. For uniform velocity U, we obtain (5.25).

C.2 Discrete form of (5.19) in node $I^\star$

Integrating (5.19) over the macroscopic CV centered at node $I^\star$ and over a macroscale time step, and using the implicit time integration scheme ($\theta = 1$), gives

$$\frac{\Delta X_{I^\star}}{\Delta T}(\bar{c}_{I^\star}^{N+1} - \bar{c}_{I^\star}^N) = d_{I^\star+1/2}(\bar{c}_{I^\star+1}^{N+1} - \bar{c}_{I^\star}^{N+1}) - d_{I^\star-1/2}(\bar{c}_{I^\star}^{N+1} - \bar{c}_{I^\star-1}^{N+1}) +$$

$$+ \frac{\Delta t}{\Delta T}\sum_{k=1}^{n_t}\left[\sum_{i=1}^{n_x}\int_{x_{i-1/2}}^{x_{i+1/2}} g(x)\mathrm{d}x\right]^{k+1}, \qquad \text{(C.7)}$$

where

$$g(x) = -\frac{\mathscr{K}}{2H}\left[c(x, y = H) + c(x, y = -H)\right] - \frac{1}{2H}\int_{-H}^{H} u(y)\frac{\partial c}{\partial x}\mathrm{d}y. \tag{C.8}$$

Using a numerical quadrature for the spatial integral in (C.7) yields

$$\frac{\Delta t}{\Delta T}\sum_{k=1}^{n_t}\sum_{i=1}^{n_x}\Delta x_i\left[g(x_i)\right]^{k+1} = \frac{1}{2HN_T}\sum_{k=1}^{n_t}\sum_{i=1}^{n_x}\Delta x_i\Big[-\mathscr{K}\left(c_{i,H} + c_{i,-H}\right) +$$

$$-\int_{-H}^{H} u(y)\frac{c_{i+1/2,y} - c_{i-1/2,y}}{\Delta x_i}\mathrm{d}y\Big]^{k+1}. \tag{C.9}$$

If $\mathrm{Pe} \in (-2, 2)$, then $c_{i+1/2}$ and $c_{i-1/2}$ $(i = 2, \ldots, n_x - 1)$ can be approximated by

$$c_{i-1/2} = \frac{c_{i-1} + c_i}{2}, \quad c_{i+1/2} = \frac{c_i + c_{i+1}}{2}. \tag{C.10}$$

At the internal boundaries separating the continuum- and pore-scale domains, $c_{1/2}$ (i.e., $i = 1$) and $c_{n_x+1/2}$ (i.e., $i = n_x$) must satisfy boundary conditions (5.28a) and (5.28b), respectively. This leads to

$$c_{1/2} = \frac{\mathcal{A}_{1/2}q_W + \left(-d_{1/2} + \mathcal{A}_{1/2}U/2\right)c_1}{-\mathcal{A}_{1/2}U/2 - d_{1/2}}, \tag{C.11a}$$

$$c_{n_x+1/2} = \frac{\mathcal{A}_{n_x+1/2}q_E - \left(d_{n_x+1/2} + \mathcal{A}_{1/2}U/2\right)c_{n_x}}{\mathcal{A}_{1/2}U/2 - d_{n_x+1/2}}. \tag{C.11b}$$

Combining (C.7) with (C.9)–(C.11) yields (5.26d).

If $\mathrm{Pe} \leq -2$ or $\mathrm{Pe} \geq 2$, then $c_{i+1/2}$ and $c_{i-1/2}$ $(i = 2, \ldots, n_x - 1)$ can be approximated by

$$c_{i-1/2} = \eta_{i-1/2}c_{i-1} - \xi_{i-1/2}c_i, \quad c_{i+1/2} = \eta_{i+1/2}c_i - \xi_{i+1/2}c_{i+1}, \tag{C.12}$$

where $\xi = \max\{-u, 0\}$ and $\eta = \max\{u, 0\}$. For $i = 1$ and $i = n_x$, the following formulae hold

$$c_{1/2} = \frac{\mathcal{A}_{1/2}q_W - c_1(d_{1/2} + \mathcal{A}_{1/2}\xi_{1/2})}{-d_{1/2} - \mathcal{A}_{1/2}\eta_{1/2}}, \tag{C.13a}$$

$$c_{n_x+1/2} = \frac{\mathcal{A}_{n_x+1/2}q_E - c_{n_x}(d_{n_x+1/2} + \mathcal{A}_{n_x+1/2}\eta_{n_x+1/2})}{-d_{n_x+1/2} - \mathcal{A}_{1/2}\xi_{n_x+1/2}}. \tag{C.13b}$$

Combining (C.7) with (C.9), (C.12), and (C.13) leads to (5.26e).

Bibliography

[1] C.P. Deck, C. Ni, K. S. Vecchio, and P.R. Bandaru, "The response of carbon nanotube ensambles to fluid flow: Applications to mechanical property measurement and diagnostics," *J. Appl. Phys.*, vol. 106, pp. 074304, 2009.

[2] P.V. Leemput, C. Vandekerckhove, W. Vanroose, and D. Roose, "Accuracy of hybrid lattice Boltzmann/finite difference schemes for reaction diffusion systems.," *Multiscale Model. Simul.*, vol. 6, no. 3, pp. 838–857, 2007.

[3] A. M. Tartakovsky, P. Meakin, T. D. Scheibe, and R. M. Eichler West, "Simulation of reactive transport and precipitation with smoothed particle hydrodynamics," *J. Comp. Phys.*, vol. 222, pp. 654–672, 2007.

[4] J.H. Walther, T. Werder, R.L. Jaffe, and P. Koumoutsakos, "Hydrodynamic properties of carbon nanotubes," *Phys. Rev. E*, vol. 69, pp. 062201, 2004.

[5] W. Um, R. J. Serne, S. B. Yabusaki, and A. T. Owen, "Enhanced radionuclide immobilization and flow path modifications by dissolution and secondary precipitates," *J. Environ. Qual.*, vol. 34, pp. 1404–1414, 2005.

[6] A. M. Tartakovsky, D. M. Tartakovsky, T. D. Scheibe, and P. Meakin, "Hybrid simulations of reaction-diffusion systems in porous media," *SIAM J. Sci. Comput.*, vol. 30, no. 6, pp. 2799–2816, 2008.

[7] M. Sahimi, "Flow phenomena in rocks: from continuum models to fractals, percolation, cellular automata, and simulated annealing," *Rev. Mod. Phys.*, vol. 65, no. 4, pp. 1393–1534, 1993.

[8] S. Whitaker, *The Method of Volume Averaging*, Kluwer Academic Publishers, Netherlands, 1999.

[9] P. E. Kechagia, I. N. Tsimpanogiannis, Y. C. Yortsos, and P. C. Lichtner, "On the upscaling of reaction-transport processes in porous media with fast or finite kinetics," *Chem. Engrg. Sci.*, vol. 57, no. 13, pp. 2565–2577, 2002.

[10] M. Shapiro and H. Brenner, "Taylor dispersion of chemically reactive species: Irreversible first-order reactions in bulk and on boundaries," *Chem. Engrg. Sci.*, vol. 41, no. 6, pp. 1417–1433, 1986.

[11] M. Shapiro and M. Brenner, "Dispersion of a chemically reactive solute in a spatially periodic model of a porous medium," *Chem. Engrg. Sci.*, vol. 43, no. 3, pp. 551–571, 1988.

[12] M. Shapiro, R. Fedou, J.-F. Thovert, and P. M. Adler, "Coupled transport and dispersion of multicomponent reactive solutes in rectilinear flows," *Chem. Engrg. Sci.*, vol. 51, no. 22, pp. 5017–5041, 1996.

[13] P. M. Adler, *Porous Media: Geometry and Transports*, Butterworth-Heinemann, 1992.

[14] R. C. Acharya, S. E. A. T. M. Van der Zee, and A. Leijnse, "Transport modeling of nonlinearly adsorbing solutes in physically heterogeneous pore networks," *Water Resour. Res.*, vol. 41, pp. W02020, 2005.

[15] W. G. Gray and C. T. Miller, "Thermodynamically constrained averaging theory approach for modeling flow and transport phenomena in porous medium systems: 1. Motivation and overview," *Adv. Water Resour.*, vol. 28, no. 2, pp. 161–180, 2005.

[16] U. Hornung, *Homogenization and Porous Media*, Springer, New York, 1997.

[17] G. de Marsily, *Quantitative Hydrogeology*, Academic Press, San Diego, California, 1986.

[18] H. Brenner, *Transport Processes in Porous Media*, McGraw-Hill, 1987.

[19] J.L. Auriault and P. M. Adler, "Taylor dispersion in porous media: analysis by multiple scale expansions," *Adv. Water Resour.*, vol. 4, no. 18, pp. 217–226, 1995.

[20] A. Mikelic, V. Devigne, and C. J. Van Duijn, "Rigorous upscaling of the reactive flow through a pore, under dominant Peclet and Damköhler numbers," *SIAM J. Math. Anal.*, vol. 38, no. 4, pp. 1262–1287, 2006.

[21] M. A. Peter, "Homogenization in domains with evolving microstructure," *C. R. Mécanique*, vol. 335, pp. 357–362, 2007.

[22] E. Marušić-Paloka and A. Piatnitski, "Homogenization of a nonlinear convection-diffusion equation with rapidly oscillating coefficients and strong convection," *J. London Math. Soc.*, vol. 2, no. 72, pp. 391–409, 2005.

[23] S. P. Neuman, "Theoretical derivation of Darcy's law," *Acta Mecanica*, vol. 25, pp. 153–170, 1977.

[24] H. Darcy, "Les fontaines publiques de la ville de dijon," *Victor Darmon*.

[25] J. L. Auriault, C. Geindreau, and C. Boutin, "Filtration law in porous media with poor separation of scales," *Transp. Porous Med.*, vol. 60, pp. 89–108, 2005.

[26] H. C. Brinkman, "A calculation of the viscous force exerted by a flowing fluid on a dense swarm of particles," *Appl. Sci. Res.*, vol. A1, pp. 27–34, 1949.

[27] T. Lévy, "Fluid flow through an array of fixed particles," *Int. J Eng. Sci.*, vol. 21, pp. 11–23, 1983.

[28] J.-L. Auriault, "On the domain of validity of Brinkman's equation," *Transp. Porous Med.*, vol. 79, pp. 215–223, 2009.

[29] L. Durlovsky and J. F. Brady, "Analysis of the brinkman equation as a model for flow in porous media," *Phys. Fluids*, vol. 30, no. 11, pp. 3329–3341, 2009.

[30] B. Goyeau, T. Benihaddadene, D. Gobin, and M. Quintard, "Averaged momentum equation for flow through a nonhomogeneous porous structure," *Transp. Porous Media*, vol. 28, pp. 19–50, 1997.

[31] M. Meyyappan, *Carbon nanotubes: science and applications*, CRC Press, Boca Raton, FL, 2005.

[32] J. A. Ochoa-Tapia, P. Stroeve, and S. Whitaker, "Facilitated transport in porous media," *Chem. Engng. Sci.*, vol. 46, pp. 477–496, 1991.

[33] B. D. Wood and R. M. Ford, "Biological processes in porous media: From the pore scale to the field," *Adv. Water Resour.*, vol. 30, no. 6-7, pp. 1387–1391, 2007.

[34] B. D. Wood, K. Radakovich, and F. Golfier, "Effective reaction at a fluid-solid interface: applications to biotransformation in porous media," *Adv. Water Resour.*, vol. 30, no. 6-7, pp. 1630–1647, 2007.

[35] T. L. van Noorden and I. S. Pop, "A Stefan problem modelling crystal dissolution and precipitation," *IMA J. Appl. Math.*, vol. 73, no. 2, pp. 393–411, 2008.

[36] F. Hesse, F. A. Radu, M. Thullner, and S. Attinger, "Upscaling of the advection-diffusion-reaction equation with Monod reaction," *Adv. Water Resour.*, vol. 32, pp. 1336–1351, 2009, 10.1016/j.advwatres.2009.05.009.

[37] K. J. Maloy, J. Feder, F. Boger, and T. Jossang, "Fractal structure of hydrodynamic dispersion in porous media," *Phys. Rev. Lett.*, vol. 61, no. 82, pp. 2925, 1998.

[38] S. P. Neuman and D. M. Tartakovsky, "Perspective on theories of anomalous transport in heterogeneous media," *Adv. Water Resour.*, p. doi:10.1016/j.advwatres.2008.08.005, 2008.

[39] A. M. Tartakovsky, D. M. Tartakovsky, and P. Meakin, "Stochastic Langevin model for flow and transport in porous media," *Phys. Rev. Lett.*, vol. 101, pp. 044502, 2008.

[40] C. Knutson, A. Valocchi, and C. Werth, "Comparison of continuum and pore-scale models of nutrient biodegradation under transverse mixing conditions," *Adv. Water Resour.*, vol. 30, no. 6-7, pp. 1421–1431, 2007.

[41] L. Li, C. Peters, and M. Celia, "Upscaling geochemmical reaction rates using pore-scale network modeling," *Adv. Water Resour.*, vol. 29, pp. 1351–1370, 2006.

[42] A. M. Tartakovsky, G. Redden, P. C. Lichtner, T. D. Scheibe, and P. Meakin, "Mixing-induced precipitation: Experimental study and multi-scale numerical analysis," *Water Resour. Res.*, vol. 44, pp. W06S04, doi:10.1029/2006WR005725, 2008.

[43] C. I. Steefel, D. J. DePaolo, and P. C. Lichtner, "Reactive transport modeling: An essential tool and a new research approach for the Earth sciences," *Earth Planet. Sci. Lett.*, vol. 240, pp. 539–558, 2005.

[44] P. Langlo and M. S. Espedal, "Macrodispersion for two-phase, immiscible flow in porous media," *Adv. Water Resour.*, vol. 17, pp. 297–316, 1994.

[45] Y. Efendief, L. J. Durlofsky, and S. H. Lee, "Modeling of subgrid effects in coarse-scale simulations of transport in heterogeneous porous media," *Water Resour. Res.*, vol. 36, no. 8, pp. 2031–2041, 2000.

[46] Y. Efendief and L. J. Durlofsky, "Numerical modeling of subgrid heterogeneity in two phase flow simulations," *Water Resour. Res.*, vol. 38, no. 8, 2002, 10.1029/2000WR000190.

[47] Y. Efendief and L. J. Durlofsky, "A generalized convection-diffusion model for subgrid transport in porous media," *Multiscale Model. Simul.*, vol. 1, no. 3, pp. 504–526, 2003.

[48] W. E, B. Engquist, and Z. Huang, "Heterogeneous multiscale method: a general methodology for multiscale modeling.," *Phys. Rev. B*, vol. 67, no. 9, pp. 092101, 2003.

[49] E. Villa, A. Balaeff, L. Mahadevan, and K. Schulten, "Multiscale method for simulating protein-dna complexes," *Mult. Model. Simul.*, vol. 2, pp. 527–553, 2004.

[50] X. Yue and W. E, "Numerical methods for multiscale transport equations and application to two-phase porous media flow," *J. Comput. Phys.*, vol. 210, pp. 656–675, 2005.

[51] D. G. Vlachos, A. B. Mhadeshwar, and N. S. Kaisare, "Hierarchical multiscale model-based design of experiments, catalysts, and reactors for fuel processing," *Comp. Chem. Engng.*, vol. 30, pp. 1712–1724, 2006.

[52] M.A. Christie, "Upscaling for reservoir simulation," *J. Petrol. Technol.*, vol. 48, pp. 1004–1010, 1996.

[53] F. J. Alexander, A. L. Garcia, and D. M. Tartakovsky, "Algorithm refinement for stochastic partial differential equations: 1. Linear diffusion," *J. Comp. Phys.*, vol. 182, pp. 47–66, 2002.

[54] F. J. Alexander, A. L. Garcia, and D. M. Tartakovsky, "Algorithm refinement for stochastic partial differential equations: II. Correlated systems," *J. Comp. Phys.*, vol. 207, no. 2, pp. 769–787, 2005.

[55] I. Battiato and D. M. Tartakovsky, "Applicability regimes for macroscopic models of reactive transport in porous media," *J. Contam. Hydrol.*, vol. Special issue, 2010.

[56] I. Battiato, D. M. Tartakovsky, A. M. Tartakovsky, and T. Scheibe, "On breakdown of macroscopic models of mixing-controlled heterogeneous reactions in porous media," *Adv. Water Resour.*, vol. 32, pp. 1664–1673, 2009.

[57] A. Malevanets and R. Kapral, "Solute molecular dynamics in a mesoscale solvent," *J. chem. Phys.*, vol. 112, pp. 7260–7269, 2000.

[58] P. V. Coveney and P. W. Fowler, "Modelling biological complexity: A physical scientist's perspective," *J. R. Soc. Interface*, vol. 2, pp. 267–280, 2005.

[59] M. M. J. Treacy, T. W. Ebbesen, and J. M. Gibson, "Exceptionally high Young's modulus observed for individual carbon nanotubes," *Nature*, 1996.

[60] M. R. Falvo, G. J. Clary, R. M. Taylor, V. Chi, F. P. Brooks, S. Washburn, and R. Superfine, "Bending and buckling of carbon nanotubes under large strain," *Nature*, 1997.

[61] J. Y. Huang, S. Chen, Z. Q. Wang, K. Kempa, Y. M. Wang, S. H. Jo, G. Chen, M. S. Dresselhaus, and Z. F. Ren, "Superplatic carbon nanotubes," *Nature*, 2006.

[62] P. Kim and C. M. Lieber, "Nanotube nanotweezers," *Science*, 1999.

[63] A. Srivastava, O. N. Srivastava, S. Talapatra, R. Vajtai, and P. M. Ajayan, "Carbon nanotube filters," *Nature Materials*, 2004.

[64] S. Ghosh, A. K. Sood, and N. Kumar, "Carbon nanotube flow sensors," *Science*, 2003.

[65] M. Wilson, "Superhydrophobic surfaces reduce drag," *Phys. Today*, 2009.

[66] P. Joseph, C. Cottin-Bizonne, J.-M. Benoit, C. Ybert, C. Journet, P. Tabeling, and L. Bocquet, "Slippage of water past superhydrophobic carbon nanotube forests in microchannels," *Phys. Rev. Lett.*, vol. 97, pp. 156104, 2006.

[67] M. Zhang, S. Fang, A.A. Zakhidov, S. B. Lee, A. E. Aliev, C. D. Williams, K. R. Atkinson, and R. H. Baughman, "Strong, transparent, multifunctional, carbon nanotube sheets," *Science*, vol. 309, no. 5738, pp. 1215–1219, 2005.

[68] A.N. Ford and D.V. Papavassiliou, "Flow around surface-attached carbon nanotubes," *Ind. Eng. Chem. Res.*, vol. 45, pp. 1797–1804, 2006.

[69] F. P. Beer, J. E. R. Johnson, and J. T. De Wolf, *Mechanics of Materials*, McGraw Hill, Boston, 4th edition, 2006.

[70] F.J. Valdes-Parada, J.A. Ochoa-Tapia, and J. Alvarez-Ramirez, "On the effective viscosity for the Darcy-Brinkman equation," *Physica A*, vol. 385, pp. 69–79, 2007.

[71] J. Happel, "Viscous flow relative to arrays of cylinders," *AIChE J.*, vol. 5, pp. 174–177, 1959.

[72] S. B. Pope, *Turbulent Flows*, Cambridge University Press, New York, USA, 2000.

[73] K. Vafai and S. J. Kim, "Fluid mechannics of the interface region between a porous medium and a fluid layer-an exact solution," *Int. J. Heat and Fluid Flow*, vol. 11, no. 3, pp. 254–256, 1990.

[74] D. A. Niel, S. L. M. Junqueira, and J. L. Lage, "Forced convection in a fluid-saturated porous-medium channel with isothermal or isoflux boundaries," *J. Fluid Mech.*, vol. 322, pp. 201–214, 1996.

[75] J. P. Lu, "Elastic properties of carbon nanotubes and nanopores," *Phys. Rev. Lett.*, vol. 79, no. 7, pp. 1297, 1997.

[76] P. Poncharal, Z. L. Wang, D. Ugarte, and W. A. de Heer, "Electrostatic deflections and electromechanical resonances of carbon nanotubes," *Science*, vol. 283, no. 1513, pp. DOI: 10.1126/science.283.5407.1513, 1999.

[77] B. Vigolo, A. Penicaud, C. Coulon, C. Sauder, R. Pailler, C. Journet, P. Bernier, and P. Poulin, "Macroscopic fibers and ribbons of oriented carbon nanotubes," *Science*, vol. 290, no. 1331, pp. DOI: 10.1126/science.290.5495.1331, 2000.

[78] M.-F. Yu, B. S. Files, S. Arepalli, and R. S. Ruoff, "Tensile loading of ropes of singlewall carbon nanotubes and their mechanical properties," *Phys. Rev. Lett.*, vol. 84, no. 24, 2000.

[79] R.H. Baughman, A. A. Zakhidov, and W. A. de Heer, "Carbon nanotubes-the route toward applications," *Science*, vol. 297, no. 2, pp. 787–793, 2002.

[80] P. Knabner, C. J. Van Duijn, and S. Hengst, "An analysis of crystal dissolution fronts in flows through porous media. part 1: Compatible boundary conditions," *Adv. Water Resour.*, vol. 18, no. 3, pp. 171–185, 1995.

[81] C. J. Van Duijn and I. S. Pop, "Crystal dissolution and precipitation in porous media: pore-scale analysis," *J. Reine Angew. Math.*, vol. 577, pp. 171–211, 2004.

[82] Z. Jiang and C. Ebner, "Simulation study of reaction fronts," *Phys. Rev. A*, vol. 42, pp. 7483–7486, 1990.

[83] M. M. Reddy, L. N. Plummer, and E. Busenberg, "Crystal growth of calcite from calcium bicarbonate solutions at constant p_{CO_2} and 25 c: a test for calcite dissolution model," *Geochimica et Cosmochimica Acta*, vol. 45, pp. 1281–1289, 1981.

[84] R. L. Jacobson and D. Langmuir, "Dissociation constant of calcite and $cahco_3^+$ from 0 to 50 c," *Geochimica et Cosmochimica Acta*, vol. 38, pp. 301–318, 1974.

[85] P. K. Kundu and I. M Cohen, *Fluid Mechanics*, Elsevier, San Diego, 4th edition, 2008.

[86] L. C. Nitsche and H. Brenner, "Eulerian kinematics of flow through spatially periodic models of porous media," *Arch. Ration. Mech. Anal.*, vol. 107, no. 3, pp. 225–292, 1989.

[87] M. Quintard and S. Whitaker, "Transport in ordered and disordered porous media II: Generalized volume averaging," *Transp. Porous Media*, vol. 14, pp. 179–206, 1994.

[88] S. Whitaker, "Flow in Porous Media I: A Theoretical Derivation of Darcy's Law," *Transp. Porous Media*, vol. 1, pp. 3–25, 1986.

[89] J. W. Morse and R. S. Arvidson, "The dissolution kinetics of major sedimentary carbonate minerals," *Earth Sci. Rev.*, vol. 58, pp. 51–84, 2002.

[90] P. C. Lichtner and D. M. Tartakovsky, "Upscaled effective rate constant for heterogeneous reactions," *Stoch. Environ. Res. Risk Assess.*, vol. 17, no. 6, pp. 419–429, 2003.

[91] D. M. Tartakovsky, M. Dentz, and P. C. Lichtner, "Probability density functions for advective-reactive transport in porous media with uncertain reaction rates," *Water Resour. Res.*, vol. 45, pp. W07414, 2009.

[92] S. Broyda, M. Dentz, and D. M. Tartakovsky, "Probability density functions for advective-reactive transport in radial flow," *Stoch. Environ. Res. Risk Assess.*, pp. doi:10.1007/s00477–010–0401–4, 2010.

[93] G. E. Grisak and J. F. Pickens, "Solute transport through fractured media, 1. The effect of matrix diffusion," *Water Resour. Res.*, vol. 16, no. 4, pp. 719–730, 1980.

[94] G. E. Grisak, J. F. Pickens, and J. A. Cherry, "Solute transport through fractured media, 2. Column stydy of fractured till," *Water Resour. Res.*, vol. 16, no. 4, pp. 731, 1980.

[95] M. Prat, "On the boundary conditions at the macroscopic level," *Transp. in Porous Media*, vol. 4, pp. 259–280, 1989.

[96] M. Pratt, "On the boundary conditions at the macroscopic level," *Transp. Porous Media*, vol. 4, pp. 259–280, 1989.

[97] H. K. Versteeg and M. Malalasekera, *An Introduction to Computtaional Fluid Dynamics: The Finite Volume Method*, Pearson Education Ltd.; Harlow, England; New York, 2007.

[98] D. B. Spalding, "A novel finite-difference formulation for differential expressions involving both first and second derivatives," *Int. J. Numer. Methods Eng.*, vol. 4, pp. 551, 1972.